

From information flow to transport investigations in fusion

Revealing the nature of transitions to core-electron-root-confinement in
Wendelstein 7-X

Inauguraldissertation

zur

Erlangung des akademischen Grades eines
Doktors der Naturwissenschaften
(Dr. rer. nat.)

der

Mathematisch-Naturwissenschaftlichen Fakultät

der

Universität Greifswald

vorgelegt von

Juan Fernando Guerrero Arnaiz

Greifswald, 31.07.2023

Dekan

Prof. Dr. Gerald Kerth

1. Gutachter

PD. Dr. habil. Andreas Dinklage

2. Gutachter

Ass.Prof. Dr. Christopher Albert

3. Gutachter

Prof. Dr. Yasuhiro Suzuki

Tag der Promotion: 18.12.2023

Contents

Abstract	1
1 Introduction: stellarators on the path to fusion electricity	2
1.1 Wendelstein 7-X	4
1.2 Core-electron-root-confinement regime	6
1.3 Novelty detection in timeseries from experimental fusion data	7
2 Methods	8
2.1 Entropy-based data analysis methods	8
2.1.1 Mutual information, partial mutual information and transfer entropy	9
2.1.2 Permutation entropy	10
2.2 Experimental methods	11
2.2.1 Electron cyclotron emission diagnostic	11
2.2.2 Soft X-ray multi-camera tomography system	13
2.2.3 Spatio-temporal fluctuation analysis	14
2.3 Numerical modelling	16
2.3.1 Ideal MHD	16
2.3.2 MHD spectrum	17
2.3.3 Gyrokinetic simulations	18
2.3.4 Radially resolved frequency analysis of simulated potential	19
3 Results	21
3.1 Article I	21
3.2 Article II	22
3.3 Article III	23
4 Conclusion	26
5 Outlook: towards real-time novelty detection	27
Bibliography	36
A. Thesis Articles	37
A.1 Article I	40
A.2 Article II	52
A.3 Article III	66
B. Statutory Declaration	103
C. Acknowledgements	104

Abstract

In course of the recent results from Wendelstein 7-X, stellarators are on the brink for assessing their maturity as a fusion reactor. To this end, stellarator specific transport regimes need detailed exploration both with appropriate systematic experimental investigations and models. A way to enhance the efficiency of this process is seen in a systematic evaluation of existing experimental data. We propose appropriate tools developed in information theory for examining large datasets. Information entropy calculations, that have proven to assist the systematic assessment of datasets in many other scientific fields, are used for novelty detection.

Potentially, as a first use-case of this holistic process, this thesis attempts to link and to develop approaches to examine the stellarator specific core-electron-root-confinement (CERC) regime. The specific interest for CERC emerges from the behavior of the radial electric field. While ion-root conditions exhibit negative radial electric fields, CERC's positive field in the very core of fusion grade plasmas adds an outward thermodynamic force to high-Z impurities and could add to potential actuators to control impurity influx as to be examined for full-metal wall operation in large stellarators. Recently, this feature received revived intent for reactor scale stellarators.

Also, in this work, parameter regions close to the transition from ion-root to CERC are examined. At lower rotational transform (a characteristic feature of the magnetic field confining fusion grade plasmas), transitions were detected when the plasma current evolved. As in smaller stellarators, it is concluded that low-order rationals and magnetic islands are related to the transitions. This is widely supported by extensive MHD simulations which finally provide indications for the role of zonal flow oscillations. As one of the outcomes, gyrokinetic instabilities are seen interacting for the first time with the neoclassical mechanisms in experiments.

In order to cope with the vast number of highly sampled spatio-temporal plasma data, new techniques for novelty detection are required. Fundamental prerequisites for the detailed physics investigations were the feasibility study of entropy-based data analysis techniques, and their adaptation to detect previously unrevealed transition mechanisms. These tools were applied to multivariate bulk plasma emissivity data, which allowed the exploration of large parameter spaces and provided insights in the spatio-temporal dynamics of CERC transitions.

In this manner, this research highlights the feasibility of information flow measure analysis in fusion studies. Applications of different entropy-based complexity measures are explored and this work sheds light on the capabilities, added value and limitations of these techniques. This investigation presents the integration of information flow measures to gain deeper understanding of plasma transport phenomena, by providing an approach to fast systematic data mining suited for real-time analysis. This work paves the way for further development and implementation of information-theoretic methods for plasma data analysis.

In summary, this research highlights the gained insight on CERC transitions, while showcasing the feasibility, added values and limitations of information flow measure analysis for fusion studies, to induce theory based analysis revealing new insights in fundamental, stellarator-specific transport mechanisms.

1 Introduction: stellarators on the path to fusion electricity

Fusion energy develops swiftly towards becoming an option for a sustainable solution to meet the ever-increasing global energy demands [1, 2]. At its core, nuclear fusion involves the collision of light atomic nuclei, such as isotopes of hydrogen (deuterium and tritium), that merge into heavier nuclei and release vast amounts of energy in the process. The fundamental principle behind fusion lies in the binding energy of atomic nuclei. When two light nuclei combine, the resulting nucleus has a slightly lower mass than the combined mass of its individual constituents. This defect mass is converted into energy according to $E = mc^2$, where E represents energy, m represents mass, and c represents the speed of light. The energy released in a fusion reaction $O(\sim 10\text{ MeV})$ is roughly seven orders of magnitude greater than that released in chemical reactions $O(\sim 1\text{ eV})$, making fusion an incredibly efficient energy source.

The potential benefits of fusion energy are significant. Fusion reactions primarily produce helium, a non-toxic and inert gas, as their main byproduct. Unlike conventional energy sources, such as fossil fuels, fusion does not emit greenhouse gases or produce long-lived radioactive waste. Moreover, fusion fuel sources, deuterium and tritium, can be obtained from seawater and are virtually inexhaustible. Therefore, fusion energy is a promising renewable and sustainable energy source.

However, harnessing fusion energy is a complex scientific and engineering challenge [3]. To achieve fusion conditions, extremely high temperatures exceeding millions of degrees Celsius are required to overcome the strong electrostatic repulsion between atomic nuclei. Additionally, the fuel must be confined long enough for the fusion reactions to occur. Achieving this confinement is one of the key challenges in fusion research.

In recent years, exceptional progress in fusion physics has been achieved in terms of developing advanced diagnostic, exploring innovative materials that can withstand high heat and particle fluxes, and reactor design and optimization between others. This progress sets the stage for the leading concepts to utilize fusion: magnetic confinement fusion (MCF) and inertial confinement fusion (ICF).

In 1997, the Joint European Torus (JET) tokamak, an MCF device built in Culham Centre for Fusion Energy in the United Kingdom, set the record for the closest approach to scientific break-even, reaching $Q = 0.67$ [4] (ratio of fusion power produced to the power required to maintain the plasma). Furthermore, the plasma facing components to be implemented in the International Thermonuclear Experimental Reactor (ITER), the largest experimental tokamak with the goal of achieving $Q \geq 10$ [5], have been investigated. The JET ITER-like walls, employing beryllium in the main chamber and tungsten in the divertor, were ideal to test the power handling capability of these components under relevant heat loads conditions. The components were successfully tested and met the expected performance [6, 7].

In 2022, for the very first time, the scientific break-even was surpassed in an ICF facility. This occurred at the National Ignition Facility (NIF) at Lawrence Livermore National Laboratory in the United States, reaching $Q = 1.5$ [8]. Although this milestone is remarkable and

serves as confirmation of the science of fusion energy, the concept *indirect drive* is used at NIF, which might be difficult to scale to reactor relevant conditions. Nearly 200 high-energy lasers are employed to heat a metal cylinder surrounding a spherical pellet containing a mix of deuterium and tritium. The cylinder re-emits the incoming energy as even higher frequency X-rays to the pellet, compressing it and leading to its implosion [9]. For now, it remains unclear how this experiment could be scaled to achieve efficient steady state operation in reactor relevant conditions, however, more efficient concepts such as the so-called *direct-drive* may be an alternative [10].

In the other hand, the next step in MCF is ITER. ITER, currently being built in Cadarache in France, will be the largest magnetic confinement plasma physics experiment. ITER is an international collaboration involving 35 countries and will pave the way for the development of commercial fusion reactors that can potentially provide a sustainable and abundant source of clean energy, with no greenhouse gas emissions and limited radioactive waste.

A variety of fusion device concepts have been explored over the years, each with its own advantages and challenges [11]. The leading alternative to the tokamak line is the stellarator. A stellarator, which is an MCF concept, employs a confining magnetic field generated by external coils, unlike their tokamak counterparts, which employ a toroidal magnetic field with a current-carrying plasma. Since the poloidal field (required to generate the twist (rotational transform, ι) of field lines needed for a stable plasma) in stellarators does not require an inductively driven (and therefore time-wise finite) large plasma current, stellarators can be operated continuously by principle. Plasmas in stellarators are expected to benefit from an increase of shear of ι to its boundary (opposite to tokamaks). As a result, stellarators do not exhibit related instabilities leading to quiescent plasmas. These striking advantages come for a price. The helical field component generating the field-like twist generates toroidally localized magnetic mirrors that typically enhance the plasma transport. That is, external helical windings produce local magnetic wells in which trapped particles are unfavorably confined (increasing diffusion losses), thus requiring a drift-optimized configuration that ensures satisfactory fast ion-confinement in the center of the plasma [12]. These particle and heat transport processes that arise due to the interplay between the 3-D magnetic field geometry and the particle drifts are referred to as *neoclassical transport*. The magnetic topology in Wendelstein 7-X (W7-X) was optimized according to seven criteria [13] and one of these criteria was minimizing the neoclassical transport. It is the most important break-through of Wendelstein 7-X to have demonstrated a concept to mitigate these issues in so-called *classical stellarators*.

Due to neoclassical transport, bifurcations to transport regimes emerge i.e. the transition from an ion-root to an electron-root-confinement-regime (CERC, [14–16]). To ensure steady state operation, it is crucial to understand how transitions to favorable plasma confinement regimes such as CERC occur. These transitions were observed in experiments with evolving ι conducted in the fusion research device Heliotron-J (H-J) [17] and the heliac TJ-II [18, 19]. In H-J, spontaneous increases of the electron temperature were observed going along the evolution of ι and its crossing through a specific rational value. Also, during ion- to core-electron-root-confinement transitions in the Compact Helical System, it was observed that magnetic perturbations were capable of triggering these transitions [20]. However, the interplay be-

tween the aforementioned mechanisms have not yet been fully explored. To detect and react accordingly to plasma state changes that could compromise the plasma confinement, novelty detection methods are employed. Currently, techniques based on neural networks are implemented [21–24]. Nevertheless, these may require large data sets for training and may also require large computational power to operate appropriately. To overcome this shortcomings, this work introduces the permutation entropy (PE) analysis, an entropy-based novelty detection technique, for the analysis of bulk plasma data. This method has been implemented in different science branches [25–27] and it has been proven to be a fast and robust data-driven anomaly detection technique that is able to handle large data sets in an automated procedure, which does not require strong assumptions about the underlying dynamics of the analyzed data. After detecting plasma state changes, the underlying physical mechanisms triggering the transitions can be characterized to gain insight on the transport processes, deepening our understanding of the transition mechanisms.

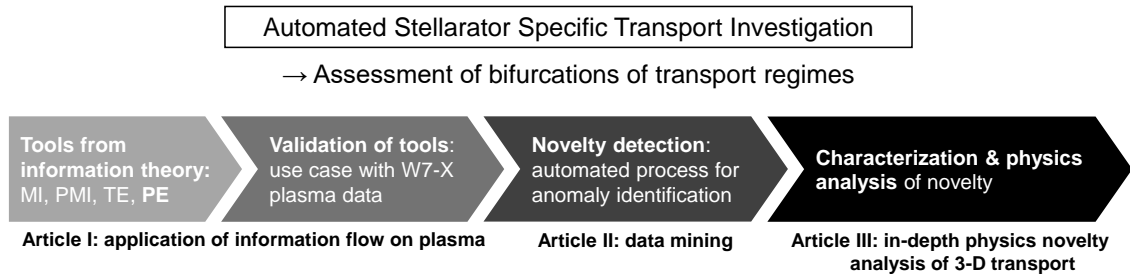


Fig. 1: Chevron diagram depicting the structure of this thesis.

With this background, this thesis presents the automated analysis of information flow measures for transport investigations. The structure of this thesis is illustrated in Fig. 1. First, this research introduces and validates the information-theoretic methods to be employed on plasma data (cf. **Article I**). Then, their implementation for the detection of previously undetected plasma phenomena in an automated procedure is presented (cf. **Article II**). Finally, the physical characterization of these new findings is explored (cf. **Article III**). The relevance of this work lies in deepening our understanding on the underlying mechanisms leading to transitions to the CERC regime, and showcasing the identification of actuators that could influence the plasma confinement in W7-X; therefore, contributing to the bigger picture of developing favorable plasma scenarios for future reactors.

1.1 Wendelstein 7-X

W7-X is an optimized, super-conducting stellarator fusion device [28] operating since 2014 at the Max Planck Institute for Plasma Physics in Greifswald, Germany. W7-X is designed to explore the extent to which stellarator optimization can lead to achieving fusion grade plasmas. The project aims to reach high performance steady state operation to demonstrate that such a device is a suitable option for a fusion power plant.

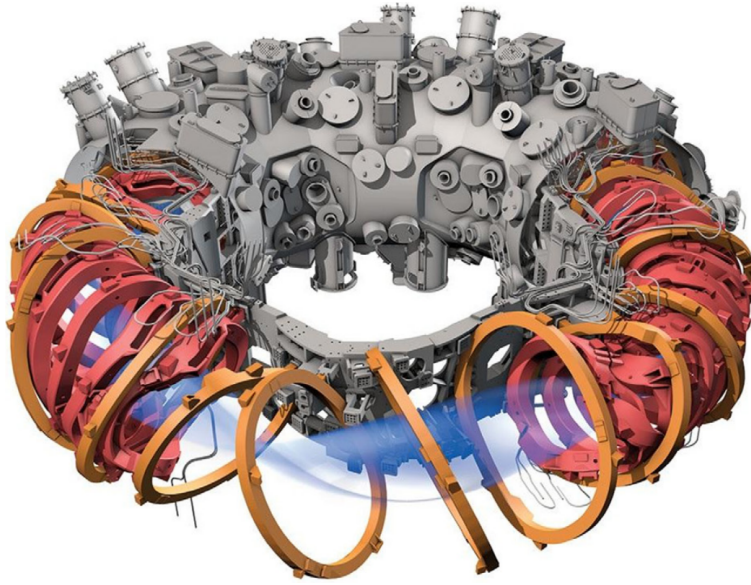


Fig. 2: Schematic structure of W7-X. The plasma shape is represented in blue. The coil system is shown in red (non-planar coild) and in orange (planar coild). © IPP

A schematics of W7-X is illustrated in Fig. 2. W7-X is equipped with a system of 50 superconducting magnet coils arranged meticulously to provide precise control over the plasma's magnetic field [29]. These coils are capable of producing a maximum magnetic field strength of 3 T, but are to date operated at 2.5 T to provide the magnetic field for the absorption of microwave radiation of both electrons and ions. The plasma vessel has a toroidal shape, with a major radius R of 5.5 m and a minor radius r of 0.5 m, allowing for the confinement of plasma volumes up to 30m^3 . Additionally, up-to-date, more than 30 diagnostic systems including high-resolution cameras, laser interferometers, an electron cyclotron emission radiometer and X-ray detectors have been commissioned, enabling detailed monitoring and analysis of plasma behavior during experimental campaigns.

To achieve magnetic confinement in a plasma, the Lorentz force guides charged particles along magnetic field lines. For this purpose, the field lines must form closed loops, enabling trajectories that helically wind around the torus and keep the particles ideally away from the plasma vessel walls. This configuration establishes a magnetic topology where the field lines, after numerous turns, trace out nested circular surfaces referred to as magnetic surfaces. These are also commonly known as flux surfaces since the poloidal flux is constant across any point on a given magnetic surface.

In the context of ideal magnetohydrodynamics (MHD), the plasma is considered as an electrically conducting fluid and all dissipative processes (i.e. viscosity, electrical resistivity and thermal conductivity) are neglected. This approximation is valid as long as the plasma velocities are not relativistic and the characteristic time and scale are both much greater than the ion gyroperiod and gyroradius respectively. Employing equations of fluid dynamics and Maxwell's equations, MHD describes large scale slow dynamics of plasmas. More specifi-

cally, a self-consistent set of MHD equations connects the plasma mass density ρ , the plasma velocity \mathbf{V} , the thermodynamic pressure p and the magnetic field \mathbf{B} . The closed set of MHD equation reads

$$\begin{aligned} \frac{\partial p}{\partial t} + \nabla(\rho \mathbf{V}) &= 0 , && \text{Mass Continuity equation,} \\ \frac{d}{dt} \left(\frac{p}{\rho^{\gamma_C}} \right) &= 0 , && \text{Energy equation,} \\ \rho \frac{d\mathbf{V}}{dt} &= -\nabla p - \frac{1}{\mu_0} \mathbf{B} \times (\nabla \times \mathbf{B}) , && \text{Euler's equation,} \\ \frac{\partial \mathbf{B}}{\partial t} &= \nabla \times (\mathbf{V} \times \mathbf{B}) , && \text{Induction equation,} \end{aligned}$$

where γ_C is the ratio of the specific heats C_p/C_V . These equations are derived and discussed more in detail in [30]. From Euler's equation, with static equilibrium conditions ($V = 0$ and $\partial/\partial t = 0$), the equation can be rewritten as

$$-\nabla \left(p + \frac{B^2}{2\mu_0} \right) + \frac{1}{\mu_0} (\mathbf{B} \cdot \nabla) \mathbf{B} = 0 . \quad (1)$$

The second term (representing the magnetic tension) is directed anti-parallel to the radius of the magnetic field line curvature, thus vanishes and Eq.1 results in the pressure balance

$$p + \frac{B^2}{2\mu_0} = \text{constant} . \quad (2)$$

The second term in Eq.2 represents the magnetic pressure, which ensures the constancy of the total pressure in the plasma fluid [31]. The magnetic field exerts a force on the plasma that can counterbalance the pressure gradient, allowing for the existence of a pressure gradient within the plasma. Notably, the pressure gradient is perpendicular to both the plasma current and the magnetic field, and since both of these vectors lie on the flux surfaces, it implies the absence of a pressure gradient along the field lines. Thus, the magnetic surfaces correspond to regions of constant p , T , and n and any fluctuations in these parameters are rapidly smoothed out.

1.2 Core-electron-root-confinement regime

Efficient confinement of high-energy particles and the minimization of energy losses are key prerequisites for achieving the conditions necessary for sustained fusion reactions. Therefore, detecting, identifying and reacting to particle and energy transport processes that play a major role in determining the performance and efficiency of fusion reactors is crucial. However, understanding and controlling these processes present formidable challenges due to the complex nature of plasmas. Turbulent transport, driven by instabilities arising from plasma density and temperature gradients, can cause particle losses and degrade energy confinement. Neoclassical transport, on the other hand, is influenced by particle drifts in magnetic fields and can

impact both particle and energy confinement. The 3-D geometry of the magnetic field in stellarators produces localized particles resulting in large neoclassical transport rates [32]. That is, trapped particles experience a radial drift until pitch-angle collisions scatter them out of the local magnetic ripple in which they are orbiting. This feature provides the so-called $1/\nu$ regime with less frequent collisions leading to particle losses [33]. According to neoclassical transport theory, a radial electric field E_r can limit the radial drift of ripple-trapped electrons and thereby suppresses the unfavorable $1/\nu$ transport. A radial electric field emerges from different particle fluxes of ions and electrons. In the neoclassical approach, E_r is calculated from the roots of the ambipolarity condition of the local (diffusive) electron and ion particle fluxes, which can be written as

$$Z_i \Gamma_i = \Gamma_e ,$$

where Γ_α represents the neoclassical particle flux of a specie α , and Z is the atomic number. Detailed derivations of multiple roots of the ambipolarity constraint can be found in [16]. For highly peaked T_e and fairly flat T_i profiles with $T_e \gg T_i$, the neoclassical electron flux can exceed that of the ions, so that a strongly positive E_r is needed to reduce Γ_e . Thus, under these special conditions, an improved confinement regime [34], specific to helical devices, is attained. This is the core-electron-root-confinement (CERC) regime [14–16].

1.3 Novelty detection in timeseries from experimental fusion data

Investigating the transitions between different confinement regimes in W7-X is crucial and involves using novelty detection techniques to detect these signatures within plasma datasets. In plasma physics, novel phenomena encompass a range of physical processes or unexpected events that warrant further investigation, such as plasma instabilities, turbulence, and, specifically in this case, transitions between different transport regimes, among others. Novelty detection techniques identify patterns or events in data that significantly deviate from the previously observed behavior. By detecting these occurrences and recognizing the conditions under which such events manifest, an initial characterization of the detected phenomena becomes possible. This contributes to a deeper understanding of the underlying processes and interactions within the plasma, potentially shedding light on the triggers that lead to transitions between different confinement regimes.

In this thesis, entropy is leveraged as a measure of uncertainty and disorder to reveal anomalies within plasma data. By these means, novelty detection, employing entropy-based methods, serves as a powerful data mining tool to automate the process of scanning through large datasets and identify fingerprints of bifurcation like transitions. It turns out that the employed entropy-based methods can be used to keep with respective requirements for plasma control. That is, by delivering results fast enough to allow for real-time monitoring and analysis of plasma parameters, enabling rapid response and adaptive control in dynamic plasma environments. Another potential application is reacting to known signatures revealed in the novelty detection procedure, e.g. to avoid transitions and securing favorable plasma conditions.

2 Methods

The following section presents an overview of the methodologies employed in this study. The methods utilized are categorized into three primary subsections: entropy-based data analysis methods, experimental methods, and numerical modelling. Each subsection is dedicated to highlight specific approaches that contribute to a deeper understanding of the underlying mechanisms driving the plasma phenomena investigated. The subsection on entropy-based data analysis methods explores innovative techniques designed to investigate dependencies and extract patterns from multivariate datasets. The subsequent subsection on experimental methods provides the experimental setup of the main diagnostics employed in this research, the physical principles on which these diagnostics are based, and the derivation of the relevant physical quantities of interest. Lastly, the numerical modeling subsection provides an outline of the diverse computational models employed in this study. These models are utilized to assess the feasibility of various mode activities that align with the experimental observations. Additionally, they play a crucial role in evaluating the influence that magnetic islands, the rotational transform, and the radial electric field have on the transitions to the core-electron-root-confinement regime. By integrating these diverse methodological approaches, this study aims to shed light on the nature of these transitions.

2.1 Entropy-based data analysis methods

The concept of entropy, borrowed from statistical mechanics and information theory, provides a measure of the randomness and disorder in a system. In the context of plasma data analysis, entropy-based methods aim to quantify the degree of complexity and information content embedded within the plasma signals. The application of entropy-based methods in plasma physics is motivated by several factors. Firstly, plasmas exhibit complex and nonlinear behavior, making traditional analysis techniques insufficient to capture their intricate dynamics. Entropy-based methods, by quantifying and analyzing various complexity measures in plasma signals, have the potential to offer further insights, even when dealing with intricate dynamics that traditional analysis techniques might not adequately capture.

Secondly, fusion devices, such as W7-X, generate vast amounts of data, consisting of multiple plasma parameters and diagnostic signals. Extracting relevant information from bulk data requires advanced analysis techniques capable of unraveling hidden patterns and correlations. Entropy-based methods provide a systematic and quantitative approach to analyze large datasets, enabling the identification of relevant features.

Thirdly, understanding and controlling plasma turbulence and transport processes are critical to maintain optimal plasma confinement conditions and performance. Entropy-based methods offer the potential to characterize and quantify plasma turbulence, providing valuable information on the underlying mechanisms driving transport phenomena. By unraveling the complex dynamics of turbulence, entropy-based methods can aid in developing strategies to predict and mitigate turbulence, as well as improve plasma confinement.

2.1.1 Mutual information, partial mutual information and transfer entropy

Information theory, and therefore the methods for the data analysis presented in this thesis, revolve around Shannon entropy [35], a measure used to quantify the average amount of information or uncertainty associated with a random variable or probability distribution. In other words, Shannon entropy H of a random variable X indicates the amount of information that is required on average to fully characterize a random variable, that is, to describe and specify the range and likelihood of the different possible outcomes of X . This quantity is defined as $H(X) = -\sum_x p(x)\log p(x)$, where $p(x)$ is the probability distribution of X .

The complexity measures subsequently implemented for the coupling analysis of plasma data are introduced in a pictorial approach as illustrated by the Venn diagrams shown in Fig. 3. More specifically, mutual information (MI), partial mutual information (PMI) and transfer entropy (TE) are respectively depicted in Fig. 3(a-c) as gray shaded regions (cf. **Article I** for detailed mathematical formulations).

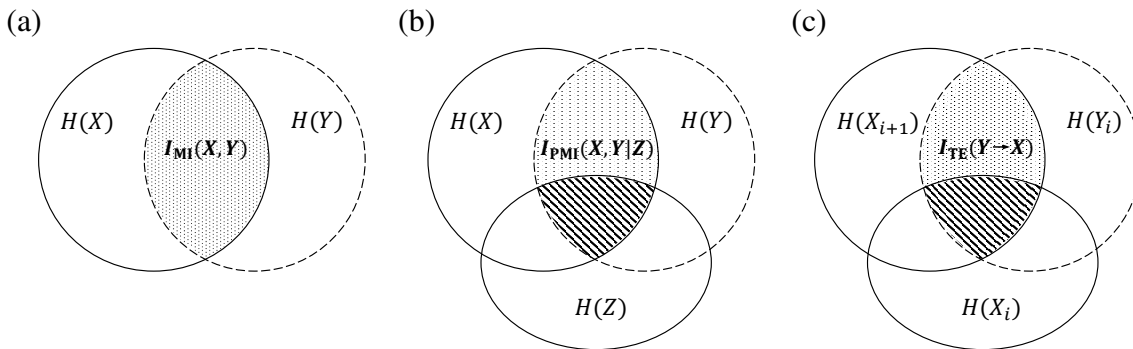


Fig. 3: Venn diagrams representing (a) the mutual information $I_{MI}(X, Y)$, (b) the partial mutual information $I_{PMI}(X, Y)$ and (c) the transfer entropy $I_{TE}(Y \rightarrow X)$ between random variables X , Y and Z .

Mutual information (MI) quantifies the statistical dependence between two or more variables by measuring the reduction in uncertainty of one variable given the knowledge of another [35]. In other words, the MI between random variables X and Y denoted by $I(X, Y)$ can be interpreted as the amount of information that can be obtained of X from realizations of Y . Therefore, this measure is employed to assess data similarity and analyze mutual influence between different systems.

Partial mutual information (PMI) extends the concept of mutual information by considering the relationship between two variables while accounting for the influence of additional variables [36]. More specifically, the PMI between X and Y , conditioned to a third known random variable Z is denoted by $I(X, Y|Z)$ and describes the information that can be obtained of X from realizations of Y (definition of MI), but discounting the contributions that Z has to the mutual dependencies of X and Y . Therefore, PMI analysis delivers robust coupling results that are crucial for understanding the mutual dependencies between systems, while taking into account the influence of spurious signals.

Transfer entropy (TE) is a special case of partial mutual information and it quantifies the flow of new information between variables [37]. Considering X_i as all observed realizations of X up to an instance i , the TE from Y to X is denoted by $I(Y \rightarrow X)$, or $I(Y_i, X_{i+1} | X_i)$ in terms of PMI, and quantifies the amount of information contained in the last realization X_{i+1} that is also contained in Y_i , but not contained in past realizations X_i . Therefore, by taking as conditioning the past realizations of one variable, TE allows one to unravel the directed information flow between different systems. Thus, a TE analysis may be employed to determine causal relationships and assess the strength and direction of information transfer.

The aforementioned techniques have been widely applied in different scientific branches. For example: mutual information analysis has been implemented in economics to develop local linear predictors for forecasting currency exchange rates [38]; partial mutual information technique has been applied on systems of coupled oscillators to distinguish between unidirectional and bidirectional couplings [39]; and transfer entropy analysis has been employed in biomedical engineering to measure the impact of administrating a dopamine receptor antagonist on the respiratory physiology in lambs.

In recent years, these methods have been gaining traction in the field of fusion plasmas. E.g. transfer entropy analysis has been implemented to investigate plasma instabilities such as edge-localized modes [40] (nonlinear instabilities that occur at the plasma edge that can lead to periodic release of bursts of energy and particles from the plasma boundary) and heat transport [41, 42]. Therefore, in the context of high-temperature plasma data, these techniques provide data-driven approaches that do not require strong assumptions about the complex underlying dynamics in the plasma. This flexibility makes the aforementioned entropy-based coupling analysis methods attractive for the analysis of e.g. nonlinear plasma instabilities and turbulence. Therefore, a suite of information-theoretic methods may contribute to a robust analysis of the interactions among plasma variables, which is essential for effective control strategies i.e. to mitigate instabilities and overall plasma phenomena that could compromise the plasma confinement.

In this work, mutual information, partial mutual information and transfer entropy are implemented to analyze couplings between multivariate spatio-temporal plasma data.

2.1.2 Permutation entropy

Permutation entropy analysis can be employed to detect novel patterns in datasets. PE is a nonlinear complexity measure that quantifies the irregularity or randomness in a timeseries. It captures the temporal structures in data by considering the order relations between m data points separated by an embedding delay τ_D from each other (cf. **Article II** for a detailed description of PE including an analysis of synthetic data). Since it is an ordinal technique, it does not rely on high-dimensional distance calculations but rather on sorting algorithms to determine the ordinal ranking between data points, resulting in fast computation times. Also, unlike traditional entropy complexity measures, permutation entropy does not assume a specific probability distribution, making it robust and suitable for analyzing non-stationary and nonlinear systems.

In plasma physics, permutation entropy analysis can be implemented as a fast and robust method for the analysis of large datasets with intricate temporal dynamics. Similar to the entropy-based techniques discussed in this section, PE provides a data-driven approach that does not require strong assumptions about the complex underlying dynamics in the plasma. Moreover, permutation entropy can aid in the detection of plasma state transitions (significant changes in the collective behavior of the plasma). Therefore, regions of high complexity that may correspond to novel or transient phenomena can be identified by means of PE analysis, and these anomalies can then be further investigated to understand their underlying physical mechanisms. As technology continues to evolve and datasets grow in length and complexity, the application of permutation entropy in plasma physics holds great promise for future research and discoveries.

2.2 Experimental methods

The diagnostics providing the experimental measurements to be analyzed by means of the aforementioned entropy-based methods are presented in this section. More specifically, the electron cyclotron emission (ECE) diagnostic and the soft X-ray multi-camera tomography system (XMCTS) are introduced. The former delivers spatio-temporal electron temperature T_e measurements along a line of sight that crosses the plasma center, whereas the latter provides X-ray emissivity measurements in a 2-D poloidal plane that can be employed for tomographic reconstructions. The objective of analyzing these measurements is, on one hand, to investigate any potential relationship between the frequency of fluctuating activity and the plasma parameters and, on the other hand, to characterize the activity in order to distinguish between possible modes and identify the fluctuating behavior. In this section, we also discuss the analysis of magnetic displacement using a spatio-temporal fluctuation analysis as a method for characterizing this activity.

2.2.1 Electron cyclotron emission diagnostic

To achieve the ambitious goals set for the W7-X project, several advanced diagnostics are employed to study and understand the behavior of high-temperature plasmas. One of the key diagnostic tools employed is the ECE diagnostic, which plays a crucial role in providing valuable insights into the electron temperature T_e and its spatial distribution within the plasma. More specifically, the ECE diagnostic enables the derivation of electron temperature profiles across the plasma cross-section. The spatial distribution of T_e is of particular interest in fusion research since it provides crucial information about the plasma's behavior, such as the heat transport processes and the effectiveness of the magnetic confinement.

The ECE diagnostic is a non-invasive diagnostic which utilizes the emission of electromagnetic waves by electrons in the presence of a magnetic field [43]. In a fusion plasma, high-energy electrons gyrate around the magnetic field lines, emitting radiation T_{rad} at the electron cyclotron frequency. This angular frequency ω_e is given by

$$\omega_e = \frac{eB}{m_e} ,$$

where e is the elementary charge, B the background magnetic field and m_e the electron mass. However, for high-temperature plasmas, where the thermal velocity of electrons is not negligible [44], additional terms appear stemming from the Doppler shift and the relativistic mass increase resulting in

$$\omega_e^w = \frac{eB}{m_e} \frac{1 - \beta_{\parallel} \cos(\theta)}{(1 - \beta^2)^{\frac{1}{2}}} ,$$

where θ is the angle between the emission and the magnetic field and β_{\parallel} is the ratio between the parallel velocity v_{\parallel} of the particle and the speed of light c . The upper term represents the Doppler shift which vanishes if the radiated emission is perpendicular to the magnetic field, whereas the lower term represents the relativistic mass increase that arises from multiplying the electron mass by the Lorentz factor. This frequency is labeled as the *warm* resonance since it takes the motion of fast electrons into consideration. Taking into account that the magnetic field is monotonically decreasing from the inner walls of the fusion device towards the outer walls, and that the gyration frequency depends on the magnetic field strength, each gyration frequency corresponds to a spatial position along a radial coordinate. Therefore, measuring the intensity of the radiation for different frequencies, spatially resolved measurements of electron temperature can be derived; more specifically, if the plasma is considered as a blackbody, for a Maxwellian velocity distribution perpendicular to the magnetic field, $T_{\text{rad}} = T_e$.

The intensity of a ray bundle dI per path element ds can be derived from the Beer-Lambert law (equation describing the radiation transfer through the absorbing and emitting plasma, [45]) and is defined as

$$\frac{dI_{\omega}}{ds} = j_{\omega} - \alpha_{\omega} I_{\omega} ,$$

where, j_{ω} and α_{ω} are the frequency-dependent emission and absorption coefficients, respectively. Assuming hot plasma conditions, that is $\hbar\omega \ll k_b T_e$, where \hbar is the reduced Planck constant, ω the gyration frequency of the electrons and k_b the Boltzmann constant, the Rayleigh-Jeans approximation (low frequency limit) holds true and the following approximation of the radiation intensity I_{ω} measured can be made

$$I_{\omega} \approx \frac{\omega^2 k_b T_e}{8\pi^3 c^2} .$$

This results in a frequency-dependent radiation intensity, which depends exclusively on the electron temperature. Now, to derive the local electron temperatures from the microwave emissivity in a fully relativistic approach, considering extra terms rising from relativistic thermal effects, the 3-D ray-tracing code TRAVIS is implemented. The radiative temperature is

calculated by summation of the contributions from all rays captured by the radiometer antenna. For this, TRAVIS solves ray-tracing equations, which are derived from the eikonal equation of ray optics as presented in [44]. Thus, by analyzing the emitted radiation, valuable information about the electron temperature and its spatial variation can be extracted. Further specifics on the ECE diagnostic commissioned in W7-X are mentioned in **Article I**, and a more in-depth description of this diagnostic can be found in [46].

Therefore, the ECE diagnostic allows one to use T_e fluctuations as tracers for the detection of turbulent transport processes and by monitoring the temporal evolution of these fluctuations, one can identify regions of enhanced or reduced confinement and gain insight into the dynamics of plasma instabilities and the underlying transport mechanisms. This information is vital for developing strategies to mitigate turbulent transport and improve plasma stability.

2.2.2 Soft X-ray multi-camera tomography system

The detection of spatio-temporally resolved instabilities and magneto-hydrodynamic mode dynamics is highly relevant for the investigation of plasma stability and confinement. For this, diagnostics capable of revealing 2-D and 3-D spatial distributions of plasma emissivities are attractive. For example, with an array of pinhole cameras aligned in a poloidal plane, the XMCTS can capture radiation emissions in a poloidal plasma cross-section, such that tomographic reconstructions of the radiation profiles are possible. Thus, plasma phenomena manifesting in fluctuations of the soft X-ray radiation might be identified and investigated. Specifics relevant to this work of the XMCTS commissioned in W7-X are mentioned in **Article II**, and more in-depth descriptions of the diagnostic can be found in [47, 48].

High-temperature plasmas emit radiation in a wide range of electromagnetic spectrum, including contributions from Coulomb collisions (electron-electron and electron-ion), recombination radiation and, most relevant to the XMCTS, bremsstrahlung. Although high-Z impurities significantly contribute with line radiation in the soft X-ray emissions, bremsstrahlung is the dominant source, stemming from the deflection or deceleration of charged particles by the interaction with an electric field or charged particle [49]. The equation for the bremsstrahlung can be derived from applying the Larmor formula and Fourier analysis for a single charged particle, and then extending this to consider a charged particle in a plasma, taking all collisions into account. This derivation is presented in detail in [50] and it is also shown that the bremsstrahlung is proportional to $n_e^2 \sqrt{T_e}$; therefore, the soft X-ray radiation is also $\propto n_e^2 \sqrt{T_e}$ and carries important information about the plasma's properties. For the detection of the radiation, silicon diode arrays are often employed with beryllium filters to block any incoming radiation outside the desired X-ray range.

A tool employed for the characterization of the fluctuating activity is the tomographic reconstruction of soft X-ray emissions. Since the XMCTS delivers a set of integrated (non-local) radiation measurements in a plasma cross-section, tomographic algorithms have to be employed to retrieve higher dimensional distributions. This can be achieved by considering several projections from different angles, that is, functions that compute the line-integrated plasma emissivity along several lines of sight [51]. For an exact reconstruction based on pro-

jections, an infinite number of them would be required. However, the number of available measurements is finite and can result in a set of different reconstructions that fit the data. Therefore, to identify the best representing reconstruction, assumptions about the 2-D distribution of the radiation must be made. To this end, in W7-X, Gaussian process tomography is employed. This method assumes that multiple solutions for the tomographic reconstruction exist in a Gaussian distribution of possible solutions. The most likely solution can be computed through Bayes' formula [52]

$$P(A|B) = \frac{P(B|A)P(A)}{P(B)},$$

where, $P(A)$ and $P(B)$ denote the *prior* probabilities of events A and B respectively (initial assumptions or knowledge about A and B), and $P(A|B)$ and $P(B|A)$ represents the *posterior* probabilities of A given B and B given A respectively (updated probabilities provided new evidence). For the case of soft X-ray tomographic reconstruction, Bayes' formula can be rewritten as

$$P(e|d, \theta) = \frac{P(d|e, \theta)P(e, \theta)}{P(d)},$$

where e denotes the underlying plasma emissivity, d is a distance metric in the tomographic reconstruction grid and θ represents the different model hyperparameters such as the shutter radial and poloidal positions. Therefore, the underlying unknown plasma emissivity distribution is treated as a Gaussian process and is evaluated along a discrete set of points (the tomographic reconstruction grid), resulting in a multi-dimensional Gaussian distribution. A detailed description of the tomographic inversion performed in W7-X can be found in [53].

2.2.3 Spatio-temporal fluctuation analysis

An alternative approach to characterize fluctuating activity is analyzing the magnetic displacement ξ resulting from the activity. Instabilities are related to perturbation of the plasma equilibrium and can be characterized by mode frequency ω , growth rate γ , poloidal and toroidal mode numbers (m, n) and ξ . The latter quantity is briefly described and analyzed in **Article III**; however, to highlight the correct interpretation of a displacement analysis, a qualitative analysis of ξ is deserving. More specifically, the expected ξ analysis results involving the presence of a magnetic island.

A sketch of the expected magnetic displacement results due to the presence of a magnetic island is shown in Fig. 4. As depicted in Fig. 4(a), a magnetic island rearranges the magnetic field topology by altering surrounding magnetic field lines. More specifically, by transversely bending them in the direction of least resistance. The magnetic field lines located closest to the X-point (where the field lines from opposite sides of the islands reconnect) suffer the strongest compression (blue and red dashed lines).

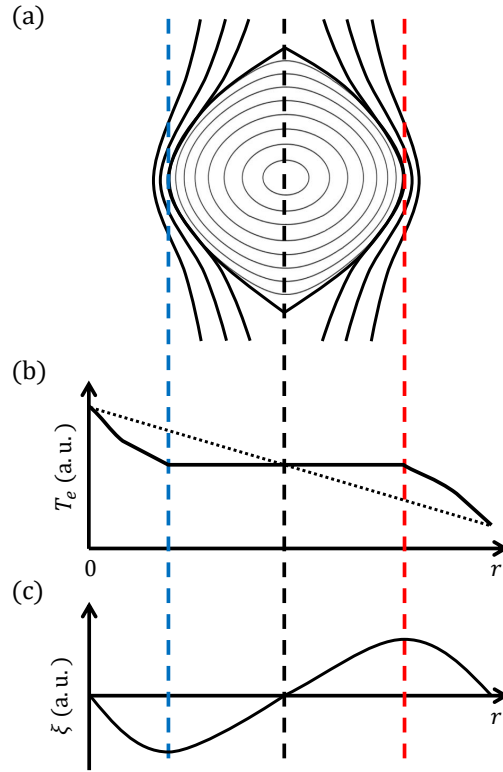


Fig. 4: Sketch of expected magnetic displacement results ξ due to the presence of a magnetic island. Depicted over the same arbitrary radial coordinate r are (a) the island altering surrounding magnetic flux surfaces, (b) the electron temperature with (black line) and without (black dotted line) the island and (c) ξ . Blue and red dashed lines indicate the radial positions at which the flux surfaces are maximally bent due to the island.

As seen from Fig. 4(b), for a monotonically decreasing electron temperature T_e in the $r > 0$ direction (dotted line), the compression of the magnetic field lines results in an inwards decrease of T_e and an outwards increase of T_e (solid line). This is since T_e is constant along a magnetic flux surface, thus their displacements result in the illustrated modification of the T_e profile. The minimum and maximum values of T_e are attained in the radial location where the magnetic compression are highest (blue and red dashed lines). Finally, this inwards and outwards compression of the magnetic field lines results in the magnetic displacement structure shown in Fig. 4(c). This structure goes along the new T_e profile due to the presence of the magnetic island. That is, ξ attains negative values at radial locations where T_e decreased, whereas positive ξ values are reached where T_e increased. Moreover, the minima and maxima of the T_e profiles and ξ agree with each other (blue and red dashed lines). Therefore, the analysis of the magnetic displacement indicates the direction of the compression of the magnetic field lines and also delivers information on the resulting modification of the T_e profile.

2.3 Numerical modelling

Numerical modeling assumes a versatile role providing valuable insights into potential scenarios that may arise from a given set of initial conditions. For instance, the initial step in modeling ideal MHD stability involves assessing the stability of magnetic equilibria against ideal MHD perturbations. This examination focuses on determining if any perturbations of this nature are prone to grow unstable. Additionally, by solving the equations of ideal MHD continuum on flux surfaces and utilizing Fourier transforms in the poloidal and toroidal directions, the MHD spectrum is obtained [54]. Analyzing the stable MHD spectrum enables us to understand the frequency space where waves can propagate, thereby evaluating the feasibility of phenomena such as Alfvén or sound waves at specific radial locations.

For a more physically complete analysis that considers non-ideal perturbations, more intricate models incorporating factors like resistivity, electron inertia and viscosity become necessary. Expanding on this point, a thorough yet more computationally demanding model such as a gyrokinetic model can be utilized. This would encompass solving the gyrokinetic equations for electrostatic and magnetic potentials for each mode, resulting in Fourier components from the fields as a function of time, radius and toroidal and poloidal angles. Hence, the growth rates of modes with fixed poloidal and toroidal mode numbers (m, n) can be computed and unstable modes can be identified. Furthermore, from the numerically obtained potentials through gyrokinetic simulations, a radial frequency analysis can be performed, providing deeper insights into mode dynamics and damping mechanisms. The role of presumed emerging magnetic islands, rotational transform ι and radial electric fields on the transitions to the CERC regime are assessed by appropriately incorporating these factors in the numerical simulations. The following section focuses on the aforementioned numerical methods employed to characterize fluctuating activity.

2.3.1 Ideal MHD

Ideal MHD is the standard tool for calculation of mode activities in tokamaks and stellarators [55,56]. The Finite-Element Fourier code package CAS3D (Code for the Analysis of the MHD Stability of 3-D Equilibria) allows the study of global MHD stability of 3-D toroidal plasmas [55, 57–59]. The kinetic (W_{kin}) and potential (W_{pot}) energies connected to a displacement vector ξ can be written as

$$W_{\text{kin}}(\xi) = \frac{1}{2} \int \int \int d^3r \rho |\xi|^2$$

$$W_{\text{pot}}(\xi) = \frac{1}{2} \int \int \int d^3r [|\mathbf{C}|^2 - A(\xi \cdot \nabla_s)^2 + \gamma_C \rho (\nabla \cdot \xi)^2] ,$$

where ρ denotes the equilibrium's mass density, \mathbf{C} is a term comprised by the perturbed magnetic field and a stabilizing term, \mathbf{A} is a term encompassing a potentially destabilizing contribution, s is a flux surface label, and γ_C is the ratio of the specific heats [57, 60]. CAS3D

solves the ideal MHD stability problem in general geometry by treating the ideal MHD energy principle in its variational form

$$\lambda W_{\text{kin}}(\xi) - W_{\text{pot}}(\xi) \longrightarrow \text{minimum} ,$$

where λ is the corresponding eigenvalue. A negative λ_{min} indicates an MHD unstable equilibrium. Therefore, the task of the CAS3D code is the numerical minimization of W_{pot} within a set of suitably normalized displacements ξ . For the case of a free-boundary calculation, the potential energy would also include the contributions of the vacuum energy and the vacuum-vessel interface. Therefore, the stability of equilibria against ideal perturbations can be tested.

2.3.2 MHD spectrum

One step further, to determine whether a plasma wave is expected to exist in a specific frequency range, the MHD spectrum, i.e. the spectra of Alfvén and sound waves, offers insight on the the frequency space in which these waves can propagate. The continua refer to the continuous range of frequencies over which waves can exist in the plasma. More specifically, the existence of the continuum leads to a damping of those modes which interact with the continuum, while modes with frequencies within open continuum gaps are global and remain undamped. Thus, gap structures are indicators for the emergence of a mode. For the calculation of the continuous Alfvén and sound spectrum, the 3-D ideal MHD continuum code CONTI can be employed. A detailed description of this code is found in [54]. Briefly summarized, the ideal MHD continuum equations are transformed into Boozer coordinates and Fourier decomposition of the perturbation on each flux surface is performed,

$$\xi_s = \sum_{(m,n)} \xi_{s(m,n)} \exp \left[2\pi i \left(m\theta + \frac{n}{N_p} \phi \right) \right] ,$$

where (m, n) are the poloidal and toroidal mode numbers respectively, θ represents the poloidal angle (varying between 0 and 1), ϕ denotes the toroidal angle (varying between 0 and N_p), and N_p is the number of periods of the device. Similarly, the equilibrium quantities are also decomposed into Fourier modes. The ideal MHD continuum equations can then be written in matrix form consisting of blocks of Fourier matrices resulting in an eigenvalue problem. In general, the eigenvalues determine the characteristic frequencies of the plasma waves, and the corresponding eigenvectors provide information about the mode shapes or spatial patterns of the waves. In this specific case, by analyzing the eigenfunctions, the CONTI code assigns the dominating Fourier harmonic to the different branches of eigenvalues. Furthermore, it determines if the eigenfunction is dominated by Alfvén or sound contributions. Therefore, this analysis results in the Alfvén and sound continua, indicating the frequency windows over the coordinate s at which modes are and are not expected to exist. Going one step further, the impact of adding presumed magnetic islands of different sizes at different locations can be included in the analysis performed with CONTI as shown in [61].

2.3.3 Gyrokinetic simulations

If ideal MHD stability studies do not conclusively yield an instability, the next natural step is the Mode stability analysis through a gyrokinetic model to include non-ideal perturbations. The rapid gyration of particles around magnetic field lines can make the analysis of the full particle motion computationally expensive and complex. In the gyrokinetic framework, a transformation is performed to remove this fast gyromotion leading to a set of equations (gyrokinetic equations) that describe the slower spatial and temporal variations of particle distributions in the presence of electromagnetic fields. The gyrokinetic equations account for kinetic effects, electromagnetic forces, and plasma self-consistency, which enable the study of plasma phenomena such as turbulence, instabilities, and transport processes with reduced computational complexity compared to fully kinetic simulations.

To formulate and implement the set of gyrokinetic equations (gyrokinetic Vlasov-Maxwell equation system) for plasma studies, the coordinate systems and the electric and magnetic field variables must be first defined. A detailed description and derivation of the gyrokinetic equation system can be found in [62]. In the Hamiltonian formulation (also called $p_{||}$ formulation), the phase-space variables in gyrocenter coordinates (denoted by a double bar) are the gyrocenter position $\bar{\mathbf{r}}$, the parallel momentum $\bar{p}_{||}$, the magnetic moment $\bar{\mu}$, and the gyrophase $\bar{\theta}$. This formulation is advantageous given that it simplifies the equations (by allowing gyro-averaging of the particle distribution function), reduces dimensionality, and improves numerical efficiency [63]. A perturbed magnetic field \mathbf{B}^* can be written in terms of the unperturbed equilibrium magnetic field \mathbf{B}_0 and the guiding center curvature drift as

$$\mathbf{B}^* = \mathbf{B}_0 + \frac{\bar{p}_{||}}{q} (\nabla \times \mathbf{b}) ,$$

where $\mathbf{b} = \frac{\mathbf{B}^*}{B^*}$. A gyrocenter perturbation potential $\bar{\Psi}$ can be written in terms of a perturbed electric field $\bar{\Phi}$ and the respective magnetic potential $\bar{\mathbf{A}}$ of the perturbed field as

$$\bar{\Psi} = \bar{\Phi} - \bar{v}_{||} \bar{A}_{||} .$$

Finally, the Vlasov equation for the gyrocenter distribution function is

$$\frac{d\bar{f}}{dt} = \frac{\partial \bar{f}}{\partial t} + \frac{d\bar{\mathbf{r}}}{dt} \cdot \nabla \bar{f} + \frac{d\bar{p}_{||}}{dt} \frac{\partial \bar{f}}{\partial \bar{p}_{||}} = 0 ,$$

and the time evolution of the particle coordinates including perturbed electromagnetic potentials is given by

$$\begin{aligned}\frac{d\bar{\mathbf{r}}}{dt} &= \mathbf{b}^* \frac{1}{m} (\bar{p}_{||} - q\langle\bar{A}_{||}\rangle) + \frac{1}{q\bar{B}_{||}^*} \mathbf{b} \times (\bar{\mu}\nabla B + q\nabla\langle\bar{\Psi}\rangle) , \\ \frac{d\bar{p}_{||}}{dt} &= -\mathbf{b}^* \cdot (\bar{\mu}\nabla B + q\nabla\langle\bar{\Psi}_{||}\rangle) , \\ \frac{d\bar{\mu}}{dt} &= 0 .\end{aligned}$$

To solve the gyrokinetic equations with multiple particle species (electrons, ions and fast ions) with self-consistent interaction of all species in an arbitrary 3-D geometry EUTERPE code can be employed [64]. EUTERPE is in principle the most physically complete code currently existing for the investigation of the physics of global modes in magnetic confinement fusion devices [65, 66]. To solve the partial differential equations numerically, a particle-in-cell method is employed. By these means, the motion of individual particles in a continuous phase space can be calculated, and the moments of the distribution function can then be evaluated on a fixed grid in space from the position and velocity of the particles. After integrating the equations of motion, a charge and current are assigned to the grid. Then, the field equations on the grid are solved. Finally, the fields from the mesh are interpolated to the particle locations and these fields act on the particles. Therefore, by iterating this process, EUTERPE allows a detailed numerical description of fast particles to investigate wave-particle interactions that can be used for perturbative stability analysis. EUTERPE has already been employed to address different physical problems, e.g. the simulation of the linear electrostatic and electromagnetic ion temperature gradient instability in stellarators Wendelstein 7-X and Large Helical Device (LHD) [67].

2.3.4 Radially resolved frequency analysis of simulated potential

EUTERPE delivers timetraces of simulated electrostatic potential, which can be analyzed to radially resolve frequencies and identify continuum branches [61, 68, 69]. The standard method for finding the frequency content of a signal is the Fourier Transform. That is, estimating the autocorrelation sequence and then obtaining the estimation of the power spectral density (PSD) by discrete time Fourier transform [70]. This technique is a non-parametric method, i.e. no assumption about the signal is made. However, its frequency resolution is limited by the signal length and resolving high frequencies can be computationally demanding. For damped signals, the spectral peaks get smeared out and the frequency estimations are inaccurate. However, parametric methods use a different approach. Instead of estimating the PSD from the data directly, these techniques model the data as the output of a linear system driven by white noise and then estimate the parameters of this model. These methods can therefore overcome the resolution limit of the Fourier Transform technique. An established parametric method is the MUSIC (Multiple Signal Classification). The following description closely follows the explanation of MUSIC presented in [71]. MUSIC first computes the autocovariance matrix R_p of the timeseries (assuming that the timeseries can be represented by a series of complex si-

sinusoids with additive white noise). This results in eigenvectors (V_1, \dots, V_p) with eigenvalues $(\lambda_1, \dots, \lambda_p)$. The eigenvectors (V_1, \dots, V_M) with largest eigenvalues form the signal subspace, whereas the remaining eigenvectors (V_{M+1}, \dots, V_p) form the noise subspace. Therefore, the signal subspace can be represented by group vectors of complex sinusoids $(e(f_1), \dots, e(f_M))$, where $e(f_i) = [1, e^{j2\pi f_i}, \dots, e^{j2\pi f_i M}]$. Finally, the PSD is estimated by

$$PSD(f_i) = \frac{1}{\Delta f \sum_{k=M+1}^p |e^T(f_i) V_k|^2} ,$$

where T is the length of the timeseries. It is important to note that one has to define the size of the noise subspace (parameter M), which can result in an under- as well as overestimation of the resulting PSD. Also, although the peaks in the PSD computed with the MUSIC method indicate the frequency locations of components in a timeseries, the magnitude of each peak does not indicate the spectral power at the corresponding frequency. An in-depth description of MUSIC can be found in [72]. Going one step further, this method has been extended to improve the frequency estimations of damped signals, resulting in the Damped MUSIC (DMUSIC, [73]) method.

3 Results

Following the structure presented in Fig. 1 (Chevron diagram, Section 1), this section focuses on the results obtained in the scientific articles presented. More specifically, **Article I** presents the validation of the entropy-based methods on plasma data, followed up by **Article II** showing the automated implementation of novelty detection analysis, and **Article III** provides the physics investigation of the spontaneous T_e transitions detected.

3.1 Article I

The complexity and dynamics of plasma behavior in fusion devices demand efficient and adequate methods for data analysis. In recent years, entropy-based methods have emerged as powerful tools for quantifying and characterizing the complexity and information content of plasma data. These methods, rooted in information theory, offer a novel approach to understanding underlying plasma dynamics, turbulence, and transport phenomena in plasmas. However, to ensure the accuracy and validity of these entropy-based methods, it is crucial to validate them against experimental data. The validation process involves comparing entropy measures with well-established plasma diagnostics and theoretical models. This comparison not only assesses the consistency and correlation between entropy measures and diagnostic signals but also validates the ability of entropy-based methods to capture key plasma characteristics. By demonstrating the effectiveness and utility of entropy-based methods, this research expands the toolbox of plasma data analysis techniques, contributing to the advancement of fusion research and the quest for practical fusion energy solutions.

Article I presents the results of employing different entropy-based coupling analysis techniques on fluctuating electron cyclotron emission signals, for the identification of radiation stemming from symmetric profiles. More specifically, the couplings between one reference ECE signal channel and all others is examined to find the radial location of the signal channel measuring the emission originating from the same flux surface, but in the opposite field-side. The techniques employed, that is the Pearson product-moment correlation (known as linear correlation), mutual information, partial mutual information and transfer entropy, all successfully achieve this. However, by comparing the results delivered by the different techniques, it is evident that the partial mutual information delivers the most robust results. That is, considering the influence of spurious signals stemming from the electron cyclotron resonance heating system, further couplings between the reference signal channel and channels measuring emissions from different flux surfaces fall below the significance threshold. The added value resulting from considering the influence of different signals on the couplings between two systems is further emphasized in the analysis taking the measurements of a neighboring channel as the conditioning in the PMI technique. In this manner, taking into account the information that is directly radially transferred to its surrounding, it is revealed how much information from a specific location can be found elsewhere. It is shown that the reference signal channel has a strong coupling with its neighboring channel and, even though this conditioning leads to a drastic decrease of the couplings between with all other signal channels,

couplings in the opposite field-side at similar radial locations can be identified. The results of spatial coupling confirm the position of the flux surfaces and, albeit these results do not perfectly match the ones delivered by MHD equilibrium calculations, these lie well within the error margins.

From the analysis presented in **Article I**, it is evident that the entropy-based techniques employed are well-suited for plasma data analysis and may even offer additional insight. The use cases shown in this article highlight the importance of discerning between physically and not physically relevant contributions to the dependencies between different systems. Therefore, carefully selecting the conditioning for the PMI analysis allows the investigation of intricate spatio-temporal couplings. Nevertheless, multi-layered coupling analysis of plasma data must be performed cautiously to be able to draw accurate conclusions and physical interpretations; this is, due to the complexity of the data analyzed. Further possible analysis employing the PMI technique include spatio-temporal coupling e.g. for the analysis of perpendicular heat flow and coupling analysis across different diagnostics to investigate dependencies between different plasma parameters. Thus, this article paves the way for future, more versatile, spatio-temporal coupling analysis.

3.2 Article II

Article II explores the application of entropy-based methods for data mining purposes in W7-X low-iota plasmas. By leveraging entropy as a measure of uncertainty and disorder, hidden patterns can be revealed, as well as dependencies between different plasma parameters and anomalies within plasma data. In other words, analyzing historical data through information flow measures, allows the identification of key parameters and control variables that significantly influence plasma behavior. Furthermore, fast and robust methods for data mining may allow real-time monitoring and analysis of plasma parameters, enabling rapid response and adaptive control in dynamic plasma environments.

Implementing PE analysis on all ECE and soft X-ray data available from several low-iota plasma discharges with evolving bootstrap current, resulted in the identification of low-frequency (up to 10kHz) intermittent fluctuation activity. These results were supported by spectral analysis, however the PE technique required significantly less computing time. The oscillations occurred in plasma discharges under different plasma conditions; however, in all cases studied, the oscillations appeared only in discharges with a two-step plasma heating scheme for plasma start-up. That is, employing only a limited number of gyrotrons at first, a time buffer was created in which the plasma started relaxing before getting heated at full performance. Additionally, in all cases presenting the fluctuations, this activity ceased during a stationary phase of the plasma, at which a spontaneous increase of core-electron temperature was observed. For the discharges analyzed, T_e increased up to 1.2keV. Surprisingly, the total diamagnetic energy w_{dia} remains unchanged after this transition, which hints to a redistribution of the electron pressure. This goes along the observation of the decrease of some soft X-ray measurements (since $\propto n_e^2 \sqrt{T_e}$). Thus PE analysis, through the analysis of ECE

and soft X-ray bulk data, allowed an efficient and automated detection of emerging fluctuation activity which revealed previously undetected spontaneous T_e transitions.

From the analysis presented in **Article II**, it is evident that permutation entropy is a powerful tool capable to deliver valuable insight regarding changes of the plasma states, requiring significantly less computing power than similar traditional methods. The hyperparameter τ_D was tailored for the data mining procedure conducted to optimally detect the fluctuation activity observed. However, one might perform this analysis in parallel (keeping the computing time low) for a set of different embedding delays to cover a broader range of fluctuation frequencies. Also, it is worth noting the importance of defining the significance threshold for the detection of anomalies. Although a statistical significance level for the permutation entropy can be derived from analyzing white noise signals, the significance threshold should be optimized for the data of interest. **Article II** shows how choosing appropriate parameters and defining well-suited significance thresholds for ECE and soft X-ray datasets allows the identification of previously undetected phenomena in an automated procedure. In other words, this investigation exemplifies the analysis of an information complexity measure for novelty detection in plasma data.

3.3 Article III

The fluctuating activity preceding the spontaneous T_e transitions reported in **Article II** are characterized in **Article III**. This is achieved by, first, employing experimental methods to investigate the dependency between the fluctuations and different plasma parameters, conducting spatio-temporal fluctuation analysis of ECE data, and analyzing soft X-ray tomographic reconstructions. Consequently, numerical methods are implemented. More specifically: first, ideal magneto-hydrodynamic (MHD) stability analysis are conducted to determine if the plasma equilibria investigated is susceptible to ideal MHD perturbations; second, the stable MHD spectrum for both Alfvén and sound waves including the effects of the presence of magnetic islands is explored; third, expanding on the ideal MHD analysis, mode stability analysis employing a fully gyrokinetic model including the effect of a radial electric field E_r is performed.

The mechanisms resulting in transitions to the CERC regime were investigated in W7-X plasma discharges. Spontaneous T_e transitions to higher core-electron temperatures were observable only in plasma experiments in the low-iota configuration ($\iota(r=0) = 0.75$), at which the plasma current evolved. These transitions, accompanied by a shift from negative to positive values of E_r close to the plasma center, offer the strongest evidence of a transition to CERC regime. From the ι evolution for discharges in the low- ι and standard configuration ($\iota(r=0) = 0.86$), it was shown that only for the case of low- ι the rotational transform crossed a rational value related to the five-fold symmetry in W7-X ($\iota = 5/7$), where *natural*, i.e. non-symmetry breaking, islands may appear. The crossing between this rational value and ι shifts, due to the evolution of ι and as shown in the literature [17–19] this plays a major role in the transition to the CERC regime. Further calculations to investigate these presumed magnetic islands are required. These can be performed employing the 3-D MHD-equilibrium code

HINT [61], in which a relaxation method based on the dynamic equations of the magnetic field and pressure are implemented. In this manner, one could evaluate if, under the experimental conditions at which the transitions were observed, magnetic islands are expected to form.

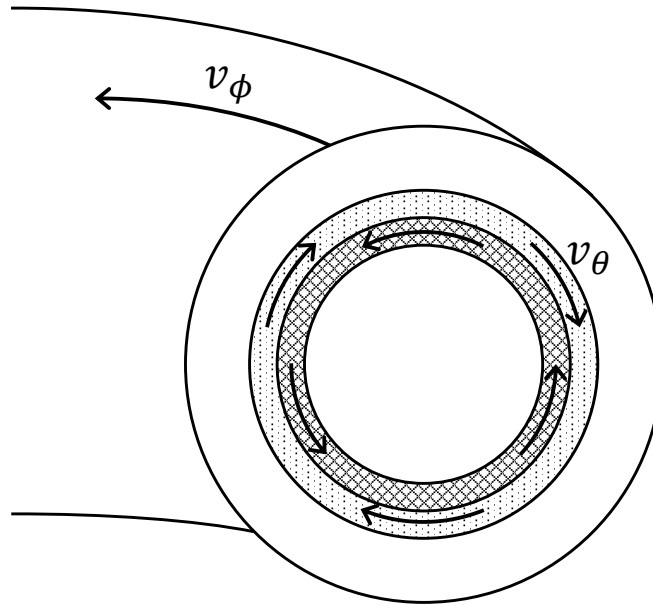


Fig. 5: Poloidal cross-section of a plasma depicting the poloidal v_θ and toroidal v_ϕ motion components of a zonal flow oscillation. Meshed and dotted regions indicate the positive and negative charges respectively, emerging due to e.g. a radially varying electrostatic potential.

The thorough characterization of the fluctuating activity preceding the T_e transition suggests this activity to be zonal flow oscillations. Zonal flow oscillations are poloidally symmetric potential perturbations, caused by a radially varying electrostatic potential and driven nonlinearly by microturbulence [74]. These oscillations are thus associated with a radial electric field, and the corresponding $\mathbf{E} \times \mathbf{B}$ flow lies in the poloidal direction as illustrated in Fig. 5. This direction changes in sign with the radius. Zonal flows do not contribute to radial transport and even limits it [75]. This is attributed to a key element in the dynamics of zonal flows, which is the process of shearing of turbulent eddy currents by flows with shear lengths larger than eddy scales [76]. This shearing tilts the eddies, narrowing their radial extent and elongating them. As a consequence, the eddies necessarily must increase the strength of their coupling to small scale dissipation, thus tending to a suppression of the driving process. Therefore, the zonal flow oscillations are mechanisms of self-regulation of drift wave turbulence. Moreover, shear flows such as zonal flows can trigger spontaneous transitions to the high-confinement regime (also called *H-mode*) [77–80], which has been observed in tokamaks [81] as well as in stellarators [82, 83]. In H-mode, the plasma experiences a transition characterized by the formation of an edge transport barrier. This barrier reduces the radial transport of particles and heat from the plasma edge to the core, resulting in an improved confinement [84, 85].

From the evidence gathered, the oscillations observed in W7-X were triggered by a sudden increase of the heating power and vanished to the transition to the CERC regime. The disappearance is suspected to happen because of the new transport conditions attained in the CERC regime. Even though, it is not conclusive if the oscillations have a causal effect on the T_e transition, the identification and characterization of this activity is highly interesting, as it offers insight on the conditions at which these zonal flow oscillations might be found. This is of high relevance given that zonal flow oscillations play an important role in the physics of anomalous transport (e.g. the regulation of transport and turbulence levels [76, 86, 87]).

4 Conclusion

The goal of this thesis was to deepen our understanding regarding transitions to the core-electron-root-confinement regime in Wendelstein 7-X. This was achieved by assessing the analysis of various entropy-based complexity measures for the analysis of plasma data in W7-X. The assessment consisted of three phases: first, the validation of a suite of information-theoretic methods for plasma data analysis (**Article I**); second, their implementation on bulk plasma data for novelty detection (**Article II**); and third, the investigation of these new findings (**Article III**).

Article I provides substantial evidence of the feasibilities, added values and constraints of the techniques presented. The partial mutual information analysis delivers the most robust and insightful spatio-temporal coupling analysis results. This is, due to its capability of accounting for the influence of external sources on the mutual dependencies between systems. However, their physical interpretation must undergo close scrutiny to draw accurate and pertinent conclusions about the underlying mechanisms.

Article II unveils the potential of permutation entropy analysis for the fast and automated detection of plasma anomalies. More specifically, the detection of localized T_e fluctuations in low-iota configuration W7-X discharges, demonstrates the capability of detecting precursors of plasma state changes delivering results well-suited for real-time monitoring and inducing plasma control actions. Also, by selecting adequate hyperparameters, the method can be set to specifically detect phenomena occurring at particular time scales. This feature is highly attractive, since it serves as an intrinsic filter to uncover plasma behavior occurring at different characteristic times. This analysis is most adequate as a first step analysis, nevertheless it relies on subsequent analysis for the identification and characterization of the detected phenomena.

Article III offers a thorough investigation of the adiabatic, core T_e transition resulting in a deeper understanding of the role of τ and E_r , on the spontaneous transition to core-electron-root-confinement and the preceding oscillating activity. Evidence is provided that rational surfaces moving through the plasma in cause of their reaction to shielding current evolution may trigger the transition to electron-root transport regimes in W7-X, as seen in H-J and TJ-II. Therefore, the results presented deepen our understanding of underlying physical phenomena relevant to bifurcations of transport regimes. Although we offer an explanation for the preceding fluctuation activity, it is evident that further analysis need to be performed to conclusively state that the observations were in fact zonal flow oscillations.

5 Outlook: towards real-time novelty detection

The evidence provided in this thesis contributes to the identification of actuators that could compromise the plasma confinement and should be taken into account for the development of future reactor-relevant favorable plasma scenarios. To exemplify future investigations employing the novelty detection method presented in **Article II**, the implementation of the permutation entropy method for the detection of a possible precursor signal of a plasma terminating event is presented in Fig. 7. More specifically, PE is employed to analyze ECE data measured in a high-iota configuration plasma is presented, in which MHD activity was driven by electron cyclotron current drive (ECCD).

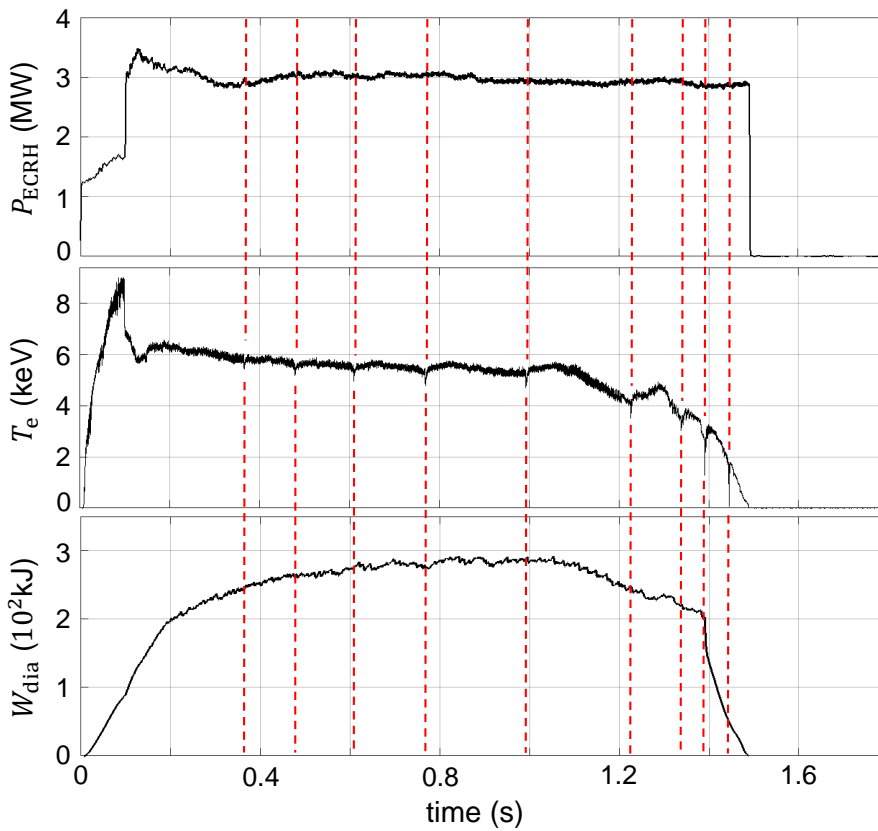


Fig. 6: Time traces of high iota configuration plasma discharge 20171123.30 in W7-X. Top-to-bottom: electron cyclotron heating power P_{ECRH} , electron temperature T_e and diamagnetic energy W_{dia} . Red dashed lines indicate instances of recurring sudden drops of T_e .

Through compensating or counteracting the plasma currents, ECCD can be employed to steer the strike lines and redistribute the power deposition on the divertors [88]. However, with varying plasma current, MHD instabilities such as sawtooth crashes are prone to emerge due to the change in the local rotational transform profile caused by very localized current drive [89, 90]. In W7-X, these recurring sudden drops of T_e with sawtooth shaped waveforms

have been detected, including oscillating precursors in ECE and soft X-ray measurements preceding the sawtooth instabilities [90]. Fig. 6 shows an overview plot of W7-X plasma discharge 20171123.30, in which sawtooth crashes were observed (red dashed lines). In this case, these are slow and unevenly long periodic dips of the T_e with a fast recuperation after reaching a local minima. It can be seen that the diamagnetic energy starts decaying at $t \approx 1.05$ s and thereon T_e does not fully recuperate after each dip until the plasma terminates.

The PE analysis conducted on ECE data, gathered from all available channels, reveals structures in the signals at various time points throughout the discharge, extending along the normalized effective radius ρ (see Fig. 7). In this analysis, PE values were calculated at a rate of $5.7 \cdot 10^6 \text{ s}^{-1}$ (calculation speed of the PE method). Clear structures are detected through PE at $t \in [1.05, 1.20]$ s, which are mirrored w.r.t. the plasma center. Other fainter structures are detected, namely: at $-0.3 < \rho < -0.2$ preceding dips in T_e (gray dashed lines, $t \in [0.3, 1.0]$ s), right before plasma termination across the whole plasma ($t \in [1.37, 1.50]$ s) and after plasma termination in the low-field side ($t > 1.5$ s).

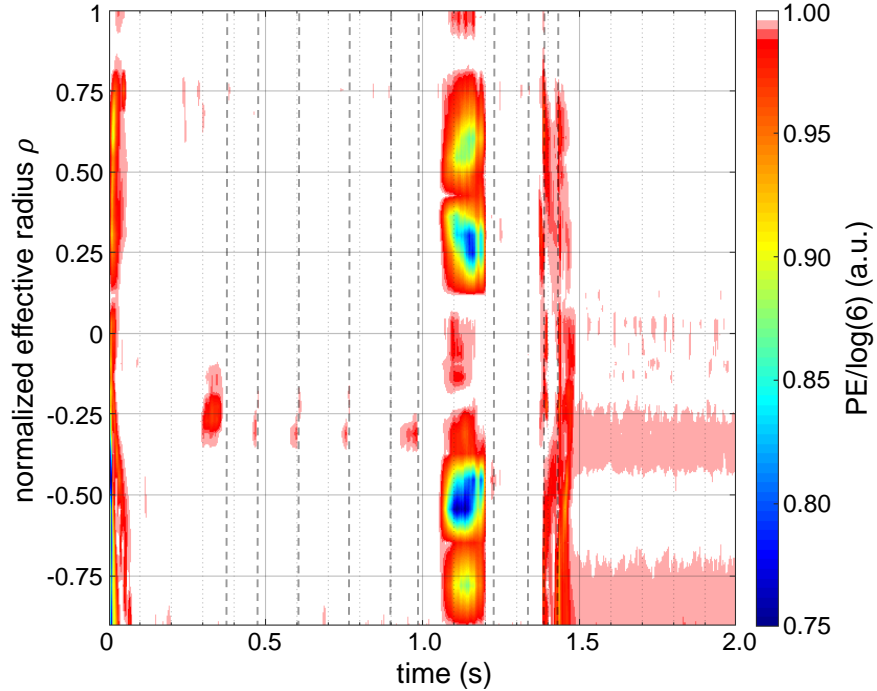


Fig. 7: Permutation entropy analysis of ECE radiation measurements from plasma discharge 20171123.30 in W7-X with permutation order $m = 3$ and embedding delay $\tau_D = 0.1$ ms. The data plot is normalized to the maximum achievable entropy. Gray dashed lines indicate instances of recurring sudden drops of T_e .

To further understand the structures detected through the PE, the waveforms analyzed are shown in Fig. 8. From Fig. 8(a) we observe the time trace of a central ECE signal channel (top) plotted in the same time window as the PE analysis (bottom). From this figure we observe that

the predominant structures in the PE contour-plot ($t \in [1.06, 1.20]$ s) appear as T_e decreases and reaches a new lower stable value. Employing a significance of 99.7%, this structure was first detected at $t = 1.08$ s (black line) and the data required for the detection is indicated by the gray shaded region. The structures observed prior to plasma termination ($t \in [1.37, 1.50]$ s) exhibit a wider distribution along ρ and are seemingly linked to short timed drops of T_e .

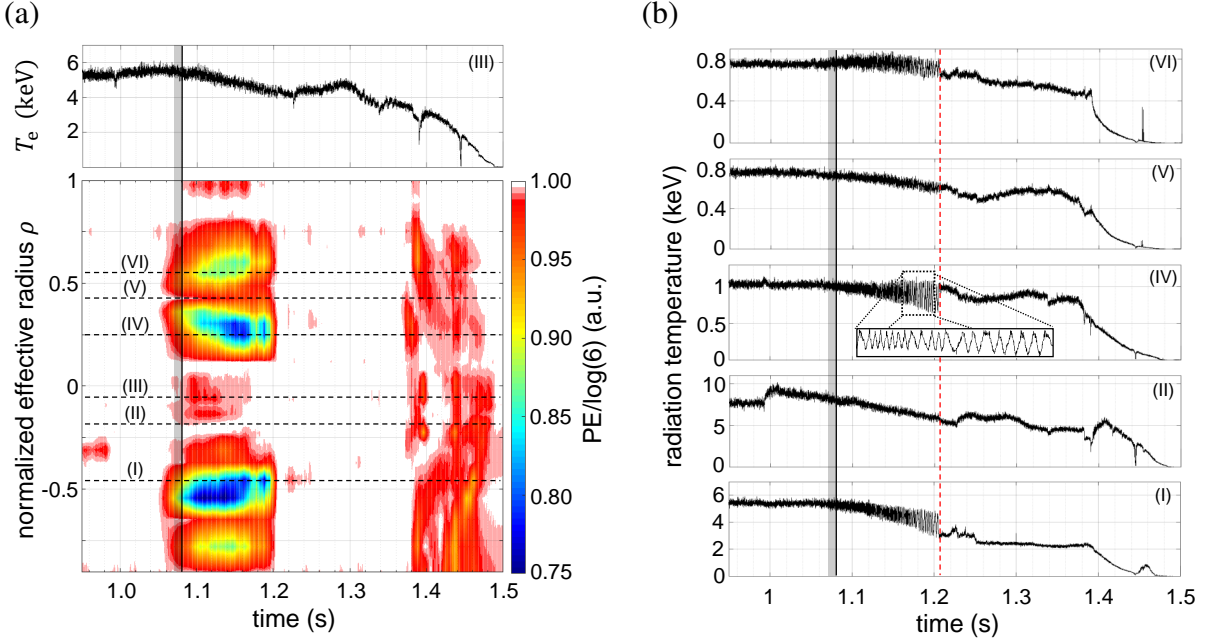


Fig. 8: (a) T_e measurements of a central ECE channel ($\rho = -0.07$, top) and PE analysis for all ECE channels (bottom) from $t = 0.95$ s to $t = 1.50$ s of plasma discharge 20171123.30 in W7-X. Black line indicates instance when MHD activity is first detected through PE method (99.7% significance). Gray shaded area displays time window containing the data analyzed for this detection. Black dashed horizontal lines pinpoint radial allocation of different ECE signals measured during the same time window. These signals are shown in (b). Magnification of signal (IV) revealing a down-chirp which vanishes at $t = 1.21$ s (red dashed line).

Further radially allocated radiation temperature time traces (black dashed horizontal lines) are shown in Fig. 8(b). From naked eye observations, with $t \in [1.06, 1.20]$ s we notice coherent fluctuations in the waveforms of the signals with lower PE values (I, III, IV and VI). A magnification of signal (IV) within this time window unveils the structure detected through PE in Fig. 8(a), a down-chirp (slowing down from $f = 2$ kHz to $f = 0.2$ kHz). The down-chirp vanishes at $t = 1.21$ s (red dashed line) preceding the last sawtooth crash that leads to plasma termination. Thus, this exemplifies the detection of a possible precursor signal of a plasma terminating event and highlights the feasibility of building a real-time plasma monitoring diagnostic based on permutation entropy. This example provides an outlook to apply information flow analysis as a valuable tool in fusion research for further enhancing our understanding of transport phenomena.

References

- [1] T. Hamacher, M. Huber, J. Dorfner, et al. Nuclear fusion and renewable energy forms: Are they compatible? *Fusion Eng. Des.*, 88(6):657–660, 2013.
- [2] ITER Organization. Advantages of fusion. <https://www.iter.org/sci/Fusion>. Retrieved 2023, June 22.
- [3] E. Peluso, E. Pakhomova and M. Gelfusa. New challenges in nuclear fusion reactors: From data analysis to materials and manufacturing. *Appl. Sci.*, 13(10):6240, 2023.
- [4] M. Keilhacker, A. Gibson, C. Gormezano, et al. The scientific success of JET. *Nucl. Fusion*, 41(12):1925, 2001.
- [5] K. Tomabechi, J. R. Gilleland, Yu. A. Sokolov, et al. ITER conceptual design. *Nucl. Fusion*, 31(6):1135, 1991.
- [6] G. Arnoux, I. Balboa, M. Clever, et al. Power handling of the JET ITER-like wall. *Phys. Scr.*, 2014(T159):014009, 2014.
- [7] S. N. Gerasimov, P. Abreu, G. Artaserse, et al. Overview of disruptions with JET-ILW. *Nucl. Fusion*, 60(6):066028, 2020.
- [8] U.S. Department of Energy. DOE national laboratory makes history by achieving fusion ignition. <https://www.energy.gov/articles/doe-national-laboratory-makes-history-achieving-fusion-ignition>. Retrieved 2023, June 22.
- [9] N. B. Meezan, M. J. Edwards, O. A. Hurricane, et al. Indirect drive ignition at the National Ignition Facility. *Plasma Phys. Control. Fusion.*, 59(1):014021, 2016.
- [10] R. S. Craxton, K. S. Anderson, T. R. Boehly, et al. Direct-drive inertial confinement fusion: A review. *Phys. Plasmas*, 22(11):110501, 2015.
- [11] R. J. Pearson and S. Takeda. Review of approaches to fusion energy. In *Commercialising Fusion Energy*, 2053-2563, pages 1 – 31. IOP Publishing, 2020.
- [12] J. Nührenberg and R. Zille. Stable stellarators with medium β and aspect ratio. *Phys. Lett. A*, 114(3):129–132, 1986.
- [13] F. Wagner and H. Wobig. Magnetic confinement. In A. Dinklage, T. Klinger, G. Marx, and L. Schweikhard, editors, *Plasma Physics: Confinement, Transport and Collective Effects*, pages 375 – 397. Springer, Berlin Heidelberg, 2005.
- [14] H. Maassberg, C. D. Beidler, U. Gasparino, et al. The neoclassical “electron root” feature in the Wendelstein-7-AS stellarator. *Phys. Plasmas*, 7(1):295–311, 2000.

-
- [15] M. Yokoyama, H. Maaßberg, C.D. Beidler, et al. Core electron-root confinement (CERC) in helical plasmas. *Nucl. Fusion*, 47(9):1213, 2007.
- [16] H. E. Mynick and W. N. G. Hitchon. Effect of the ambipolar potential on stellarator confinement. *Nucl. Fusion*, 23(8):1053, 1983.
- [17] N. Kenmochi, T. Minami, T. Mizuuchi, et al. Reformation of the electron internal transport barrier with the appearance of a magnetic island. *Sci. Rep.*, 10(1):5, 2020.
- [18] T. Estrada, D. López-Bruna, A. Alonso, et al. Electron Internal Transport Barriers and Magnetic Topology in the Stellarator TJ-II. *Fusion Sci. Technol.*, 50(2):127–135, 2006.
- [19] T. Estrada, F. Medina, D. López-Bruna, et al. Transitions to improved core electron heat confinement triggered by low order rational magnetic surfaces in the stellarator TJ-II. *Nucl. Fusion*, 47(4):305, 2007.
- [20] S. Ohshima, 2022-08. Personal communication.
- [21] G. Pautasso, C. Tichmann, S. Egorov, et al. On-line prediction and mitigation of disruptions in ASDEX Upgrade. *Nucl. Fusion*, 42(1):100, 2002.
- [22] V. Škvára, V. Šmídl, T. Pevný, et al. Detection of Alfvén eigenmodes on COMPASS with generative neural networks. *Fusion Sci. Technol.*, 76(8):962–971, 2020.
- [23] D. R. Ferreira, P. J. Carvalho, C. Sozzi, et al. Deep learning for the analysis of disruption precursors based on plasma tomography. *Fusion Sci. Technol.*, 76(8):901–911, 2020.
- [24] E. Aymerich, G. Sias, F. Pisano, et al. Disruption prediction at JET through deep convolutional neural networks using spatiotemporal information from plasma profiles. *Nucl. Fusion*, 62(6):066005, 2022.
- [25] D. Jordan, G. Stockmanns, and E. Kochs. Permutation entropy of the EEG indicates increase and decrease of the anesthetic level. *Anesthesiology*, 107(6):A800, 2007.
- [26] M. Henry and G. Judge. Permutation entropy and information recovery in nonlinear dynamic economic time series. *Econometrics*, 7(1):2225–1146, 2019.
- [27] J. E. Maggs, T. L. Rhodes and G. J. Morales. Chaotic density fluctuations in L-mode plasmas of the DIII-D tokamak. *Plasma Phys. Control. Fusion*, 57(4):045004, 2015.
- [28] C. Beidler, G. Grieger, F. Herrnegger, et al. Physics and engineering design for Wendelstein 7-X. *Fus. Technol.*, 17(1):148–168, 1990.
- [29] T. S. Pedersen, M. Otte, S. Lazerson, et al. Confirmation of the topology of the Wendelstein 7-X magnetic field to better than 1:100,000. *Nat. Commun*, 7(1):13493, 2016.

References

- [30] V. Nakariakov. Introduction to MHD. https://warwick.ac.uk/fac/sci/physics/research/cfsa/people/valery/teaching/khu_mhd. Retrieved 2023, June 22.
- [31] J. Howard. *Magnetohydrodynamics*, chapter 6, pages 135–138. Australian National University, 2002.
- [32] V. V. Nemov, S. V. Kasilov, W. Kernbichler, et al. The ∇B drift velocity of trapped particles in stellarators. *Phys. Plasmas*, 12(11):112507, 2005.
- [33] R. C. Wolf. A stellarator reactor based on the optimization criteria of Wendelstein 7-X. *Fusion Eng. Des.*, 83(7):990–996, 2008. Proceedings of the Eight International Symposium of Fusion Nuclear Technology.
- [34] R. C. Wolf, et al. Major results from the first plasma campaign of the Wendelstein 7-X stellarator. *Nucl. Fusion*, 57(10):102020, 2017.
- [35] C. E. Shannon. A mathematical theory of communication. *Bell Syst. Tech. J.*, 27(3):379, 1948.
- [36] S. Frenzel and B. Pompe. Partial mutual information for coupling analysis of multivariate time series. *Phys. Rev. Lett.*, 99(20):204101, 2007.
- [37] T. Schreiber. Measuring information transfer. *Phys. Rev. Lett.*, 85(2):461, 2000.
- [38] L. Cao and A. S. Soofi. Nonlinear deterministic forecasting of daily dollar exchange rates. *Int. J. Forecast.*, 15(4):421–430, 1999.
- [39] M. Paluš and S. Aneta. Direction of coupling from phases of interacting oscillators: An information-theoretic approach. *Phys. Rev. E*, 67(5):055201, 2003.
- [40] A. Murari, M. Lungaroni, M. Peluso, et al. On the use of transfer entropy to investigate the time horizon of causal influences between signals. *Entropy*, 20(9):627, 2018.
- [41] B. Ph. van Milligen, U. Höfel, J. H. Nicolau, et al. Study of radial heat transport in W7-X using the transfer entropy. *Nucl. Fusion*, 58(7):076002, 2018.
- [42] J. H. Nicolau, L. Garcia, B. A. Carreras, et al. Applicability of transfer entropy for the calculation of effective diffusivity in heat transport. *Phys. Plasma*, 25:102304, 2018.
- [43] I. H. Hutchinson. *Principles of Plasma Diagnostics*, chapter 5, pages 158–166. Cambridge University Press, New York, 2002.
- [44] N. B. Marushchenko, Y. Turkin, and H. Maassberg. Ray-tracing code TRAVIS for ECR heating, EC current drive and ECE diagnostic. *Comput. Phys. Commun.*, 185(1):165–176, 2014.
- [45] D. F. Swinehart. The beer-lambert law. *J. Chem. Educ.*, 39(7):333, 1962.

-
- [46] U. Höfel, M. Hirsch, S. Kwak, et al. Bayesian modeling of microwave radiometer calibration on the example of the Wendelstein 7-X electron cyclotron emission diagnostic. *Rev. Sci. Instrum.*, 90(4):043502, 2019.
- [47] C. Brandt, T. Broszat, H. Thomsen, et al. Installation of the soft x-ray multi-camera tomography system (XMCTS) in the Wendelstein 7-X stellarator. *Fusion Eng. Des.*, 123:887, 2017.
- [48] C. Brandt, J. Schilling, H. Thomsen, et al. Soft x-ray tomography measurements in the Wendelstein 7-X stellarator. *Plasma Phys. Control. Fusion*, 62(3):035010, 2020.
- [49] H. A. Bethe and L. C. Maximon. Theory of bremsstrahlung and pair production. I. differential cross section. *Phys. Rev.*, 93(4):768–784, 1954.
- [50] L. M. Young. Bremstrahlung. In *Plasma astrophysics: radiative processes and high energy astrophysics*. pages 19-23. <http://kestrel.nmt.edu/~lyoung/426/Chap4.pdf>. Retrieved 2022, June 16.
- [51] R. M. Lewitt. Reconstruction algorithms: Transform methods. *Proc. IEEE*, 71(3):390–408, 1983.
- [52] J. Joyce. Bayes’ Theorem. In E. N. Zalta, editor, *The Stanford Encyclopedia of Philosophy*. Metaphysics Research Lab, Stanford University, 2021.
- [53] J. Schilling, H. Thomsen, C. Brandt, et al. Soft x-ray tomograms are consistent with the magneto-hydrodynamic equilibrium in the Wendelstein 7-X stellarator. *Plasma Phys. Control. Fusion.*, 63(5):055010, 2021.
- [54] A. Könies and D. Eremin. Coupling of Alfvén and sound waves in stellarator plasmas. *Phys. Plasmas*, 17(1):012107, 2010.
- [55] C. Nührenberg. Compressional ideal magnetohydrodynamics: Unstable global modes, stable spectra, and Alfvén eigenmodes in Wendelstein 7-X-type equilibria. *Phys. Plasmas*, 6(1):137–147, 1999.
- [56] C. Z. Cheng and M. S. Chance. Nova: A nonvariational code for solving the mhd stability of axisymmetric toroidal plasmas. *J. Comput. Phys.*, 71(1):124–146, 1987.
- [57] C. Schwab. Ideal magnetohydrodynamics: Global mode analysis of three-dimensional plasma configurations. *Phys. Fluids*, 5(9):3195–3206, 1993.
- [58] C. Nührenberg. Global ideal magnetohydrodynamic stability analysis for the configurational space of Wendelstein 7-X. *Phys. Plasmas*, 3(6):2401–2410, 1996.
- [59] C. Nührenberg. Free-boundary ideal MHD stability of W7-X divertor equilibria. *Nucl. Fusion*, 56(7):076010, 2016.

- [60] P. Merkel, C. Nuehrenberg and W. A. Cooper. Free-boundary ideal MHD modes in W7-AS. Technical report, Switzerland, 1996.
- [61] A. Könies, J. Cao, R. Kleiber et al. A numerical approach to the calculation of the Alfvén continuum in the presence of magnetic islands. *Phys. Plasmas*, 29(9):092102, 2022.
- [62] T. B. Fehér. *Simulation of the interaction between Alfvén waves and fast particles*. Ph.D. Thesis, Greifswald, 2013.
- [63] A. J. Brizard and T. S. Hahm. Foundations of nonlinear gyrokinetic theory. *Rev. Mod. Phys.*, 79(2):421–468, 2007.
- [64] M. Cole, A. Mishchenko, A. Könies, et al. Fluid electron, gyrokinetic ion simulations of linear internal kink and energetic particle modes. *Phys. Plasmas*, 21(7):072123, 2014.
- [65] A. Mishchenko, M. Borchardt, M. Cole, et al. Global linear gyrokinetic particle-in-cell simulations including electromagnetic effects in shaped plasmas. *Nucl. Fusion*, 55(5):053006, 2015.
- [66] R. Kleiber, R. Hatzky, and A. Könies. An explicit large time step particle-in-cell scheme for nonlinear gyrokinetic simulations in the electromagnetic regime. *Phys. Plasmas*, 23(3):032501, 2016.
- [67] P. Helander, T. Bird, F. Jenko, et al. Advances in stellarator gyrokinetics. *Nucl. Fusion*, 55(5):053030, 2015.
- [68] R. Kleiber, M. Borchardt, A. Könies, et al. Modern methods of signal processing applied to gyrokinetic simulations. *Plasma Phys. Control. Fusion.*, 63(3):035017, 2021.
- [69] A. Könies, C. Slaby, R. Kleiber, et al. The MHD continuum with a radial electric field. *Phys. Plasmas*, 27(12):122511, 2020.
- [70] H. Zhao and L. Gui. Nonparametric and parametric methods of spectral analysis. *MATEC Web Conf.*, 283:07002, 2019.
- [71] National Instruments Corporation. Using the music method (advanced signal processing toolkit). <https://www.ni.com/docs/de-DE/bundle/labview-advanced-signal-processing-toolkit-api-ref>. Retrieved 2023, June 20.
- [72] P. Stoica and M. L. Randolph. *Spectral Analysis of Signals*. Prentice Hall, 2005.
- [73] Y. Li, J. Razavilar and K. J. Ray Liu. A high-resolution technique for multidimensional nmr spectroscopy. *IEEE. Trans. Biomed. Eng.*, 45(1):78–86, 1998.
- [74] A. Mishchenko and R. Kleiber. Zonal flows in stellarators in an ambient radial electric field. *Phys. Plasmas*, 19(7):072316, 2012.

-
- [75] G. Birkenmeier, M. Ramisch, B. Schmid, et al. Experimental evidence of turbulent transport regulation by zonal flows. *Phys. Rev. Lett.*, 110:145004, 2013.
- [76] P. H. Diamond, S-I Itoh, K. Itoh, et al. Zonal flows in plasma — a review. *Plasma Phys. Control. Fusion*, 47(5):R35, 2005.
- [77] P. Manz, G. Xu, B. N. Wan, et al. Zonal flow triggers the L-H transition in the Experimental Advanced Superconducting Tokamak. *Phys. Plasmas*, 19(7):072311, 07 2012.
- [78] G. D. Conway, C. Angioni, F. Ryter, et al. Mean and oscillating plasma flows and turbulence interactions across the $L-H$ confinement transition. *Phys. Rev. Lett.*, 106(6):065001, 2011.
- [79] Z. Yan, G. R. McKee, R. Fonck, et al. Observation of the $L-H$ confinement bifurcation triggered by a turbulence-driven shear flow in a tokamak plasma. *Phys. Rev. Lett.*, 112(12):125002, 2014.
- [80] L. Schmitz, L. Zeng, T. L. Rhodes, et al. Role of zonal flow predator-prey oscillations in triggering the transition to H-mode confinement. *Phys. Rev. Lett.*, 108(15):155002, 2012.
- [81] F. Wagner. The history of research into improved confinement regimes. *Eur. Phys. J. H*, 43(4), 2018.
- [82] F. Wagner, J. Baldzuhn, R. Brakel, et al. H-mode of W7-AS stellarator. *Plasma Phys. Control. Fusion*, 36(7A):A61, 1994.
- [83] S. Morita, T. Morisaki, M. Goto, et al. H-mode-like transition and ELM-like bursts in LHD with thick ergodic layer. *Nucl. Fusion*, 47(8):1033, 2007.
- [84] F. Wagner, G. Fussmann, T. Grave, et al. Development of an edge transport barrier at the H-mode transition of ASDEX. *Phys. Rev. Lett.*, 53(15):1453–1456, 1984.
- [85] P. T. Lang, A. Loarte, G. Saibene, et al. ELM control strategies and tools: status and potential for ITER. *Nucl. Fusion*, 53(4):043004, 2013.
- [86] H. Sugama and T.-H. Watanabe. Collisionless damping of zonal flows in helical systems. *Plasma Phys. Control. Fusion.*, 13(1):012501, 2006.
- [87] T. H. Watanabe, H. Sugama, S. Ferrando-Margalet, et al. Reduction of turbulent transport with zonal flows enhanced in helical systems. *Phys. Rev. Lett.*, 100(19):195002, 2008.
- [88] Y. Gao, J. Geiger, and M. W. Jakubowski. Effects of toroidal plasma current on divertor power depositions on Wendelstein 7-X. *Nucl. Fusion*, 59(10):106015, 2019.
- [89] Y. Nagayama, K. Kawahata, S. Inagaki, et al. Sawtooth oscillation in current-carrying plasma in the large helical device. *Phys. Rev. Lett.*, 90(20):205001, 2003.

References

- [90] M. Zanini, H. P. Laqua, H. Thomsen, et al. ECCD-induced sawtooth crashes at W7-X. *Nucl. Fusion*, 60(10):106021, 2020.

A. Thesis Articles

Authors contributions

Article I

Flux surface identification by spatio-temporal coupling with partial mutual information analysis of electron cyclotron emission data

J. F. Guerrero Arnaiz, A. Dinklage, B. Pompe, J. Geiger, M. Hirsch, U. Höfel, N. Marushchenko, Y. Turkin, R. C. Wolf and the W7-X Team

Plasma Physics and Controlled Fusion, Vol. 63.015002 (2021), DOI: 10.1088/1361-6587/abc2e1

J. F. Guerrero Arnaiz is responsible for the manuscript, designing, validating and implementing the suite of spatio-temporal coupling analysis methods (including Pearson's correlation, mutual information, partial mutual information and transfer entropy), for the analysis of electron cyclotron emission (ECE) data. The mathematical formulation of the methods was achieved in collaboration with B. Pompe. The ECE data and T_e profiles were provided by U. Höfel. The discussion of the results and the final editing of the article was a close collaboration between J. F. Guerrero Arnaiz and all the co-authors listed.

Article II

Fast characterization of plasma states in W7-X with permutation entropy

J. F. Guerrero Arnaiz, A. Dinklage, J. Geiger, M. Hirsch, U. Höfel, C. Brandt, H. Thomsen, J. Schilling, K. Rahbarnia, U. Neuner, M. Zanini and the W7-X Team

Plasma Physics and Controlled Fusion, Vol. 64.084005 (2022), DOI: 10.1088/1361-6587/ac7a5d

J. F. Guerrero Arnaiz is responsible for the manuscript, the development and implementation of the tool based on permutation entropy for the analysis of bulk plasma data. Additionally, J. F. Guerrero Arnaiz is accountable for the analysis of the experimental data acquired through the ECE diagnostic (in collaboration with M. Hirsch and U. Höfel) and the soft X-ray diagnostic (in collaboration with H. Thomsen, C. Brandt and J. Schilling). The discussion of the results and the final editing of the article was a close collaboration between J. F. Guerrero Arnaiz and all the co-authors listed.

Article III

Spontaneous transitions to high core-electron temperatures in W7-X low-iota plasmas close to electron-root condition

J. F. Guerrero Arnaiz, A. Dinklage, A. Könies, C. Nührenberg, A. Zocco, H. Bouvain, M. Borchardt, C. Brandt, N. Chaudhary, J. Geiger, M. Hirsch, R. Kleiber, K. Rahbarnia, A. Mishchenko, H. Thomsen, M. Zanini and the W7-X Team

Plasma Physics and Controlled Fusion, Submitted for publication July 2023

J. F. Guerrero Arnaiz is responsible for the manuscript and the analysis of the experimental

data acquired through the electron cyclotron emission diagnostic (in collaboration with M. Hirsch and N. Chaudhary) and the soft X-ray diagnostic (in collaboration with H. Thomsen and C. Brandt). That is, the computation and analysis of the rotational transform evolution (in collaboration with A. Dinklage), the derivation of plasma profiles (in collaboration with H. Bouvain) and the investigation of the magnetic field displacement (in collaboration with M. Zanini). Regarding the numerical analysis portion of this article, the ideal MHD stability analysis were a contribution from C. Nührenberg. The Alfvén and sound wave continuum numerical analysis were provided by A. Könies in collaboration with M. Borchardt. The mode stability analysis implementing EUTERPE were conducted by J. F. Guerrero Arnaiz in collaboration with A. Zocco, M. Borchardt and A. Könies. Further gyrokinetic simulations employing EUTERPE for the investigation of zonal flows were delivered by A. Könies. The discussion of the numerical results was a close collaboration between J. F. Guerrero Arnaiz and the aforementioned co-authors that contributed in this section, including key dialogues with R. Kleiber and A. Mishchenko. The final editing involved all the co-authors listed.

Confirmed by supervisor,
Greifswald, 31.07.2023

PD. Dr. habil. Andreas Dinklage

Confirmed by doctoral candidate,
Greifswald, 31.07.2023

Juan Fernando Guerrero Arnaiz

A.1 Article I

Flux surface identification by spatio-temporal coupling with partial mutual information analysis of electron cyclotron emission data

J. F. Guerrero Arnaiz, A. Dinklage, B. Pompe, J. Geiger, M. Hirsch, U. Höfel, N. Marushchenko, Y. Turkin, R. C. Wolf and the W7-X Team

Plasma Physics and Controlled Fusion, Vol. 63.015002 (2021), DOI: 10.1088/1361-6587/abc2e1

Flux surface identification by spatio-temporal coupling with partial mutual information analysis of electron cyclotron emission data

J F Guerrero Arnaiz^{1,2} , A Dinklage^{1,2} , B Pompe², J Geiger¹ , M Hirsch¹ , U Höfel¹ , N Marushchenko¹ , Y Turkin¹, R C Wolf¹  and the W7-X Team

¹ Max-Planck-Institut für Plasmaphysik, Greifswald, Germany

² Universität Greifswald, Institut für Physik, Greifswald, Germany

E-mail: juan.fernando.guerrero.arnaiz@ipp.mpg.de

Received 6 August 2020, revised 9 October 2020

Accepted for publication 20 October 2020

Published 10 November 2020



CrossMark

Abstract

Fluctuations of electron cyclotron emission (ECE) signals are analyzed for differently heated Wendelstein 7-X plasmas. The fluctuations appear to travel predominantly on flux surfaces and are used as ‘tracers’ in multivariate time series. Different statistical techniques are assessed to reveal the coupling and information entropy-based coupling analysis are conducted. All these techniques provide evidence that the fluctuation analysis allows one to check the consistency of magneto-hydrodynamic (MHD) equilibrium calculations. Expanding the suite of techniques applied in fusion data analysis, partial mutual information (PMI) analysis is introduced. PMI generalizes traditional partial correlation (Frenzel and Pompe *Phys. Rev. Lett.* **99** 204101) and also Schreiber’s transfer entropy (Schreiber 2000 *Phys. Rev. Lett.* **85** 461). The main additional capability of PMI is to allow one to discount for specific spurious data. Since PMI analysis allows one to study the effect of common drivers, the influence of the electron cyclotron resonance heating on the mutual dependencies of simultaneous ECE measurements was assessed. Additionally, MHD mode activity was found to be coupled in a limited volume in the plasma core for different plasmas. The study reveals an experimental test for equilibrium calculations and ECE radiation transport.

Keywords: partial mutual information, electron cyclotron emission, magneto-hydrodynamic equilibrium, correlation analysis, stellarator, Wendelstein 7-X

(Some figures may appear in colour only in the online journal)

1. Introduction

Wendelstein 7-X (W7-X) is an *optimized*, superconducting stellarator [1–3]. The main goal of W7-X is demonstrating

optimized stellarators to be an economic option for a fusion power plant. The notion of *optimization* in the context of stellarator research refers to the intentional shaping of the magnetic field. To this end, 3D shaped coils generate toroidal flux surfaces to meet with seven physical *optimization criteria* [4]. The optimization criteria of W7-X address potential show-stoppers of classical stellarators, namely to reduce particle and energy losses of both the thermal plasma and fast (fusion-born-like) particles as well as stability to achieve magneto-hydrodynamic (MHD) equilibrium at high plasma beta and (reactor-like) low collisionalities. Thus, the magnetic



Original Content from this work may be used under the terms of the [Creative Commons Attribution 4.0 licence](https://creativecommons.org/licenses/by/4.0/). Any further distribution of this work must maintain attribution to the author(s) and the title of the work, journal citation and DOI.

equilibrium is one key to enjoy the benefits of the magnetic field optimization.

The experimental demonstration of *optimized* magnetic field geometry motivates strong interest in techniques that validate precalculated equilibria. The vacuum field has been demonstrated to meet with high accuracy requirements [5] and delivers—as one of the key benefits of stellarator fields—even at vanishing plasma beta confinement by nested flux surfaces. Since W7-X is equipped with superconducting coils, the field can be maintained at quasi steady-state (limited by the infrastructure up to 30 min). Ultimately, insight into the magnetic field geometry with plasma (at finite beta values) provides a next-step validation of field optimization. A specific question addressed in this paper provides indications for flux surfaces. Our technique traces plasma fluctuations simultaneously observed in electron cyclotron emission (ECE) emissivity time series on the inboard and outboard side of W7-X plasmas. The partial mutual information (PMI) technique benefits from the increase of significance levels and from capabilities to suppress spurious nonphysical signal contributions. PMI provides measures estimating how much two time series are related. The method has been developed from information theory [6] and we will show that it offers approaches to address shortcomings from traditional statistical time series analysis.

Conditional mutual information (PMI resp. transfer entropy (TE)) have been applied in very different fields. Examples are in medicine [7] (multichannel electroencephalographic recordings) and climatology (air-temperature anomalies at sea surface toward the upper troposphere) [8]. This paper, however, reports the first application of PMI in fusion data analysis extending early applications of TE [9]. To supplement MHD equilibrium reconstructions, the results are compared to independent flux surface mapping of the electron cyclotron emissivity. The comparison shows good agreement and delivers—beyond the validation aspect—confirmation of radiative transport. New insights could be retrieved applying concepts from information theory to determine *information entropies*. Differently to specific statistical moments (such as in correlation analyses), the information measures provide an overall measure of how much new data X_0 can be predicted from measurements X_1, X_2, \dots . The complexity of the (chaotic) dynamics in a plasma as well as spurious contributions in the analyzed real-world data gives rise to limitations. In literature, practical limitations have been reported (see e.g. [10, 11]). In fusion, tools from information theory for coupling analysis were applied to high-sampled high temperature plasma data. Examples use Schreiber's TE [12]. Specific applications are the successful and fast detection of edge-localized modes [13]. A different example links coupling analysis to heat transport [9, 14, 15]. Limitations both in sensitivity and time-resolution, however, are to be expected in any technique. Clear limitations arise from instruments due to cross-talk, ambient noise (*smog*) and noise in highly sensitive detectors. That is, for real-world plasma data, co-information from sources beyond the measured data and dynamical noise affect the measurements. Thus, clearing coupling analysis from spurious dues is key to critically assess the causality reflected from spatio-temporal signals.

The TE technique makes an important step to address the aforementioned shortcomings. Assuming that an additional time series Y picks up spurious effects as well as the reference time series X , TE discounts for those spurious signal contributions that both time series experience. TE thus delivers additional information not contained as 'underlying' spurious contribution and thereby significantly increases the significance of coupling measures between X and Y . The technique in this paper significantly extends TE by discounting additional signals: if sources of spurious contributions can be identified (e.g. in this paper it is the effect of electron cyclotron resonance heating (ECRH) on ECE measurements), a common driver or noise source in X and Y can be specifically discounted for. This results in an additional increase of significance levels which is shown to be prerequisite for the validation technique in this paper.

The paper is structured as follows: first, in order to assess how much different formulations of information entropies provide new insights, we briefly revise the background of PMI. Next, the description of the instrument (multi-channel ECE radiometer) focuses on the later application for the identification of flux surfaces. Then, the experimental technique is described to introduce the analysis approach. Afterwards, the results from the analysis of multivariate time series from discharges in W7-X provide the central part of this paper. Finally, conclusions will be drawn along a discussion of the different approaches, section 4.

2. Measuring coupling in multivariate time series

The concepts of information flow and transport appear to be closely related. Self-reproducing, open thermodynamical system fed by matter and energy may maximize a process quantity termed *entropy* [16], which is related to the number of states that the system can adopt and, therefore, to the amount of *information* that can be stored or transmitted by it [17]. Heat transport carried by turbulent plasma flows obeys the second principle and the entropy production rate defines the causality of turbulent flows [18]. Both views reflect entropy to be the directing entity for the causality of processes, thus suggesting that an estimate of information flows from experimental data could deliver insight into transport processes. This paper addresses the extent to which different techniques may be employed in order to conduct such measurements. Here, we will apply linear correlation, mutual information (MI) and PMI analysis on time series retrieved through a heterodyne multichannel electron cyclotron radiometer. The latter methods rely on Shannon's information theory [19] and their outcome is considered to estimate the coupling in terms of common (mutual) information of different observables. In general, we would expect that the sum of the thermodynamic entropies of two systems is strictly less than the thermodynamic entropy of the joint system, if there are statistical dependencies between the observables.

An indicator of the strength of the linear association between two variables or time series is given by the Pearson product-moment correlation (PPMC) [20], for which a line of best fit is drawn across the data such that the agreement

between the fit and the data can be expressed as a coefficient r . Correlation coefficient $|r| = 1$ means that there is a deterministic linear relation between the time series, i.e. $y_t = a + bx_t$ with some fixed real values a and b . More precisely,

$$r = \pm 1 \quad \Leftrightarrow \quad \frac{y_t - \bar{y}}{\sigma_y} = \pm \frac{x_t - \bar{x}}{\sigma_x}$$

holds for each t , with standard deviations σ_x and σ_y and means \bar{x} and \bar{y} of series x and y , respectively. Moreover,

$$\begin{aligned} r = 0 &\Leftrightarrow \text{'}x \text{ and } y \text{ are not correlated (linearly dependent)'} \\ r = 0 &\not\Rightarrow \text{'}x \text{ and } y \text{ are statistically independent'} \\ r = 0 &\Rightarrow \text{'}x \text{ and } y \text{ might be nonlinearly dependent'} \end{aligned}$$

One step further, the linear correlation analysis can be performed as a function of the time displacement between samples by shifting one of them by a number of time steps relative to the other which results in the cross-correlation function.

Since details and mathematical background of the information theoretic methods is found in literature [6, 12], only a pictorial explanation is given here to explain why the PMI is capable to discount for perturbations. MI and PMI are information measures based on the concept of Shannon entropy H of a probability distribution $\{p_j\}$ of a random variable X ,

$$H(X) = - \sum_j p_j \text{ld}(p_j).$$

We use dual logarithm $\text{ld} \equiv \log_2$, hence entropy is measured in *bit* (Binary digit) representing the answers of optimal 'yes-no' questions. H represents an average of $\text{ld}(1/p_j)$ w.r.t. the probability distribution $\{p_j\}$. It is interpreted as the (mean) *a priori uncertainty* on X before measurement, or as the posterior information on X gained due to a measurement.

Consider now another random variable Y with probability distribution $\{q_k\}$. If there are statistical relation between X and Y , a measurement of the latter yields some information on X . Hence, starting with the uncertainty $H(X)$ there remains the uncertainty $H(X|Y)$ on X due to the measurement of Y . Consider now the joint distribution $\{s_{jk}\}$ of the random vector (X, Y) , then the (mean) conditional uncertainty is obtained from the corresponding conditional probabilities $p_{j|k} = s_{jk}/q_k$,

$$\begin{aligned} H(X|Y) &= \sum_k q_k \left(- \sum_j p_{j|k} \text{ld} p_{j|k} \right) \\ &= - \sum_{j,k} s_{jk} (\text{ld} s_{jk} - \text{ld} q_k) \\ &= H(X, Y) - H(Y). \end{aligned}$$

If we subtract from the *a priori* uncertainty $H(X)$ on X the posterior uncertainty on X due to measuring Y , we get the information on X contained in Y ,

$$\begin{aligned} I(X, Y) &= H(X) - H(X|Y) \\ &= H(X) + H(Y) - H(X, Y). \end{aligned}$$

It is called *mutual information* because it is symmetric, $I(X, Y) = I(Y, X)$. In general, $0 \leq I(Y, X) \leq \min\{H(X), H(Y)\}$. We get $I(X, Y) = 0$ if and only if X and Y are statistically independent, i.e. iff $s_{jk} = p_j q_k$ for all j, k . If $I(Y, X) = H(X)$ then X is a function of Y . We note that there are also other quantities measuring or detecting dependencies like contingency, however, entropy measures have a more profound interpretation in coding theory.

PMI extends MI, allowing one to discount for a third random variable Z . For that purpose, we consider the random vector (X, Y, Z) with joint distribution $\{s_{jkl}\}$. PMI is defined as

$$I(X, Y|Z) \equiv I(X, (Y, Z)) - I(X, Z).$$

It can be rewritten as,

$$\begin{aligned} I(X, Y|Z) &= H(X|Z) - H(X|(Y, Z)) \\ &= H(X, Y) + H(Y, Z) - H(Z) - H(X, Y, Z) \\ &= \sum_{jkl} s_{jkl} \text{ld} \frac{s_{jkl} \cdot s_{\bullet\bullet l}}{s_{j\bullet l} \cdot s_{\bullet kl}}. \end{aligned}$$

Here we use the marginal distributions $s_{\bullet\bullet l} \equiv \sum_{jk} s_{jkl}$, $s_{j\bullet l} \equiv \sum_k s_{jkl}$, and $s_{\bullet kl} \equiv \sum_j s_{jkl}$. Note that PMI is symmetric w.r.t. an exchange of X and Y $I(X, Y|Z) \neq I(Y, X|Z)$ as well,

$$I(X, Y|Z) = I(Y, X|Z).$$

Conditioning the MI of X and Y on Z , makes PMI analysis a tool to investigate causalities, since the effect of common drivers Z on two apparently coupled time series can be measured. Somewhat differently worded, PMI measures what one random variables Y tells us about another one X (in terms of MI) without the information from a third random variable Z . For our application, we use the estimator proposed in [6] based on a k th-nearest-neighbor algorithm.

The TE $T_{Y \rightarrow X}$ introduced by Schreiber [12] estimates common information of two time series $\{X_n\}$ and $\{Y_n\}$ (the latter shifted by a delay) conditional on time shifted measurements of the time series under consideration $\{X_n\}$:

$$T_{Y \rightarrow X} = I(X_{n+1}, Y_{n-k} | X_{n-k}).$$

In other words, $T_{Y \rightarrow X}$ measures the information in Y_{n-k} on X_{n+1} that is not in X_{n-k} .

3. Multivariate ECE measurements on W7-X for the detection of flux surfaces

Figure 1 shows aspects of the magnetic field geometry of W7-X. The field is mainly generated by 50 nonplanar and 10 planar coils of seven different types (not shown in figure 1). Each type can be charged separately allowing one to change the field topology. The mean major radius of the torus is $R = 5.5$ m. With an aspect ratio of about ten, a typical plasma volume of about 30 m^3 is generated.

A view from the top (figure 1(a)) shows the five-fold symmetry of W7-X. The field strength (mod B) is seen to vary on the flux surfaces giving rise to field ripples. Particles traveling along the field lines therefore experience different magnetic

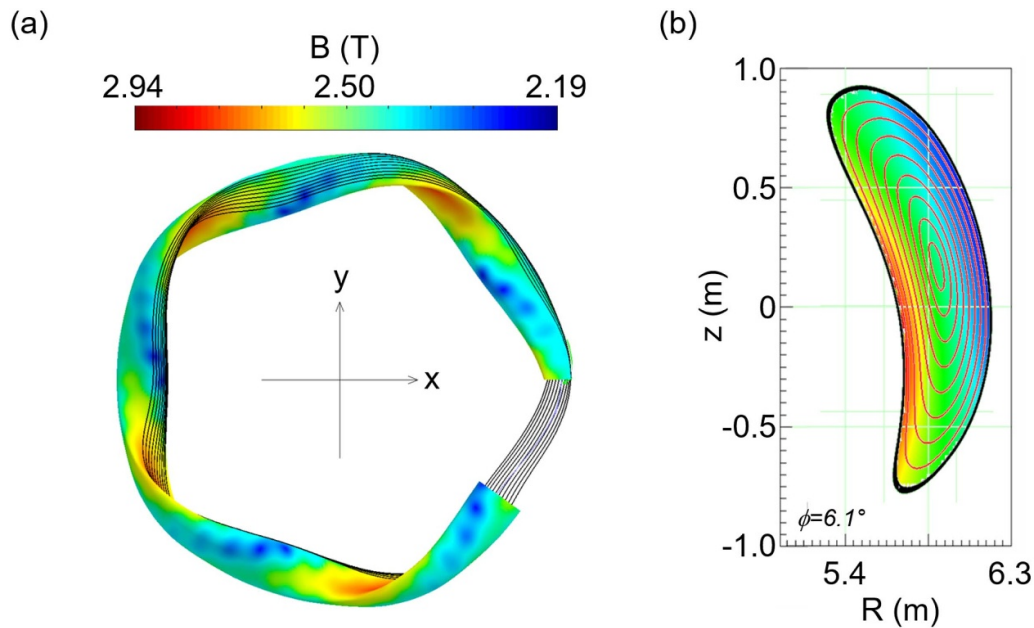


Figure 1. (a) Shows a 3D view on the last closed flux surface of the W7-X standard island-divertor configuration (no islands shown) the open section provides the magnetic axis. The color corresponds to mod B and the black lines indicate a field line. (b) shows a poloidal cross section in the toroidal plane of ECE radiometer measurements. The background color show mod B behind a representative set of flux surface cross sections. Figures are produced with mcviewer based on MConf library, see [21].

mirrors giving rise to locally trapped particles. The pentagonal shape of the torus has high fields on the inboard side in regions of highest curvatures (‘corners’). In the straight sections, there is less field variation along the major radius R . With this background, W7-X is said to have a linked-mirror configuration. The field structure forces trapped particles (in the long mean free path) to precess poloidally in the straight sections and to be reflected from the high field regions at high curvature. It is the precession of deeply trapped particles in the straight sections that diminishes convective losses by grad-B and curvature drifts. Since those losses are much smaller than in classical stellarators, W7-X is *drift optimized*.

Dependent on the magnetic configuration (that can be changed), one finds poloidal cross sections with large variations of mod B. Figure 1(b) shows the cross section observed by the ECE radiometer allowing lines of sight with large variation of mod B and thereby the gyrofrequency. Figure 1(b) also indicates flux surfaces which are considered to be surfaces of constant pressure in ideal MHD. It is directly seen that mod B is different for inboard and outboard sides of an individual flux surface. Any fluctuation of the electron pressure will be quickly leveled off on the flux surface. Thus, coupling analysis of fluctuating plasma parameters are expected to be capable of identifying the flux surface position in the opposite field side of a spatial plasma parameter measurement such as the electron temperature T_e .

3.1. ECE radiometer at W7-X

Electron cyclotron emission radiometry is well established on stellarators [22]. The intensity of ECE due to the gyromotion of the electrons provides a measure for T_e . If ECE is

measured with radiometers (delivering intensities in finite frequency windows), spatio-temporally resolved electron temperatures can be inferred. Since ECE radiometers provide highly sampled signals, they enable beyond the derivation of electron (radiation) temperature profiles also the detection and analysis of temperature perturbations. However, fluctuations of the measured signals do not necessarily imply perturbations in plasma temperature, but may be due to, e.g. system noise.

The ECE diagnostic on W7-X measures in the microwave range with a 32-channel heterodyne radiometer [22–24]. The principal set-up is shown in figure 2. The instrument measures continuously the second harmonic X-mode emission between 124 and 162 GHz at 2.5 T, allowing one to derive T_e profiles. For each ECE channel, the detected microwave intensity is absolutely calibrated by comparison with the emission of a blackbody source. The calibration measurement consists of the detection of radiation from surfaces at two well-defined temperatures (room temperature and boiling temperature of liquid nitrogen). The radiation collected by an observation optics is received by a microwave horn antenna and led by waveguides to the receiver system outside the torus hall. The radiation has to pass through a notch filter, required to suppress spurious microwave radiation from high power electron cyclotron heating. Here, the gyrotrons emit frequencies matching with the second harmonic gyrofrequency at the plasma center at the toroidal position of heating (≈ 140 GHz). The ECE channels are enumerated from #1–32, where the higher the enumeration, the higher the frequency at which the measurements are performed. For the subsequent discussion, the ECE channel #16, which detects the ECE at ≈ 139 GHz, is at the edge of the notch filter characteristic and will be referred to as the *heating*

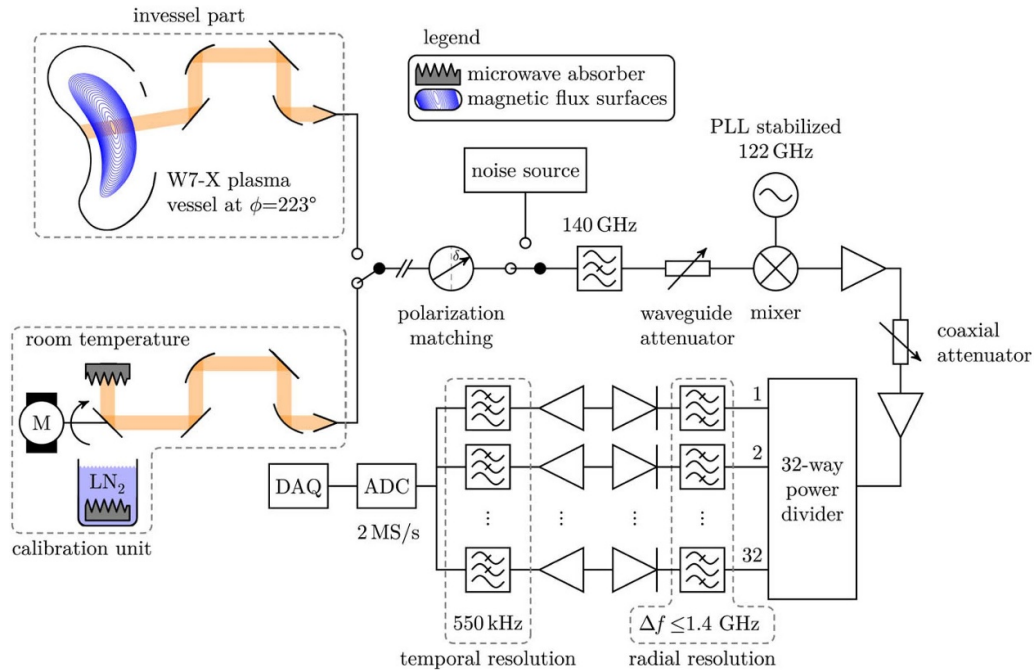


Figure 2. Signal path of the multichannel broadband heterodyne radiometer at W7-X: from plasma and calibration source to DAQ. Adapted from [23].

channel. ECE channels #1 – 15 measure the low-field side and channels #17 – 32 the high-field side. The microwaves are detected and down-converted to lower frequencies (4 – 40 GHz) via a stabilized local oscillator at 122 GHz. Then, the down converted signals are split into 32 channels and bandpass filtered with bandwidths of $0.25 \text{ GHz} \leq \Delta f \leq 1.4 \text{ GHz}$. After predetection amplifiers, detection diodes and a low-pass filter to avoid aliasing, a 16 bit analog-to-digital converter with a sampling frequency of up to 2 MHz converts the intensities into sampled time series. Finally, the fast sampled digital signals arrive in the data acquisition system (DAQ), resulting in a diagnostic with spatial and temporal resolutions of the order of 1 cm and $10 \mu\text{s}$ [25]. The details of the set-up are relevant to assess measurement noise and common drifts that may affect groups or individual of channels of the radiometer.

According to the previous discussion, a spatial profile of T_e can be derived from calibrated spectral intensities and the assignment of frequencies to mod B. The latter assignment is made by calculating the field with a 3D MHD equilibrium code (VMEC (variational moments equilibrium code) [26]) that solves the force balance of ideal MHD under the assumption of the existence of flux surfaces. This approach is employing the cold resonance of ECE, assuming that the measured intensity is emitted from the location where the probed frequency corresponds directly to the cyclotron frequency. The cold resonance model is valid for a single emitting electron only. Radiation transport in a plasma including reabsorption and emission by electrons must be taken into account to explain the finite optical thickness and hence the layer where the measured radiation stems from. For conditions in the plasma core, this optical thickness is sufficient to be treated as blackbody radiation from a finite layer right at somewhat higher field than that of the cold resonance location. The code TRAVIS

(TRAcing VISualized) [21] solves the radiative transport and the radiative transfer equations using the 3D magnetic equilibrium and 3D ray-tracing. The correction of radiative transport results in spatio-temporal radiation temperature measurements and profiles as shown later in figures 3 and 4 respectively.

3.2. ECE time series from W7-X and coupling analysis

Figure 3(a) shows waveforms analyzed in this paper. The discharge (20160309.22) was conducted in the first experimental campaign of W7-X which allowed (due to unprotected walls) small heating energies only. The plasma was heated by electron cyclotron heating and the power (figure 3(a) red line) was applied for one second at different heating power levels for 300 ms each (after a 100 ms start-up phase), resulting in time periods with a ‘high’ heating power of 2 MW, ‘mid’ power of 1.3 MW and ‘low’ of 0.6 MW. Within the achievable density in the respective plasma campaign, the plasma density was relatively low ($< 1.2 \times 10^{19} \text{ m}^{-3}$). These conditions reveal so called core electron-root confinement, a confinement regime typically exhibiting regions of large positive radial electric fields in the core. The reason lies in (parameter dependent) non-intrinsically ambipolar electron and ion fluxes (in stellarators) [27]. With its large spatial T_e variations, the chosen discharge provides a cross section of different plasma regimes relevant to assessments of the optimization criteria in W7-X [28] with large and small prevailing neoclassical electron energy transport. The response in T_e is shown in figure 3(a) as well. Different channels of the radiometer indicate electron temperatures as high as $T_e \sim 6 \dots 8 \text{ keV}$ in the center (channel #12 and #18) and much lower temperature in the periphery of the plasma. The transition of the ECE channel waveform due to changes

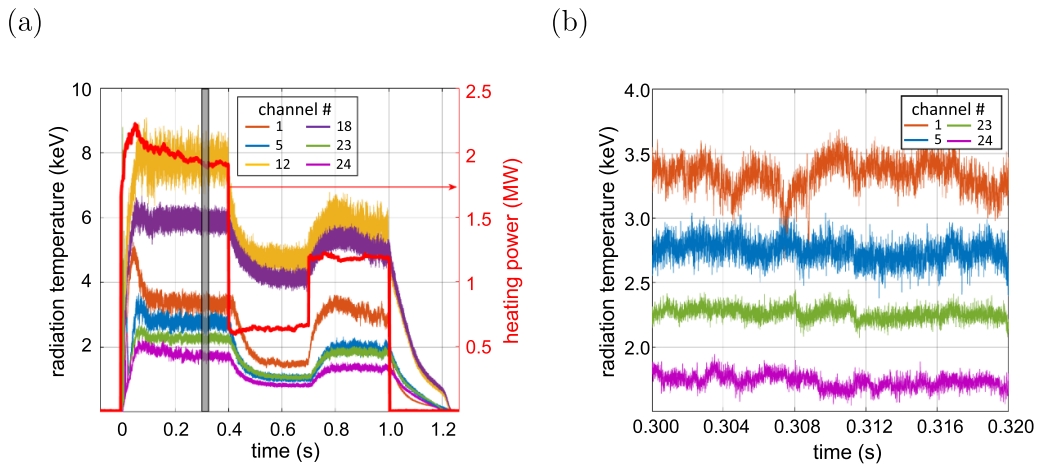


Figure 3. Overview plot of relevant plasma parameters for the flux surface identification. (a) Electron temperature T_e at various radial positions obtained through the ECE diagnostic and the power of the main plasma heating source (red line). The gray shaded area indicates the time interval selected to analyze the ECE time series. This interval is magnified in (b).

of the heating power reflects local changes of the energy confinement.

Figure 3(b) shows a magnification of selected ECE time series from four radiometer channels indicated by the channel number. The ECE time series were chosen in a stationary time window from $t = 0.300 \dots 0.320$ s. Visual inspection reveals apparent similarities in the time series. E.g. a pulse-like structure is found both in channels #23 and #5 at around 0.317 s. It is noted, however, that many of the excursions beyond the apparent noise level are difficult to identify in other channels. All signals show noise levels which may vary from channel to channel. This simple observation already indicates that the observed fluctuations of the signals may result partly from the instrument. Dynamical noise (from the plasma), however, is not excluded and it will be shown later that this part of the signal contains ‘tracer fluctuations’ that appear to be detectable by the information entropies. This ambiguity is sought to be addressed by the PMI analysis below. In order to estimate the statistical significance of the information measures, the coupling between one random noise signal of the same duration as the ECE time series and other hundred equally generated signals are analyzed through the MI, PMI and TE methods. This results in a significance threshold level of 8×10^{-3} bit.

The set-up of the ECE indicated ECE channels close to the heating frequencies to be affected by large spurious ‘stray-radiation’. Given the capabilities of PMI to discern the information of a third source from the MI of two others, PMI analysis will be applied in this case to discount the information coming from an ECE channel that is heavily directly influenced by the plasma heating source. In the remainder we present analyses for the quasi-stationary signals in the ‘high’ power region.

Since we address spatial coupling revealed by the radiometer channels, we need to address where the detected emissivity in each channel is born. With lines of sight measured in real space geometry and measurements of the coil positions, coordinate transforms are conducted to assign positions to flux surfaces. While a first approximation of the

emissivity position is given by the electron cyclotron resonance frequency, resonance broadening and radiation transport is considered in the ray-tracing calculations with the code TRAVIS. The broadening is mainly relativistic since the line of sight of the radiometer is almost perpendicular to the guiding center and, therefore, Doppler broadening is negligible. The radiation transport needs to be considered since the assumption of equal emission and absorption (blackbody) is gradually violated as the plasma becomes optically gray (at lower temperatures). The bar in the abscissa in figure 4 indicates the dominating regions (spatial width) the emissivity is emerging from (5%–95% interval). These regions are asymmetric in the low-field side near the edge (where the optical depth is low) due to a relatively large amount of radiation coming from the plasma core, but less from the edges themselves. This asymmetry is also observed in the high-field side and is in the same direction given the sign change of the T_e gradient. Since the radiation transport depends on densities and temperatures, the TRAVIS calculation refers to the time interval of the coupling investigation.

The contributions to the ECE mostly come from waves with a polarization perpendicular to the background magnetic field given by the oscillating E-field (X-mode), thus the radial position of the measurements to be considered for the following coupling analysis will be those from the X-mode. Negative values of the effective plasma radius ρ (defined as $\rho = \frac{r}{a}$, where $\frac{r}{a}$ is the normalized minor radius of the plasma) represent radial regions near the high-field side positions with respect to the axis. The channel with the lowest frequency covers the plasma center as indicated by the spatial width of emission line, thus the measurements from this ECE channel are expected to show strong couplings with measurements originating from the plasma center. This is due to the relativistic downshift of the ECE from hot electrons in the plasma center which at the plasma edge (low density and low T_e) is not well reabsorbed. This effect also compromises the measurements from ECE channel #2 but at a shorter extent. Because of this, the measurements from these channels

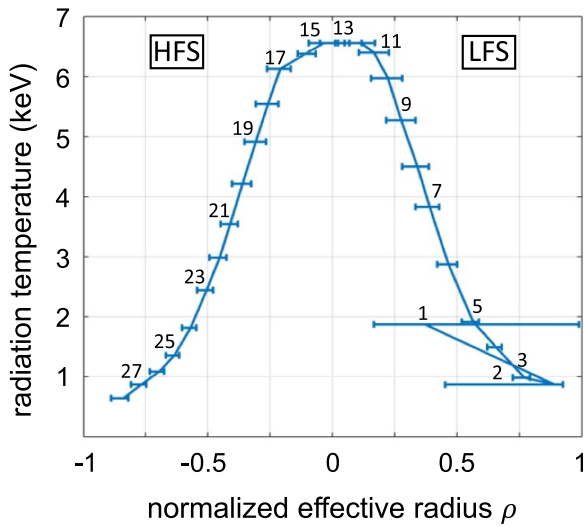


Figure 4. Radiation temperature profile calculated through the ray-tracing code TRAVIS from electron cyclotron emission measurements in W7-X plasma discharge 20160309.22 from $t = 0.30$ s to $t = 0.32$ s for the X-mode. Positive values of ρ represent radial regions near the low-field side (LFS) and negative, near the high-field side (HFS).

cannot be interpreted as localized temperature measurement. Thus, the radial positions of this channel will be obtained from the cold resonance, that is, neglecting kinetic effects such as relativistic.

Now, the coupling of one selected channel (#5 at about $\rho = 0.55$ in figure 4) is examined. Figure 5(a) shows the absolute value of the linear correlation (PPMC—solid gray lines), MI (broken red lines), PMI (solid red lines) and TE (dotted red lines) results. The instantaneous coupling with each individual channel is displayed as indicated in the title text of the figure. The channels are allocated spatially according to the normalized effective radius as shown in figure 4. The blue shaded areas represent the region where the radiation measured through channel #5 comes from and its mirrored location on the opposite field side.

Clear peak structures are identified in all coupling calculations. Moreover, indications for couplings are seen in adjacent channels to #5 as well. The most prominent peak, however, is found in the opposite field side at channel #23, close to the mirrored effective radius location of channel #5 but shifted to the low-field side. Also, the radial region covered by channel #23 (red shaded area) overlaps with the mirrored location of the reference channel. At this point, one may conclude that the flux surface is identified within the resolution of the coupling analysis. The broad peak structure around channel #23 indicates radial couplings with neighboring channels. This is, not sharply pinpointing one specific channel, but rather a radial location with a specific width (as seen from the radial overlaps seen in figure 4). A more detailed inspection shows that besides identifying a coupling structure near the suggested position of the flux surface, linear correlation indicates couplings with the channels in the low-field side closest to the ECE

horn antenna, adjacent channels and other channels sensitive also to radiation coming from the plasma center.

For the analysis of linear dependencies, only the linear correlation is implemented given that the fluctuations through these surfaces are quickly enough leveled off, for a synchronous analysis to be representative. It is noted that the linear correlation indicates coupling with channels in the core but also even further out the dominant peak ($\rho \sim -0.75$). The linear correlation is now compared to the MI which takes also non-linear dependencies into account. The comparison with noise levels provides the ‘detection’ limit as shown by the gray shaded area in figure 5(a). The MI indicates coupling structures similar to the linear correlation but exhibit differences to the linear correlation as well. Considering the significance threshold, some couplings suggested by the linear correlation are not significant in the MI analysis.

Next, we study the MI discounted from information in other channels. The PMI was calculated systematically discounting for all other ECE channels. The largest impact was found if channel #16 (the heating channel) was discounted for. The PMI (conditional on the signal from channel #16) shows one prominent coupling peak above the significance level on the $\rho < 0$ part of the profile. Moreover, spatial coupling structures are quite narrow compared to the linear correlation and less coupling indications above the significance threshold are found compared to the linear correlation and MI. Additional coupling indications for more outside lying channels (#1, #2) for negative ρ agree with the outcome of the radiation transport calculations (as indicated by the overlap of spatial widths of emission lines shown in figure 4). This is, through neglecting the characteristics contained in the signal measured from the heating channel that seem to influence the pairwise couplings.

Comparing the results from the PMI analysis with the TE $T_{\#5 \rightarrow \#X}$ ($k = 1$, cf section 2) analysis, results in a similar coupling structure near the expected flux surface location. In the TE analysis, the peak structure is narrower and as low in amplitude as the detection limit.

Performing the same coupling analysis for ECE channel #23 as the reference (figure 5(b)) results in similar results. The individual peaks of the coupling structure in the opposite field side of the reference channel lies for all methods at the same radial location. This finding is providing evidence that the ECE line of sight transverses the flux surface twice (see also figure 6). Taking the width of the peaks, a comparison with ECE profiles from ray-tracing (with TRAVIS using a VMEC equilibrium), indicates that the position of the flux surface is consistently detected. A small radial shift of the peak maximum, however, occurs systematically toward the high-field side. The shift is about 1 GHz (corresponds to one channel number, cf section 3.1) and coincides with the asymmetric (high-field side shift) broadening of the ECE emission layer by hot electrons. The typical scale of the shift $\frac{\Delta\nu}{\nu} \sim \frac{T_e}{m_e c^2}$ [29] corresponds to our observations.

Between the synchronous nondirected coupling analysis methods (PPMC, MI and PMI analysis), the clearest indication for flux surface coupling is found in PMI calculations conditional on the signal from the heating channel. This finding is

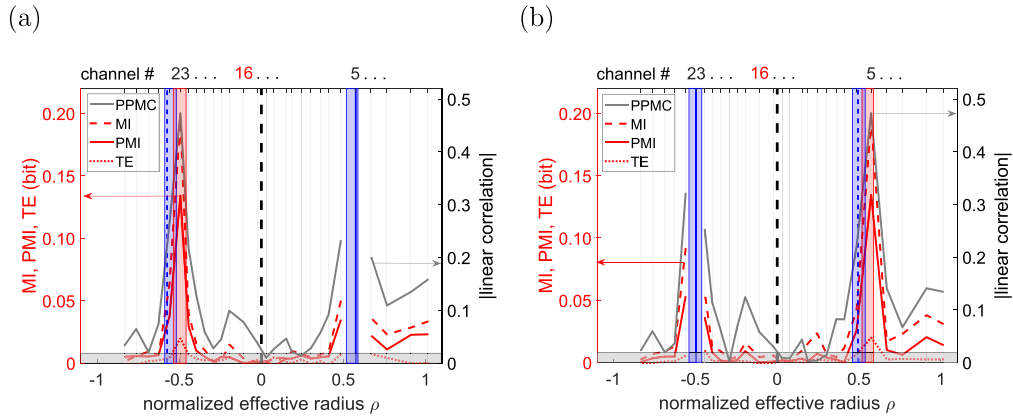


Figure 5. (a) Absolute value of the Pearson product-moment correlation (PPMC), mutual information (MI), partial mutual information (PMI) and transfer entropy (TE) $T_{\#5 \rightarrow \#X}$ of the ECE radiometer channel #5 with all others for ECE signal in W7-X plasma discharge 20160309.22 from $t = 0.30$ s to $t = 0.32$ s. Channel #16 is discounted in the PMI analysis and the sample shift for the TE analysis is $k = 1$. The blue solid line indicates the radial position of the reference channel and the blue dashed line illustrates the equivalent position in the opposite field side of channel #5. The blue shaded areas indicate the radial region covered from ECE channel #5 and its mirrored location. The gray shaded area reflects the significance threshold for the information quantities. The red shaded area indicates the location from channel #23. (b) Identical analysis for channel #23 as the reference.

interpreted to reflect the impact of spurious signals correlated with a central channel affected by the ECRH.

In a next step, the PMI coupling analysis method is extended to more ECE channels as the reference (#4, #5 and #6), which results in similar outcomes (figure 6). For a better visualization of the physical significance of the results, figure 6(a) shows a poloidal cross section of W7-X with a Poincaré plot depicting the line of sight of the ECE diagnostic crossing the plasma center, as well as the locations of the three ECE reference channels and the flux surfaces connecting these to their respective locations in the opposite field side. The results of the PMI analysis discounting again, the influence of the heating channel on the mutual dependencies between the reference channel and all others, are shown in figure 6(b). Similar to the results shown in figure 5(a), couplings with adjacent ECE channels appear, as well as peak structures near the respective flux surface position in the opposite magnetic field side indicated by TRAVIS.

As the reference channel moves inwards, closer to the plasma center, so do the PMI coupling structures. Couplings between reference channels #4–5 and the two outermost channels can be seen. This can be retraced from the spatial widths of emission lines in the temperature profile (figure 4) due to relativistically downshifted emission from hot core electrons. However, even when PMI analysis offers the most robust results out of the other methods, not yet fully understood couplings with channels measuring radiation from the high temperature gradient (#8–11) are observed. Nevertheless, the spatio-temporal coupling analysis of ECE data for these three ECE signal channels as the references identify the position of the respective flux surfaces in the opposite field side. However, the shift of the coupling structure to the low-field side observed from figure 5 prevails.

Besides the results during the ‘high’ power phase ($t = 0.30$ s), coupling analysis during the ‘low’ and ‘medium’ power phases were also carried out confirming the reported

results from the high-power phase. With increasing heating power the coupling strengths also increase, the identifiable flux surfaces lie closer to the plasma edge, the mismatch between the calculated positions of the flux surfaces and the ones suggested by the coupling analysis increases, and more in number coupling structures appear across all coupling analysis methods. Throughout the three different power phases during this plasma discharge, the determination of the position of the flux surface in the opposite field side of a reference channel was possible.

A different case to reveal the capabilities of the PMI technique is reflected in figure 7. Here, we show the MI (no discounting), the PMI (discounting system noise) and the PMI discounting for an ECE channel adjacent to the chosen reference (channel #9 indicated by the black dotted line and discounted channel #10 red dotted line, respectively). A Fourier analysis of the scrutinized channels indicates typical frequencies of about 4 KHz allowing one to classify the observed fluctuations as MHD mode activity. The coupling analysis is omitted for ECE channels with low signal-to-noise ratio.

It is clearly seen that the coupling is localized in the core ($|\rho| < 0.5$). The system noise is discounted by conditioning on a time window of the ECE channel after plasma operation (dashed black line in the figure). The small difference of MI (gray) and PMI (black) confirms the coupling to result from plasma effects. Finally, the PMI conditioned on a channel within the MHD-mode activity region indicates significantly lower coupling. We recall that (this specifically conditioned) PMI $I(X_{\text{ref}}, Y_i | X_{i=10})$, indicated by the red dotted line, could be seen as a measure of how much information is left in an ECE channel Y_i to predict time series from the reference channel X_{ref} (if X_{ref} is known). In other words, the red curve reveals how much new information comes from the respective location in addition to channel #10. The large decrease (red vs. gray) indicates a close coupling in channels #9 and #10 (red)

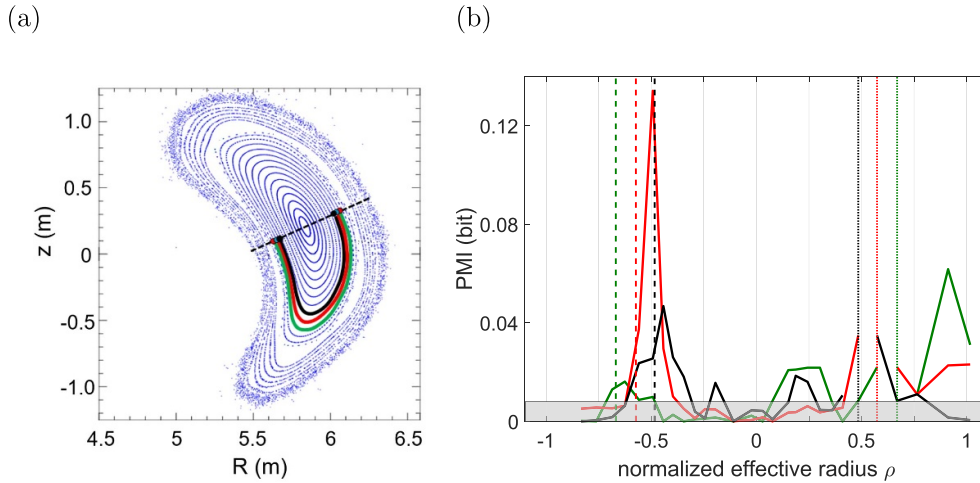


Figure 6. (a) Poloidal cross section with a Poincaré plot of the magnetic configuration implemented in plasma discharge 20160309.22 for a toroidal angle $\phi = 6.1^\circ$ at W7-X. Black dashed line depicts the line of sight of the ECE diagnostic. Green, red and black curves and markers indicate the flux surfaces connecting channels #4, #5 and #6 with their respective locations in the opposing field side. (b) Extended PMI analysis w.r.t. three different reference ECE channels mapped on the normalized effective radius ρ . Channel #16 is discounted in the PMI analysis. The gray shaded area reflects the significance threshold.

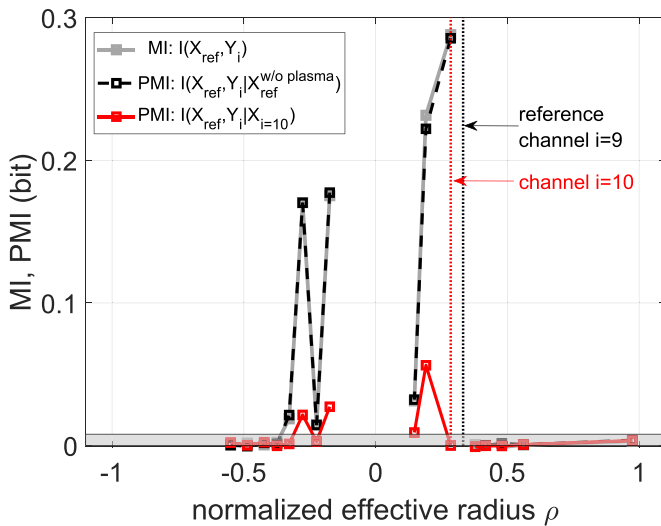


Figure 7. MI and PMI for MHD mode activity identification in the W7-X discharge 20180829.33 from $t = 1.00$ s to $t = 1.01$ s (mean density of $3 \times 10^{19} \text{ m}^{-3}$, heated at 2 MW ECRH power). The coupling analysis of radiometer channel #9 (reference channel, $i = 9$) with all others channels is shown. The abscissa represents the position of the ECE emissivity determined by ray-tracing calculations. The gray shaded area indicates the significance threshold for the information quantities.

due to MHD mode activity. We thus conclude that the coupling involves regions $|\rho| \lesssim 0.3$, and thus has a global character. We note that the observed coupling disappears in the course of the discharge.

4. Discussion and conclusions

All investigated traditional and information-based coupling analysis methods identify coupling of ECE radiometer channels. TE analysis results coincide with the results from the

other methods but appear to be less sensible for the conducted coupling analysis. PMI analysis, with its capability to discount for specific spurious signals (stemming from different noise sources), is able to extract T_e -fluctuations from the background of other fluctuating signal components. As a result, PMI delivers clearer results than linear correlation and MI analysis for the specific data set analyzed in this paper. Detailed assessments of cross-talk effects and common noise sources from amplifiers and detection electronic groups are giving valuable input from structural similarities in the PMI analysis.

While the indication of coupling on flux surfaces is interpreted to be due to fluctuations carried by parallel transport on flux surfaces, the introduced analysis also provides indications for couplings perpendicular to flux surfaces as reported in [9]. The broadening of the coupling structures, moreover, may provide insight into energy and particle transport but is also found to be affected by apparent couplings due to induced noise and radiation transport. Moreover, the impact of the physics of ECE, here the asymmetric broadening due to relativistic mass increase, leads to systematic shifts of the coupling peak to apparently higher magnetic field positions.

All in all, the findings of spatial coupling analysis with PMI of ECE radiometer data confirm the position of the flux surfaces in plasma operation. We conclude that the method confirms (as expected) MHD equilibrium calculations. The experimental approach is simple and robust, since it relies on the coupling analysis method (PMI) of electron cyclotron emissivity fluctuations. The technique was also applied to reveal the spatial coupling and extent of MHD mode activity. The coupling analysis does not depend on the signal level or calibration of the ECE signal. Therefore, and by taking note that ECE is a microwave measurement [30], we expect that the method could be also employed to confirm the existence of flux surfaces in harsh environments.








As an overall conclusion, we find that conditional information coupling analysis may provide indications of physical

processes, e.g. parallel transport or spatial structures of fluctuations. Equally important, the coupling analysis also indicates how much the measurement process is affected by spurious signals. Therefore, through discerning between physically and not physically relevant contributions to the mutual dependencies between synchronous ECE measurements, the introduced method of PMI analysis appears to provide an added value for the analysis of experimental fluctuation data from fusion plasmas.

Acknowledgments

This work has been carried out within the framework of the EUROfusion Consortium and has received funding from the Euratom research and training programme 2014–2018 and 2019–2020 under Grant Agreement No. 633053. The views and opinions expressed herein do not necessarily reflect those of the European Commission.

ORCID iDs

J F Guerrero Arnaiz  <https://orcid.org/0000-0002-7650-2918>
 A Dinklage  <https://orcid.org/0000-0002-5815-8463>
 J Geiger  <https://orcid.org/0000-0003-4268-7480>
 M Hirsch  <https://orcid.org/0000-0002-7120-6087>
 U Höfel  <https://orcid.org/0000-0003-0971-5937>
 N Marushchenko  <https://orcid.org/0000-0002-0415-1303>
 R C Wolf  <https://orcid.org/0000-0002-2606-5289>

References

- [1] Nührenberg J and Zille R 1986 Stable stellarators with medium β and aspect ratio *Phys. Lett. A* **114** 129
- [2] Grieger G, Lotz W and Merkel P *et al* 1992 Physics optimization of stellarators *Phys. Fluids B* **4** 2081
- [3] Wolf R C *et al* 2017 Major results from the first plasma campaign of the Wendelstein 7-X stellarator *Nucl. Fusion* **57** 102020
- [4] Wagner F and Wobig H 2005 Magnetic confinement *Plasma Physics: Confinement, Transport and Collective Effects* eds A Dinklage, T Klinger, G Marx and L Schweikhard (Berlin: Springer) pp 375–97
- [5] Pedersen T *et al* 2015 Plans for the first plasma operation of Wendelstein 7-X *Nucl. Fusion* **55** 126001
- [6] Frenzel S and Pompe B 2007 Partial mutual information for coupling analysis of multivariate time series *Phys. Rev. Lett.* **99** 204101
- [7] Staniek M and Lehnertz K 2008 Symbolic transfer entropy *Phys. Rev. Lett.* **100** 158101
- [8] Runge J, Heitzig J and Marwan N *et al* 2012 Quantifying causal coupling strength: A lag-specific measure for multivariate time series related to transfer entropy *Phys. Rev. E* **86** 061121
- [9] van Milligen B, Höfel U and Nicolau J *et al* 2018 Study of radial heat transport in W7-X using the transfer entropy *Nucl. Fusion* **58** 076002
- [10] James R, Barnett N and Crutchfield J 2015 Information flows? A critique of transfer entropies *Phys. Rev. Lett.* **116** 238701
- [11] Smirnov D A 2013 Spurious causalities with transfer entropy *Phys. Rev. E* **87** 042917
- [12] Schreiber T 2000 Measuring information transfer *Phys. Rev. Lett.* **85** 461
- [13] Murari A, Lungaroni M and Peluso E *et al* 2018 On the use of transfer entropy to investigate the time horizon of causal influences between signals *Entropy* **20** 627
- [14] van Milligen B, Höfel U and Hirsch M *et al* 2017 The impact of heating power on radial heat transport in W7-X *Nucl. Fusion* **57** 056028
- [15] Nicolau J H, Garcia L and Carreras B A *et al* 2018 Applicability of transfer entropy for the calculation of effective diffusivity in heat transport *Phys. Plasma* **25** 102304
- [16] Boltzmann L 1877 Über die beziehung zwischen dem zweiten hauptsatz der mechanischen wärmetheorie und der wahrscheinlichkeitsrechnung resp. den sätzen über das wärmeleichgewicht *Sitzb. Kais. Akad. Wiss. Wien Math. Naturwiss. Cl.* **76** 373
- [17] Marinescu D C and Marinescu G M 2012 Chapter 3 - classical and quantum information theory *Classical and Quantum Information* eds Marinescu D C and Marinescu G M (New York: Academic) pp 221–344
- [18] Garbet X, Dubuit N and Asp E *et al* 2005 Turbulent fluxes and entropy production rate *Phys. Plasmas* **12** 082511
- [19] Shannon C E 1948 A mathematical theory of communication *Bell Syst. Tech. J.* **27** 379
- [20] Ware B M W and Ferron J 2013 Describing the relationship between two quantitative variables: correlation *Introductory Statistics: A Conceptual Approach Using R* (New York: Routledge)
- [21] Marushchenko N, Turkin Y and Maassberg H 2014 Ray-tracing code TRAVIS for ECR heating, EC current drive and ECE diagnostic *Comput. Phys. Commun.* **185** 165
- [22] Hartfuss H J, Geist T and Hirsch M 1997 Heterodyne methods in millimetre wave plasma diagnostics with applications to ECE, interferometry and reflectometry *Plasma Phys. Control. Fusion* **39** 1693
- [23] Höfel U, Hirsch M and Kwak S *et al* 2019 Bayesian modeling of microwave radiometer calibration on the example of the Wendelstein 7-X electron cyclotron emission diagnostic *Rev. Sci. Instrum.* **90** 043502
- [24] Schmuck S, Hartfuss H J and Hirsch M *et al* 2009 Design of the ECE diagnostic at wendelstein 7-X *Fusion Eng. Des.* **84** 1739
- [25] Hirsch M and Höfel U *et al* 2019 ECE diagnostic for the initial operation of Wendelstein 7-X *EPJ Conf.* p 03007
- [26] Hirshman S, van Rij W and Merkel P 1986 Three-dimensional free boundary calculations using a spectral green's function method *Comput. Phys. Commun.* **43** 143
- [27] Yokoyama M *et al* 2007 Core electron-root confinement (CERC) in helical plasmas *Nucl. Fusion* **47** 1213
- [28] Dinklage A, Beidler C and Helander P *et al* 2018 Magnetic configuration effects on the Wendelstein 7-X stellarator *Nat. Phys.* **14** 855
- [29] Hutchinson I H 2002 Chapter 5 *Principles of Plasma Diagnostics* (Cambridge: Cambridge University Press) pp 158–66
- [30] Biel W *et al* 2015 Demo diagnostics and burn control *Fusion Eng. Des.* **96–97** 8

A.2 Article II

Fast characterization of plasma states in W7-X with permutation entropy

J. F. Guerrero Arnaiz, A. Dinklage, J. Geiger, M. Hirsch, U. Höfel, C. Brandt, H. Thomsen, J. Schilling, K. Rahbarnia, U. Neuner, M. Zanini and the W7-X Team

Plasma Physics and Controlled Fusion, Vol. 64.084005 (2022), DOI: 10.1088/1361-6587/ac7a5d

Fast characterization of plasma states in W7-X with permutation entropy

J F Guerrero Arnaiz^{1,2,*} , A Dinklage^{1,2} , J Geiger¹ , M Hirsch¹, U Höfel¹, C Brandt¹ , H Thomsen¹, J Schilling¹ , K Rahbarnia¹ , U Neuner¹, M Zanini¹  and the W7-X Team¹

¹ Max-Planck-Institut für Plasmaphysik, Greifswald, Germany

² Universität Greifswald, Institut für Physik, Greifswald, Germany

E-mail: juan.fernando.guerrero.arnaiz@ipp.mpg.de

Received 28 February 2022, revised 2 June 2022

Accepted for publication 20 June 2022

Published 4 July 2022



CrossMark

Abstract

Detecting changes in plasmas is compulsory for control and the detection of novelties. Moreover, automated novelty detection allows one to investigate large data sets to substantially enhance the efficiency of data mining approaches. To this end we introduce permutation entropy (PE) for the detection of changes in plasmas. PE is an information-theoretic complexity measure based in fluctuation analysis that quantifies the degree of randomness (resp. disorder, unpredictability) of the ordering of time series data. This method is computationally fast and robust against noise, which allows the evaluation of large data sets in an automated procedure. PE is applied on electron cyclotron emission and soft x-ray measurements in different Wendelstein 7-X low-iota configuration plasmas. A spontaneous transition to high core-electron temperature (T_e) was detected, as well as a localized low-coherent intermittent oscillation which ceased when T_e increased in the transition. The results are validated with spectrogram analysis and provide evidence that a complexity measure such as PE is a method to support *in-situ* monitoring of plasma parameters and for novelty detection in plasma data. Moreover, the acceleration in processing time offers implementations of plasma-state-detection that provides results fast enough to induce control actions even during the experiment.

Keywords: permutation, entropy, data-mining, W7-X

(Some figures may appear in colour only in the online journal)

1. Introduction

Wendelstein 7-X (W7-X) is an *optimized*, superconducting stellarator [8, 17, 23] with the main goal of demonstrating that stellarators are capable of plasma steady-state operation at fusion-relevant plasma conditions. The optimization was performed according to different reactor relevant criteria, e.g.

minimizing losses due to neoclassical transport and maximizing the confinement of fast particles in the plasma center, while maintaining good magneto-hydrodynamic (MHD) stability at finite β equilibria. Regardless of the complexity and challenges that are faced in stellarator research, these devices are promising for reactor purposes since the magnetic field topology is formed only by external coils, which means that the plasma can thus be sustained continuously.

To ensure steady-state operation, it is necessary to detect, understand and react accordingly to plasma state changes that could compromise the plasma confinement. For this, novelty/anomaly detection methods based on neural networks are currently implemented e.g. for the detection of magnetic instabilities caused by Alfvén eigenmodes [20] and for the detection of disruption precursors in tokamaks [7]. However,

* Author to whom any correspondence should be addressed.



Original Content from this work may be used under the terms of the [Creative Commons Attribution 4.0 licence](https://creativecommons.org/licenses/by/4.0/). Any further distribution of this work must maintain attribution to the author(s) and the title of the work, journal citation and DOI.

these methods can be computationally expensive and may require large data sets to operate appropriately. Here, we propose an extremely fast and robust detector based on permutation entropy (PE) for *in-situ* detection of transient events, as well as for offline bulk data analysis. To study the spatio-temporal evolution of the plasma and demonstrate the feasibility and benefits of the PE analysis, we implemented it on highly sampled T_e and soft x-ray (SXR) data.

2. Measuring predictability in multivariate time series

Measuring predictability of time series allows a better understanding of the characteristics and properties of any underlying stochastic processes and the characteristics of dynamical systems. Time series can be regarded to be more or less ordered. A generic task of time series analysis is to predict a value from measurements, that is e.g. calculating the probability to measure a value x_t given measurements $\{\dots, x_{t-2\tau}, x_{t-\tau}\}$ preceding x_t or to unravel characteristic invariants of the time series. Entropy has been shown to be one of the most powerful quantities to evaluate the degree of randomness and predictability of a signal. However, with continuous data, the entropy of a time series can only be calculated to provide an estimation. The accuracy of which is bound to the advantages and drawbacks of the method implemented [6]. Various estimators have been developed, one of these being the PE which is a statistical measure that takes all statistical dependencies into account to describe the degree of randomness in a data set. PE was firstly introduced in [1] and has been successfully implemented in different science branches e.g. medical sciences [12, 13, 18] and financial economics [10, 24, 25], including plasma physics, e.g. for unraveling the chaotic nature of L-mode edge plasma density fluctuation dynamics [14] and characterizing low-aspect-ratio reversed-field pinch plasma through the identification of stochastic and chaotic regions [19]. In this paper, we apply PE on non-stationary data to characterize plasma states and their evolution. In particular, PE is employed as a method for time series analysis and the method is computationally effective to allow one for fast even real-time characterization.

In a sense, PE estimates the degree of randomness of a signal. The salient feature of PE is to identify ordinal patterns of m -tuples separated by a delay time τ_D [1, 2]. For a PE of order m , m measurements are analyzed at a time forming a *time comb* to determine the ordering of consecutive measurements. To do so, distinct measurements are assigned a *rank* or a *symbol* depending on their relative ordinal arrangement such that the order pattern π of the m -tuple can be identified. As an example, for the order $m = 3$ one could arrange three (different) values into $3!$ different patterns π . In practice, PE is determined by counting the number of occurrences of each π and the calculating the Shannon information H_m of the probability distribution p_π :

$$H_m = - \sum_{\pi} p_{\pi} \log p_{\pi}. \quad (1)$$

The Shannon information varies within $0 \leq H_m \leq \log_2 m!$. $H_m = 0$ is attained for either a monotonously increasing or decreasing time series. For completely random time series (independent and identically distributed processes, *i.i.d.*) each permutation has probability $(m!)^{-1}$ leading to $H_m = \log_2 m!$. However, if there is some structure in the data, the permutations are not uniformly distributed $H_m < \log_2 m!$. And the more irregular the time series is, the closer is $H_m/\log_2 m!$ to one. For experimental data, an ordinal technique such as PE is less affected by noise and data outliers.

For a numerical implementation, PE is based on sorting algorithms rather than distance calculations which are way faster to compute. The main determinant of the computing speed of the PE is the permutation order m given that the sorting algorithm has to assign an order pattern to each m -tuple from $m!$ distinct possible patterns. The choice of m is a trade-off between details in ordering pattern and computational costs: while low m lead to very small computation times, a low permutation order does not allow a detailed separation of ordering patterns and may not accurately describe the underlying dynamics. If one is interested in details of the ordering patterns, a higher m would be required and a larger computation time is expected. In principle, one wants to ensure that all possible patterns $m!$ become visible (appear at least once). From the literature [5, 21] it can be seen that appropriate values of m can be chosen depending on the length of the time series to be analyzed, which e.g. for the case of 10^4 samples, a permutation order $m = 4$ would be adequate. The effect of the hyperparameter τ_D on the PE will be discussed along a practical example below.

To further illuminate the PE technique, an analysis of synthetic data is presented. In this use case, the PE of two uncoupled systems is calculated, namely of $X_1(t_n)$ and $X_2(t_n)$ defined as:

$$X_1(t_n) = \xi_1 \quad (2)$$

$$X_2(t_n) = \xi_2 + \alpha X_2(t_n - 1), \quad (3)$$

where ξ_i is Gaussian noise with expectation value μ_i and standard deviation σ_i ($\xi_i \sim N_i(\mu_i, \sigma_i)$) and α is an autoregressive (AR) coefficient limited to $|\alpha| < 1$. Both systems consist of random signals, however $X_2(t_n)$ has an additional first order AR term creating a dependency between the last and the upcoming realization. The time traces of the first 100 samples of both systems are depicted in figure 1. For this example, we will consider $\mu_{1,2} = 0$, $\sigma_{1,2} = 1$, $\alpha = 0.9$ and $t_n = 1, 2, \dots, 10^4$. From the waveforms it can be seen that $X_2(t_n)$ (red) is more structured and seem less random than $X_1(t_n)$ (blue).

Figure 2(a) shows the probability density functions (PDF) of the time series in figure 1. We observe that the PDF of $X_1(t_n)$ (blue) is narrower than the one from $X_2(t_n)$ (red); however, both PDFs have the same shape (normal distributions). It is noted here that, from this depiction of the one dimensional distribution, the degree of randomness of the signals cannot be determined.

For the assessment of the degree of randomness, the joint distributions of consecutive realizations from the time series

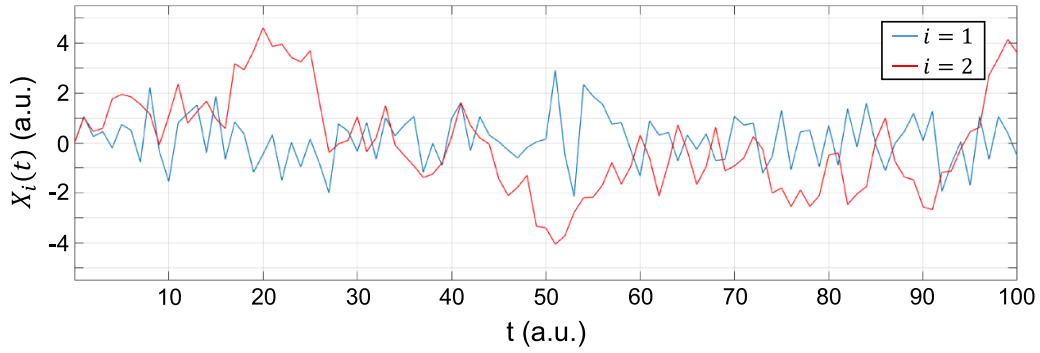


Figure 1. Time traces of synthetic data to be analyzed by means of PE. Data consists of the first 100 realizations of systems $X_1(t_n)$ and $X_2(t_n)$ as defined in equations (1) and (3).

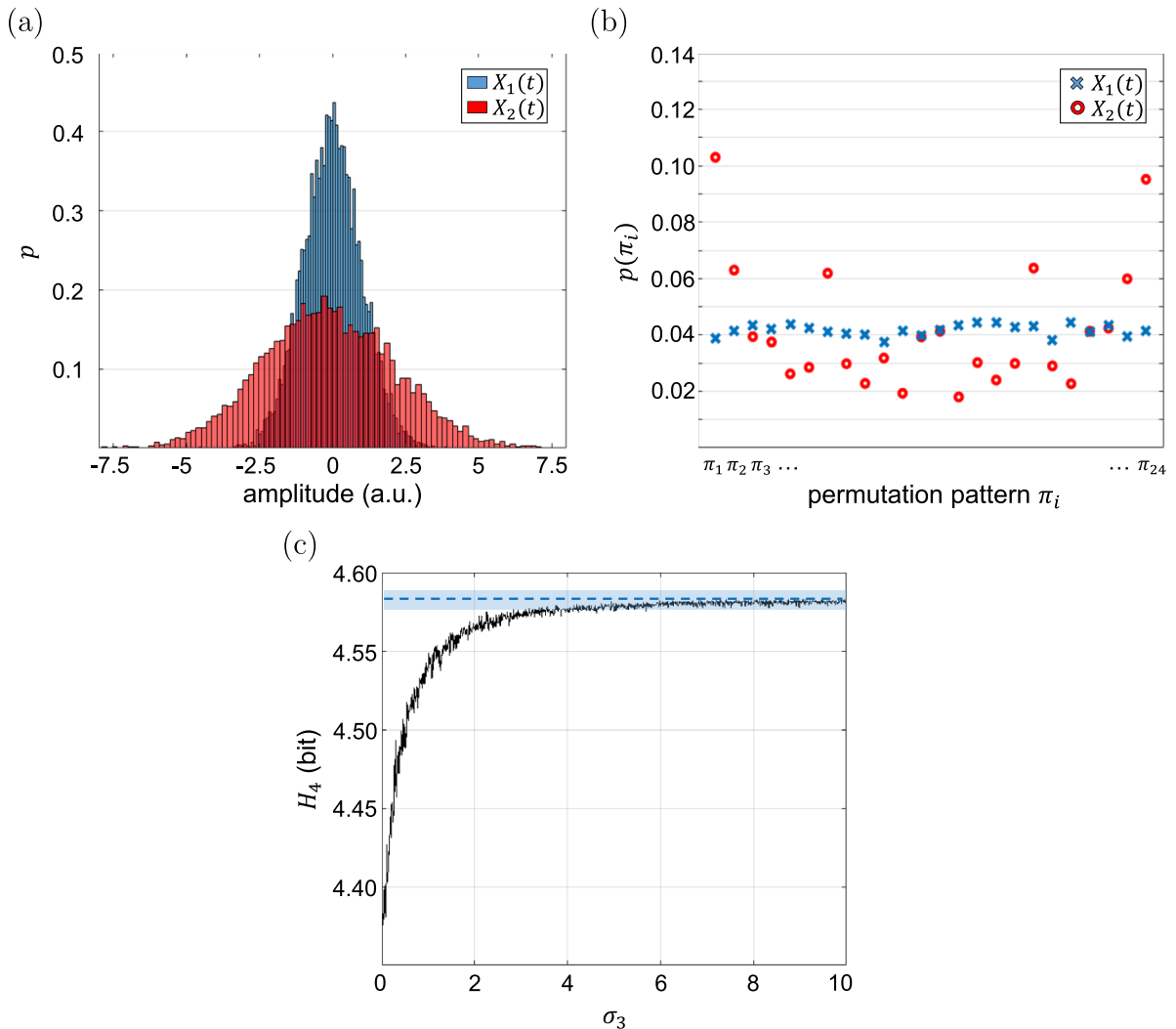


Figure 2. Analysis of uncoupled systems $X_1(t_n)$ and $X_2(t_n)$ for $t = 1, 2, \dots, 10^4$. (a) Probability density function estimate of both systems. (b) Probability distribution of permutation patterns π of 4th order of consecutive measurements ($m = 4$, $\tau_D = 1$). The 4-tuples are arranged from monotonically decreasing to monotonically increasing order patterns such that $\pi_1 = (4, 3, 2, 1)$, $\pi_2 = (4, 3, 1, 2)$, \dots , $\pi_{24} = (1, 2, 3, 4)$. (c) Permutation entropy of system $X_2(t_n)$ with varying additional noise source $\xi_3 \sim N_3(0, \sigma_3)$. The blue dashed line indicates the entropy of system $X_1(t_n)$ ($H_4 = 4.583$ bit) and the shaded area illustrates the error with a confidence interval of 99.7%.

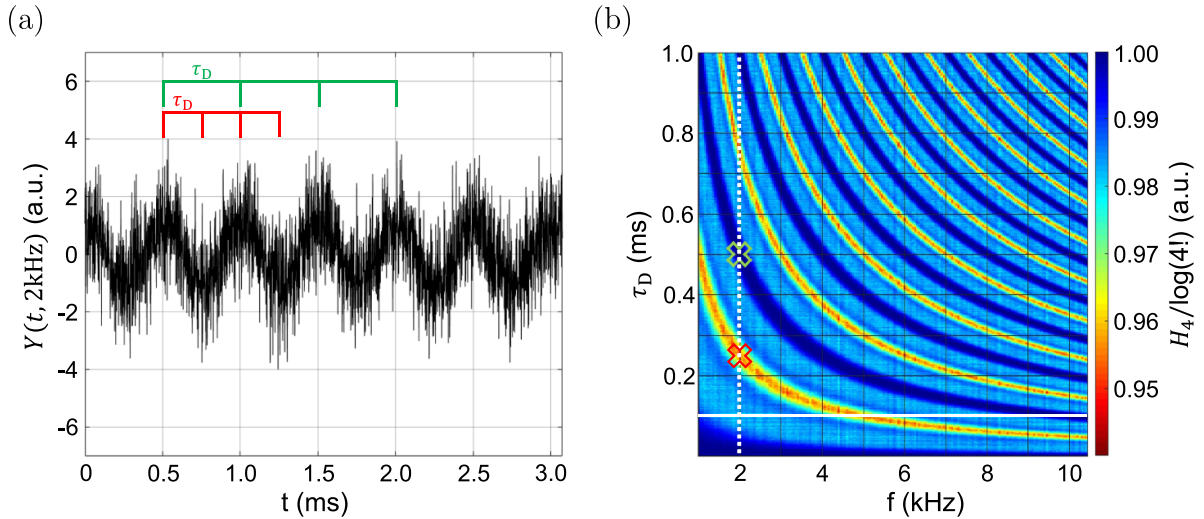


Figure 3. Calculation of permutation entropies of order $m=4$ of signals $Y(t,f) = \sin(2\pi ft) + \xi$, where $\xi \sim N(0,1)$, for the assessment of best suited embedding delay τ_D to detect structures with different frequencies. (a) Time trace of the signal with $f=2$ kHz. Minimum and maximum PE values were achieved with $\tau_D = 0.25$ ms (red) and $\tau_D = 0.50$ ms (blue); normalized to the maximum achievable entropy, $H_4/\log 4! = 0.950$ and $H_4/\log 4! = 0.999$ respectively. (b) $H_4/\log 4!$ of signals with varying f and τ_D . White solid line indicates values of PE for time series with different f and $\tau_D = 0.1$ ms; white dotted line, for the specific case $f=2$ kHz with color coded markers pinpointing embedding delays shown in (a).

illustrated in figure 1 are shown in figure 2(b). For this, a PE with $m=4$ and $\tau_D=1$ is implemented. It can be seen for the case of $X_1(t_n)$ (blue) that all $m!=24$ possible permutation patterns π have roughly equal probabilities ($p(\pi) \approx \frac{1}{24}$). On the other hand, for $X_2(t_n)$ (red) some probabilities deviate significantly from an equal distribution indicating that monotonically decreasing and increasing sequences are more frequent. This reflects the effect of the AR term (α in equation (3)) leading to more ordered patterns in $X_2(t_n)$ (red) compared to $X_1(t_n)$ (blue). Calculating the PE of the systems $X_1(t_n)$ and $X_2(t_n)$ results in 4.583 bit and 4.359 bit, respectively. This indicates a higher entropy in the time series $X_1(t_n)$ compared to $X_2(t_n)$. In other words, $X_1(t_n)$ is more random (and thus less predictable) than $X_2(t_n)$.

Now, we assess the robustness of PE. To this end, $X_2(t_n)$ is exposed to different noise levels, figure 2(c). For this, an additional i.i.d. signal $\xi_3 \sim N_3(0, \sigma_3)$ with varying σ_3 is incorporated into the time series of $X_2(t_n)$ depicted in figure 1. After a steep for low values of σ_3 , it gradually approaches the maximum PE value of $X_2(t_n)$ (blue dashed line, $H_4 = 4.583$ bit). At about $\sigma_3 > 4$ the entropies of $X_1(t_n)$ and $X_2(t_n)$ are virtually the same. For this example with normal distributions at $\sigma_{1,2} = 1$, PE is able to detect autodependencies for noise levels up to $\sigma_3 \approx 4\sigma_1$.

Now we discuss the role of the hyperparameters in the PE calculation, namely the embedding delay τ_D and the order m . The assessment of a well-suited embedding delay τ_D leading to the detection of underlying structures at different frequencies is presented in figure 3. For this, synthetic data are generated consisting of noisy sine waves $Y(t,f) = \sin(2\pi ft) + \xi$, with frequencies $f \in [1, 11]$ kHz and $\xi \sim N(0,1)$.

The waveform of $Y(t, 2 \text{ kHz})$ is shown in figure 3(a). For a time window of 10 ms, the PE of order $m=4$ is calculated for varying $\tau_D \in [0.01, 1.00]$ ms. This results in a minimum PE value with $\tau_D = 0.25$ ms (depicted in red) and maximum with $\tau_D = 0.50$ ms (green). These values, normalized to the maximum achievable entropy, are $H_4/\log 4! = 0.950$ and $H_4/\log 4! = 0.999$ respectively. This indicates an embedding delay of $\tau_D = 0.25$ ms ($1/2$ of the period T of the sine wave) to be best suited for the detection of the underlying structure with $f=2$ kHz, whereas an analysis with $\tau_D = 0.50$ ms $= T$ would not be able to differentiate between this structure and a signal fully comprised of white noise. The reason becomes obvious from figure 3(a): if the time comb samples periodic data at a fixed phase, a ranking and thus an ordinal pattern cannot be derived.

The full impact of sampling at a fixed phase is seen in figure 3(b). First, we follow the dotted line to discuss the variation of a specific delay time τ_D . This is equivalent to changing the extent of the time comb in figure 3(a). For the two indicated time combs, the PE is maximum and minimum respectively. The difference in PE (as depicted by red/green symbols in figure 3(b)) affects cases with the previously discussed sampling at the same phase of the noisy sine wave (min. PE) and at the largest variation of phases (max. PE). Expanding the discussion to an extended range of frequencies, provides a similar impact of sampling at a fixed phase but at different frequencies. This result is seen as a consecutive structure of ‘fringes’ in figure 3(b).

In practical application, combinations of frequencies f and delay times τ_D leading to normalized PE ≈ 1 are not sensitive to detect irregularities. The white line shows the choice

made for the analysis in this paper, indicating a ‘blind spot’ for $f \gtrsim 9$ kHz (but without impact on the results). A strategy to overcome this deficiency is obvious: adding an additional PE analysis at a somewhat higher τ_D does ensure a coverage at any blind spot for any frequency of interest.

3. Multivariate measurements on Wendelstein 7-X for the characterization of plasma states

Now, we analyze data taken from plasma discharges of Wendelstein 7-X. The specific discharges were conducted with magnetic field settings that lead to a comparably low value of the rotational transform (low ι configuration). Figure 4 shows an overview of the temporal evolution of some plasma quantities from the plasma discharge 20180829.24. The salient feature apparent from the waveforms of the electron temperature is a step-wise increase of T_e at the discharge time $t \approx 1.4$ s. In this time range, the heating power P and diamagnetic energy W_{dia} are roughly constant. The sudden increase is observed with different diagnostics namely the electron cyclotron emission (ECE) and the SXR diagnostic both measurements depending on T_e . This has been observed to occur in various plasma discharges with different plasma conditions.

To examine the spatio-temporal characteristics of the temperature change, highly sampled data from an ECE radiometer and from SXR diagnostic have been analyzed by means of PE. The measurements are described along with the analysis in the subsequent sections.

3.1. ECE radiometer at W7-X

ECE radiometry is employed to measure the electron temperature and to derive T_e profiles in stellarators [9]. The ECE diagnostic in W7-X measures the second harmonic X-mode emission at 2.5 T employing a heterodyne radiometer. The radiometer has a line of sight (LoS) that crosses the plasma center and consists of 32 signal channels that measure a frequency range from 126 to 162 GHz. With a sampling frequency up to 2 MHz for temperature localized measurements, the LoS of the radiometer is selected such that the magnetic field increases monotonically towards the inner side of the torus. The correspondence of electron gyration frequency and $|B|$, allows one a spatial 1D allocation of temperature measurements. Here, the specific assignment of frequencies to $|B|$ is made by calculating the field with VMEC [11], a 3D MHD equilibrium code that solves the force balance of ideal MHD equilibrium.

The ray-tracing code TRAVIS [15] is used to take into account the radiation transport effects when the temperature profiles are derived from emissivity signals of the ECE channels. The complex refraction index along the line of sight of the ECE radiometer is determined from electron density and -temperatures, mapped on magnetic coordinates from

a MHD equilibrium provided by the VMEC code. Technically, the radiation transport equation is solved such that the emissivity (and thus the respective temperatures profiles) contributing to each frequency channel is predicted. TRAVIS provides the location and width of the emissive layer at any frequency. This results in a typical spatial mapping to an effective measurement location (see figure 5(a)) with a resolution of the ECE measurements of $\Delta r \approx 1$ cm in the plasma core.

3.2. Analysis of ECE time series

The T_e profile for the discharge presented in figure 4 is shown in figure 5(a). Negative values of the normalized effective radius ρ represent regions in the high-field side (inboard), whereas positive values, regions in the low-field side (outboard). The ECE channel numbers are depicted above each data point in the profile³. We obtain a peaked T_e profile and also observe that measurements retrieved through ECE channel-#10 originate near the plasma core, in the high T_e gradient region on the low-field side.

The time series of measurements of channel-#10 ($\rho = 0.20$) recorded at a sampling frequency of 1 MHz is displayed in figure 5(b). Figure 5(b) shows a significant fluctuation level, partly due to measurement noise and partly due to plasma fluctuations. The signal is seen to fluctuate during the plasma start up phase, before reaching a stationary state from $t \approx 0.4$ s to $t \approx 1.4$ s. A spontaneous T_e increase is observed at $t \approx 1.4$ s (red dashed line) and the temperature is maintained at a second plateau in a stationary phase until $t = 2.5$ s when the heating power is modulated.

As a first step analysis, PE was applied to the waveform shown in figure 5(b). This analysis, as well as all further PE analysis presented in this paper, is conducted with a permutation order $m = 4$, an embedding delay $\tau_D = 0.1$ ms and a sliding time window of 10 ms of duration for the computation of each PE value. The calculations are performed in *MATLAB* with a code based on the algorithm presented in [22]. To claim that structures within a signal have been detected by means of PE, a detection threshold must be defined. The choice of the threshold is oriented at a significance level derived from noise data analysis. More specifically this is done by calculating the PE of 100 time series consisting of Gaussian noise ($\xi \sim N(0, 1)$) with the same hyperparameters ($m = 4$, $\tau_D = 0.1$ ms) as for the analysis of experimental data. Obviously, the most appropriate threshold will depend on the data to be analyzed, but the method employed here is well-suited to establish a basis for an analysis that requires minimal previous knowledge about the nature of the data.

The result of the PE analysis is shown in figure 6(a). For an intuitive illustration of the results, the complement of the PE

³ It can be seen that the data of channel-#16 ($\rho = -0.08$) is absent. This is due to the heating system operating at about the same frequency (≈ 140 GHz) as channel-#16 and thus, the measurements obtained through this channel are not accurate and are therefore neglected.

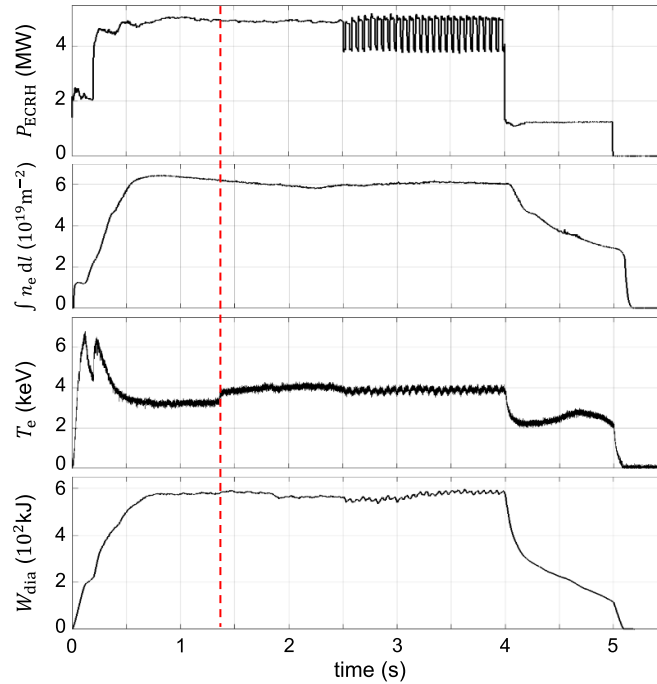


Figure 4. Time traces of low iota configuration plasma discharge 20180829.24 in W7-X (configuration B: DBM, $\langle \beta \rangle = 1.02\%$). Top-to-bottom: electron cyclotron heating power P_{ECRH} , line integrated electron density n_e , electron temperature T_e and diamagnetic energy W_{dia} . Red dashed line pinpoints the instant when a spontaneous T_e increase is observed.

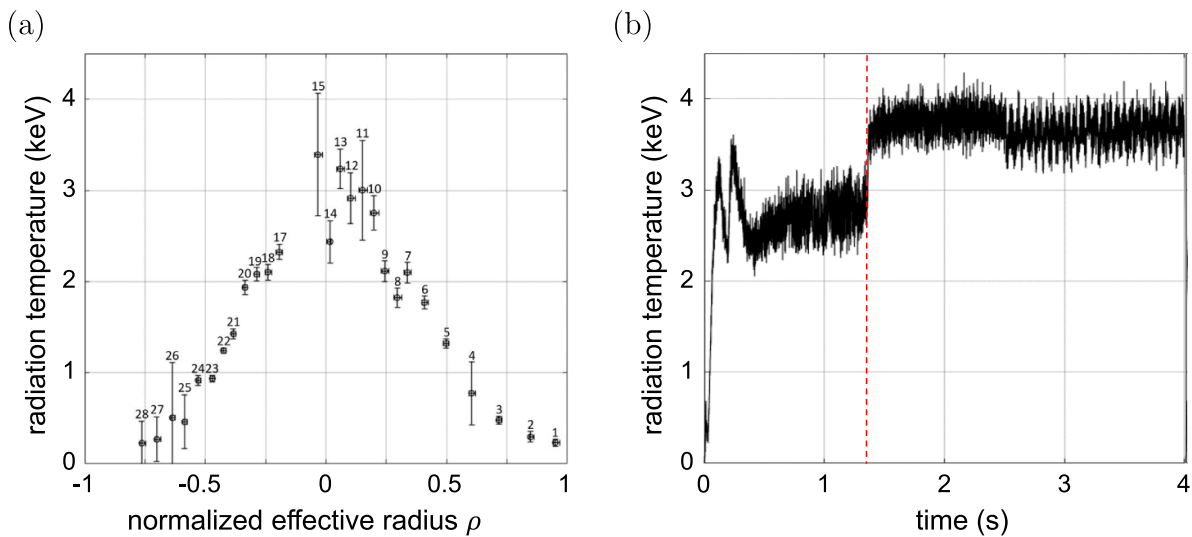


Figure 5. (a) Measured radiation temperature mapped to the effective measurement location calculated by TRAVIS in W7-X plasma discharge 20180829.24 from $t = 1.00$ s to $t = 1.05$ s. The number above each data point indicates the respective ECE channel number. (b) Radiation temperature measurements obtained through channel-#10 for the whole plasma discharge. Red dashed line indicate instant when spontaneous T_e increase is observed.

values normalized through the maximum achievable entropy is plotted in logarithmic scale. The significance threshold is $\log(1 - s) = 6.7 \times 10^{-4}$ (magenta line) and this value, multiplied by three to prevent random spikes in PE that would yield false positive detections, results in the detection threshold for

the T_e transition (blue line). We observe that the PE (black line) for $t \in [0.4, 1.4]$ s is significantly greater than for $t > 1.4$ s and is above both thresholds. This is also observed for a moving average (MA) over a sliding window of 10 ms of the PE signal (green line). Hence, PE differentiates between the time

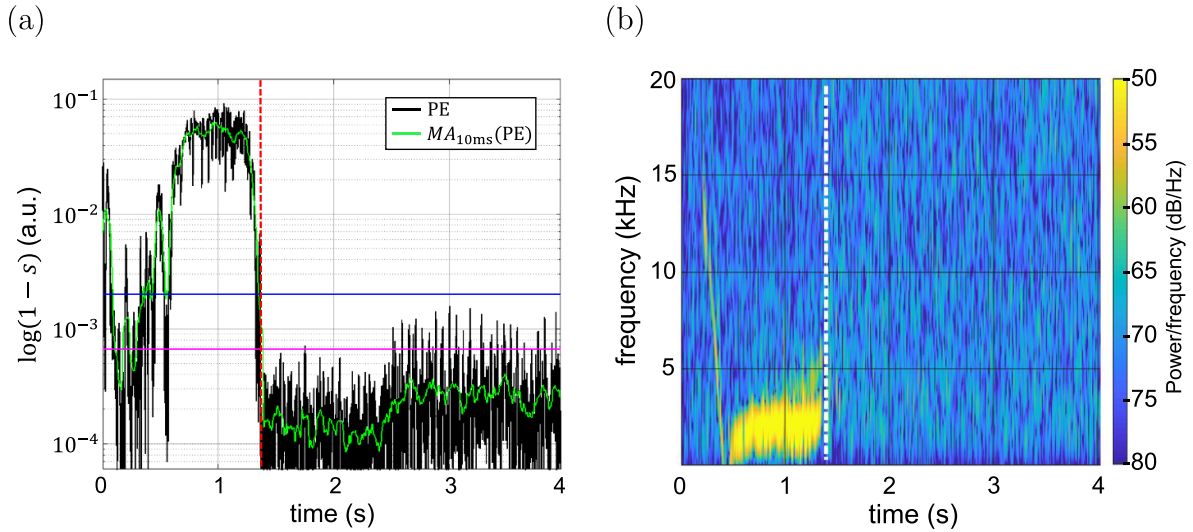


Figure 6. Analysis of ECE measurements obtained through signal channel-#10 from plasma discharge 20180829.24 in W7-X. Red and white dashed lines indicate instant when spontaneous T_e increase is observed. (a) Permutation entropy analysis with permutation order $m = 4$ and embedding delay $\tau_D = 0.1$ ms for a sliding time window of 10 ms of duration: complement of PE values s normalized through the maximum achievable entropy. Green line depicts moving average over a sliding window of 10 ms, magenta line displays the PE significance threshold derived from noise data analysis and blue line indicates the T_e transition detection threshold. (b) Spectrogram computed through the short-time Fourier transform.

windows before and after the T_e transition (red dashed line). Other than this distinction, a small fluctuation in the PE analysis can be seen between the significance threshold and the T_e transition detection threshold, which goes along with the heating power modulation starting from $t \approx 2.5$ s. This MA signal is better suited than the original one to serve as *trigger signal* in data mining by avoiding large excursions (compare black and green lines in figure 6(a)). Figure 6(b) shows spectral analysis of the same data computed using the *MATLAB* built-in function *spectrogram* [16]. All spectral analysis throughout this paper are computed through short-time Fourier transforms with hamming windows of 1 ms of duration and 10% overlap between windows. Through spectral analysis, a quasi coherent mode structure with a fluctuation frequency between $f \approx 2$ kHz and $f \approx 3$ kHz is observed between $t \approx 0.4$ s and $t \approx 1.4$ s, which vanishes once the T_e transition occurs (white dashed line). Comparing figures 6(a) and (b) indicates a smaller PE to result from a more ordered time series as reflected by the spectral maximum in figure 6(b).

Now, PE and spectral analysis are applied on all signal channels such that the localization of the structures can be examined. Both methods identified the same ECE channels for which the MHD activity was observed (see figure 7). More specifically, the T_e profile is separated in three types of regions: MHD activity was observed (red shaded area), no activity was observed (white shaded area) and no fluctuation analysis was possible due to low signal-to-noise ratio (gray shaded area). Even though, the analysis could not be performed in all regions, MHD activity is localized in the core. Thus, through both methods, spectral analysis and PE the

mode activity could be allocated along the radial coordinate and lies in the high gradient region near the plasma core.

3.3. XMCTS at W7-X

The SXR multi-camera tomography system (XMCTS) measures emissions through pinhole cameras arranged in an up-down symmetry in a poloidal plane [3], where the flux surfaces have a triangular shape as seen in figure 8. This non-invasive diagnostic consists of 20 SXR cameras arranged poloidally to cover the plasma from multiple views and each camera is equipped with 18 photodiodes to measure radiation in the energy range of approximately 1–12 keV [4]. Figure 8 depicts the flux surfaces for the low-iota configuration B (DBM, $\beta = 1.02\%$) and the line of sight geometry of this diagnostic, specifically, the region covered by SXR camera 4A (gray shaded region) and LoS-#8 (white dashed line). The SXR emissions measured emerge mainly from contributions from bremsstrahlung ($\propto n_e^2 \sqrt{T_e}$), recombination and line radiation. Through high sampling rate and spatial resolution, this diagnostic is able to resolve MHD instabilities in a poloidal cross section of the plasma.

3.4. Analysis of SXR time series

The radiation recorded through SXR camera 4A for plasma discharge 20180829.24 in W7-X is presented in figure 9. The waveforms in red (figure 9(a)) correspond to measurements closest to the vessel's inner wall (high-field side), whereas

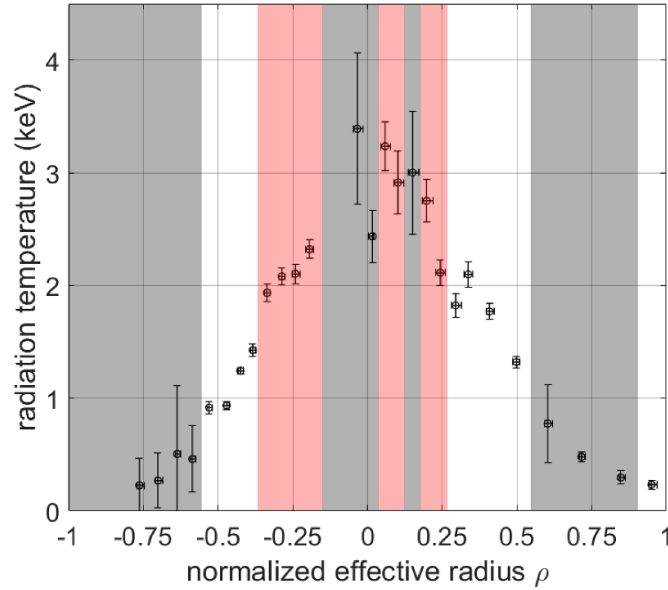


Figure 7. Measured radiation temperature mapped to the effective measurement location calculated by TRAVIS in W7-X plasma discharge 20180829.24 from $t = 1.00$ s to $t = 1.05$ s. Red shaded areas indicate regions where MHD activity was observed. In white are regions where this activity was not observed and, in gray, regions where no fluctuation analysis was possible due to low signal-to-noise ratio.

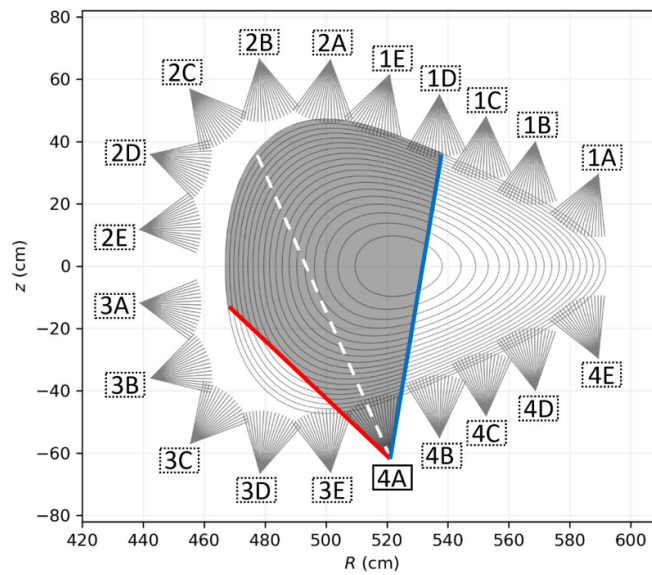


Figure 8. Setup of the soft x-ray multi-camera tomography system depicting the lines of sight geometry for all cameras installed (1A – 4E) and the flux surfaces for the low iota configuration B (DBM, $\beta = 1.02\%$). The shaded area indicates the region from which the radiation measured through SXR camera ‘4A’ comes from (delimited by the red and blue lines). The white dashed line depicts one of the 18 lines of sight (specifically, LoS-#8) available for the measurements.

waveforms in blue, correspond to measurements near the plasma center (low-field side, see figure 8).

The channels showing the innermost lines of sight are arranged in figure 9(b), where SXR signals measuring similar intensities but from opposing locations w.r.t. the plasma center can be observed. When T_e spontaneously rises (black dashed line), a significant branching between the off-axis

measurements and their respective counterparts is seen. Radiation measurements taken more laterally on the high-field side (red) drop slightly in intensity, whereas measurements in the low-field side (blue) increase. The difference in the temporal evolution of the ECE and SXR signals provides clear evidence that the emissivity change is localized to the innermost channels. Moreover, while ECE data showed a

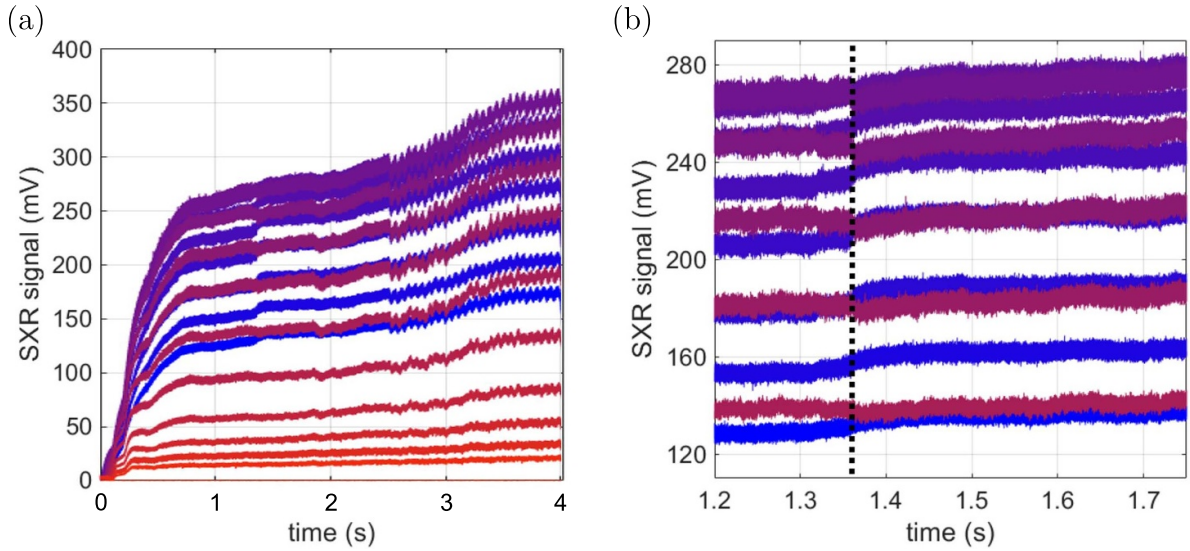


Figure 9. SXR measurements obtained through camera ‘4A’ for low-iota configuration plasma discharge 20180829.24 in W7-X. Black dashed line indicates instant when spontaneous T_e increase is observed. (a) Time series recorded through all 18 photodiodes: red plots depicting lines of sight closer to the periphery and blue plots, regions near the plasma center (see figure 8). (b) Magnification of (a) exhibiting bifurcation of signals after T_e transition.

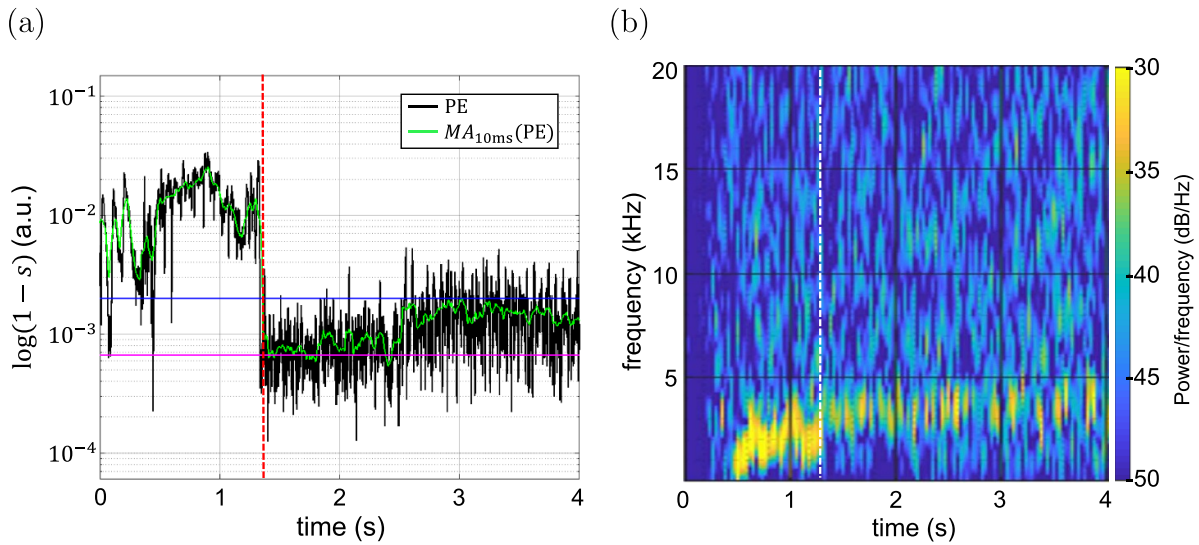


Figure 10. Analysis of SXR measurements obtained through camera ‘4A’ LoS-#8, from plasma discharge 20180829.24 in W7-X. Red and white dashed lines indicate instant when spontaneous T_e increase is observed. (a) Permutation entropy analysis with permutation order $m = 4$ and embedding delay $\tau_D = 0.1$ ms for a sliding time window of 10 ms of duration: complement of PE values s normalized through the maximum achievable entropy. Green line depicts moving average over a sliding window of 10 ms, magenta line displays the PE significance threshold derived from noise data analysis and blue line indicates the T_e transition detection threshold. (b) Spectrogram computed through short-time Fourier transform revealing two structures around 1–4 kHz.

localized increase of T_e , the simultaneously observed increase and decrease of SXR signal ($I \propto n_e^2 \sqrt{T_e}$) allows one to conclude that the plasma density is also affected in the transition.

Now we conduct the PE and spectral analysis of density and temperature dependent SXR data. The PE analysis ($m = 4$, $\tau_D = 0.1$ ms) as shown in figure 10(a) indicates a clear

detection of structures from plasma start up until the instance when the T_e suddenly rises (red dashed line). From this point in time onwards, PE (black line) detects structures with values above the significance threshold (magenta line) and partially above the T_e detection threshold (blue line). The MA signal also detects structures above the significance threshold after $t \approx 1.4$ s, however not above the T_e detection threshold. The

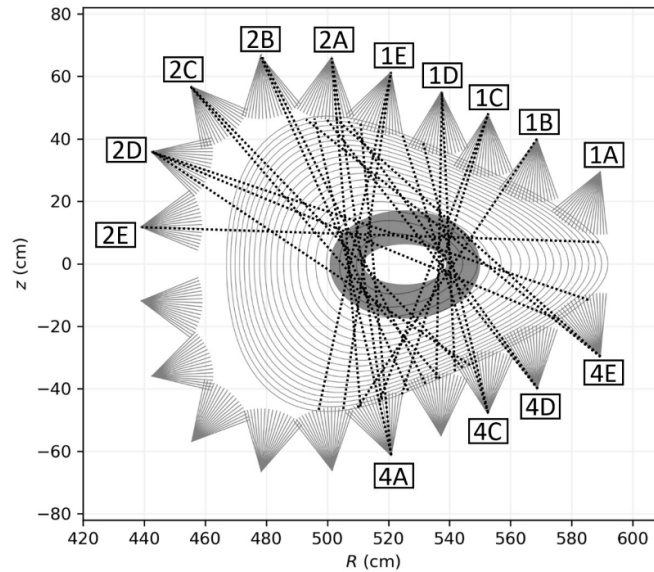


Figure 11. Localization of MHD activity in the poloidal plane through the analysis of SXR measurements in W7-X from plasma discharge 20180829.24. Dotted lines indicate lines of sight that detected MHD activity. Gray area depicts locations with high density of crossings between dotted lines suggesting a 2D localization of the activity.

next step is to identify the structures detected by the PE analysis through spectral analysis as shown in figure 10(b). From this analysis, two different structures can be observed: a predominant structure in a frequency range between $f = 2$ kHz and $f = 4$ kHz taking place between plasma start up and the T_e transition (white dashed line), and a weaker in power structure in the slightly higher frequency range (up to $f \approx 5$ kHz) that extends until the plasma is terminated. The second structure is observed in the PE analysis, however it lies between the significance threshold and the T_e transition detection threshold. Therefore, the distinction between the time windows before and after the T_e transition is in the PE analysis most evident. The computing times for both of the analysis lie around $t_{PE} = 0.49$ s and $t_{FFT} = 13.83$ s, PE being clearly faster for the analysis of a ≈ 5.5 s long time series with a sampling rate of 2 MHz.

Assuming that SXR data is proportional to $n_e^2 \sqrt{T_e}$, the ECE signals increase only locally and the total energy did not show any response, the previous observations are an indication of the redistribution of the electron pressure. Expanding the time series analysis to all available photodiodes from the SXR cameras, the MHD activity can be localized in a 2D tomographic reconstruction of a plasma poloidal cross section. The cameras available for the analysis are shown in figure 11 as well as the lines of sight (black dotted lines) where the activity preceding the transition was identifiable by means of PE. From the density of the crossings between these lines of sight, a rough idea of the spatial location of the activity can be estimated (gray shaded area). From this simplistic tomographic approach, we observe that the activity lies near the plasma center as also observed from the ECE data analysis in the previous section. Furthermore, the tomographic approach allows to exclude the occurrence of the MHD activity on axis.

3.5. Data mining with PE

Now, we investigate the capability of PE for an automated detection of the temperature transition in a large amount of data. Purpose of the survey is to identify the temperature bifurcation using PE at settings used in the previous section ($m = 4$, $\tau_D = 0.1$ ms). The success rate of this data mining procedure is derived from the number of successful detections of transitions and the number of false positives. To this end, ECE data from a full shot-day on W7-X are analyzed to detect spontaneous T_e transitions. Since the ECE signal reflects the electron temperature rather than a combination of n_e and T_e , only the ECE data were chosen for the data mining. The PE (at fixed settings) was applied on ECE data. Table 1 summarizes for which discharges PE detected a temperature transition at a time t_B , and for which discharges no transition could be revealed. The result from the findings in table 1 is that PE detects all transitions and no false positives were found, i.e. PE detected all T_e transitions when using a MA of the PE over a sliding time window of 10 ms as trigger signal as shown in figures 6 and 10. It is worth mentioning, that the first 100 ms of every discharge were excluded from the analysis to avoid the detection of structures due to plasma start-up.

To validate the PE findings, spectrogram were calculated and the frequency of a accompanying MHD activity is added to the transition in table 1. The spectrogram confirms the transition detected by PE but also reveals additional power spectral densities also at varying frequencies. E.g. in figure 6, a peak steadily decreasing in the plasma build-up phase adds signal contributions that are hard to discriminate. Even more ambiguous, the spectrogram of soft-x ray data (figure 10) indicate spurious power spectral densities even after the T_e transition. Contrasting the more ambiguous findings from spectral analysis, the PE analysis offered (for the data set in table 1)

Table 1. Detection of spontaneous T_e transitions in bulk data analysis by means of permutation entropy in W7-X plasma discharges. PE analysis performed on ECE data with permutation order $m = 4$ and embedding delay $\tau_D = 0.1$ ms for a sliding time window of 10 ms. Plasma parameters before the transition are shown, including increment in electron temperature measured through ECE signal channel-#10 $\Delta T_{e, \text{ch}\#10}$ and frequency f of the MHD activity preceding the transition.

Discharge ID	P_{ECRH} (MW)	$\int \text{ndl}$ (10^{19} m^{-2})	t_B (s)	T_e (keV)	ΔT_e (keV)	f_{ECE} (kHz)
20180829.5	5.0 ± 0.2	4.0 ± 0.1	—	—	—	—
20180829.6	5.02 ± 0.02	3.43 ± 0.03	3.7 ± 0.1	3.35 ± 0.02	0.25 ± 0.02	7.5–10
20180829.7	3.71 ± 0.02	3.01 ± 0.03	2.1 ± 0.1	3.47 ± 0.03	0.33 ± 0.03	7–10
20180829.8	3.62 ± 0.02	2.60 ± 0.03	0.9 ± 0.1	4.04 ± 0.02	0.17 ± 0.02	7–8
20180829.9	3.72 ± 0.03	2.21 ± 0.02	0.9 ± 0.1	4.22 ± 0.04	1.00 ± 0.04	7–8
20180829.12	3.5 ± 0.2	2.0 ± 0.2	—	—	—	—
20180829.15	2.0 ± 0.1	2.0 ± 0.2	—	—	—	—
20180829.16	5.01 ± 0.02	5.01 ± 0.02	1.6 ± 0.1	2.79 ± 0.02	0.64 ± 0.02	2.5–3.5
20180829.17	4.83 ± 0.03	3.61 ± 0.03	1.2 ± 0.1	2.83 ± 0.01	0.18 ± 0.01	8–9
20180829.18	3.50 ± 0.02	4.10 ± 0.02	1.7 ± 0.1	2.81 ± 0.02	0.38 ± 0.02	8–9
20180829.19	3.5 ± 0.2	4.0 ± 0.2	—	—	—	—
20180829.20	2.42 ± 0.03	4.02 ± 0.02	2.6 ± 0.1	1.94 ± 0.03	0.37 ± 0.03	2–2.5
20180829.21	3.55 ± 0.02	4.34 ± 0.01	1.2 ± 0.1	3.02 ± 0.02	0.37 ± 0.02	2–3
20180829.22	1.5 ± 0.1	4.0 ± 0.2	—	—	—	—
20180829.23	2.0 ± 0.1	4.0 ± 0.1	—	—	—	—
20180829.24	4.97 ± 0.04	6.23 ± 0.04	1.4 ± 0.1	2.81 ± 0.03	0.85 ± 0.03	2–3
20180829.25	5.04 ± 0.03	6.33 ± 0.03	1.1 ± 0.1	1.81 ± 0.03	0.31 ± 0.03	2–3
20180829.26	5.00 ± 0.04	6.30 ± 0.04	1.4 ± 0.1	2.94 ± 0.03	0.88 ± 0.03	2–3
20180829.27	3.61 ± 0.03	6.04 ± 0.03	2.5 ± 0.1	2.57 ± 0.03	0.41 ± 0.03	4–5
20180829.28	3.6 ± 0.2	6.0 ± 0.5	—	—	—	—
20180829.31	3.5 ± 0.2	6.5 ± 0.4	—	—	—	—
20180829.32	2.04 ± 0.02	3.98 ± 0.02	2.1 ± 0.1	1.75 ± 0.02	0.25 ± 0.02	3–4
20180829.33	2.05 ± 0.02	3.96 ± 0.02	2.1 ± 0.1	1.82 ± 0.03	0.25 ± 0.03	3–4
20180829.34	2.05 ± 0.01	4.05 ± 0.02	2.0 ± 0.1	1.74 ± 0.03	0.23 ± 0.03	2–4
20180829.35	2.02 ± 0.01	3.73 ± 0.01	2.3 ± 0.1	1.80 ± 0.03	0.25 ± 0.03	1–4
20180829.37	5.0 ± 0.2	4.3 ± 0.1	—	—	—	—
20180829.38	5.4 ± 0.2	3.5 ± 0.1	—	—	—	—
20180829.39	5.36 ± 0.04	2.08 ± 0.01	1.6 ± 0.1	4.81 ± 0.04	1.21 ± 0.04	6–7
20180829.40	5.51 ± 0.03	2.02 ± 0.03	3.1 ± 0.1	5.02 ± 0.03	1.06 ± 0.03	5–9
20180829.41	5.3 ± 0.2	2.1 ± 0.1	—	—	—	—
20180829.42	5.3 ± 0.1	2.3 ± 0.2	—	—	—	—
20180829.43	5.3 ± 0.2	2.6 ± 0.2	—	—	—	—
20180829.48	3.0 ± 0.3	3.5 ± 0.1	—	—	—	—
20180829.49	3.1 ± 0.2	3.0 ± 0.1	—	—	—	—
20180829.50	3.2 ± 0.2	3.1 ± 0.2	—	—	—	—

a straight forward setting to define a statistically based PE threshold for systematically detecting previously unrevealed temperature bifurcation.

4. Discussion and conclusions

The applicability of PE as a first step analysis on plasma data over a wide range of plasma conditions is broad and serves as a tool to rapidly and robustly detect underlying dynamics in time series. This method allowed an automated analysis of bulk data, which resulted in the detection of localized T_e fluctuations in low-iota configuration discharges in W7-X. PE as a data mining tool allowed one to discriminate shots with and without T_e transitions. The results of the PE analysis were supported by spectral analysis, however, the former was shown to be at least 25 times faster to compute for this case. We conclude that PE can be used to report changes of the plasma state

as fast as ~ 0.1 ms which is much faster than the energy confinement time (~ 100 ms). It is concluded that PE has a large potential for real-time detection of changes to, e.g. induce interlocks or other control interventions.

Data availability statement

The data that support the findings of this study are available upon reasonable request from the authors.

Acknowledgments

This work has been carried out within the framework of the EUROfusion Consortium, funded by the European Union via the Euratom Research and Training Programme (Grant Agreement No. 101052200—EUROfusion). Views and opinions expressed are however those of the author(s) only and

do not necessarily reflect those of the European Union or the European Commission. Neither the European Union nor the European Commission can be held responsible for them.

ORCID iDs

J F Guerrero Arnaiz  <https://orcid.org/0000-0002-7650-2918>

A Dinklage  <https://orcid.org/0000-0002-5815-8463>

J Geiger  <https://orcid.org/0000-0003-4268-7480>

C Brandt  <https://orcid.org/0000-0002-5455-4629>

J Schilling  <https://orcid.org/0000-0002-6363-6554>

K Rahbarnia  <https://orcid.org/0000-0002-5550-1801>

M Zanini  <https://orcid.org/0000-0002-8717-1106>

References

- [1] Bandt C and Pompe B 2002 Permutation entropy: a natural complexity measure for time series *Phys. Rev. Lett.* **88** 174102
- [2] Bandt C and Shiha F 2007 Order patterns in time series *J. Time Ser. Anal.* **28** 646–65
- [3] Brandt C, Broszat T, Thomsen H, Laube R, Marquardt M, Franz P, Schülke M, Sieber T and Weißflog S 2017 Installation of the soft x-ray multi-camera tomography system (XMCTS) in the Wendelstein 7-X stellarator *Fusion Eng. Des.* **123** 887
- [4] Brandt C *et al* 2020 Soft x-ray tomography measurements in the Wendelstein 7-X stellarator *Plasma Phys. Control. Fusion* **62** 035010
- [5] Cuesta-Frau D, Murillo-Escobar J P, Orrego D and Delgado-Trejos E 2019 Embedded dimension and time series length. Practical influence on permutation entropy and its applications *Entropy* **21** 385
- [6] Dudewicz E, Gyorfi L and van der Meulen E 1997 Nonparametric entropy estimation: an overview *Int. J. Sci. Res. Math. Stat. Sci.* **6** 17
- [7] Ferreira D R, Carvalho P J, Sozzi C, Lomas P J and Contributors J 2020 Deep learning for the analysis of disruption precursors based on plasma tomography *Fusion Sci. Technol.* **76** 901–11
- [8] Grieger G *et al* 1992 Physics optimization of stellarators *Phys. Fluids B* **4** 2081
- [9] Hartfuss H J, Geist T and Hirsch M 1997 Heterodyne methods in millimetre wave plasma diagnostics with applications to ECE, interferometry and reflectometry *Plasma Phys. Control. Fusion* **39** 1693
- [10] Henry M and Judge G 2019 Permutation entropy and information recovery in nonlinear dynamic economic time series *Econometrics* **7** 10
- [11] Hirshman S, van RIJ W and Merkel P 1986 Three-dimensional free boundary calculations using a spectral green's function method *Comput. Phys. Commun.* **43** 143
- [12] Jordan D, Stockmanns G and Kochs E 2007 Permutation entropy of the EEG indicates increase and decrease of the anesthetic level *Anesthesiology* **107** A800
- [13] Li X, Cui S and Voss L 2008 Using permutation entropy to measure the electroencephalographic effects of sevoflurane *Anesthesiology* **109** 448
- [14] Maggs J E, Rhodes T L and Morales G J 2015 Chaotic density fluctuations in L-mode plasmas of the DIII-D tokamak *Plasma Phys. Control. Fusion* **57** 045004
- [15] Marushchenko N, Turkin Y and Maassberg H 2014 Ray-tracing code TRAVIS for ECR heating, EC current drive and ECE diagnostic *Comput. Phys. Commun.* **185** 165
- [16] *MATLAB and Statistics Toolbox Release 2018a* (Natick, MA: The Mathworks, Inc.) (available at: www.mathworks.com/help/signal/)
- [17] Nührenberg J and Zille R 1986 Stable stellarators with medium β and aspect ratio *Phys. Lett. A* **114** 129
- [18] Olofson E, Sleight J and Dahan A 2008 Permutation entropy of the electroencephalogram: a measure of anaesthetic drug effect *Br. J. Anaesth.* **101** 810
- [19] Onchi T, Fujisawa A, Sanpei A, Himura H and Masamune S 2017 Permutation entropy and statistical complexity in characterising low-aspect-ratio reversed-field pinch plasma *Phys. Scr.* **92** 055601
- [20] Škvára V, Šmídl V, Pevný T, Seidl J, Havránek A and Tskhakaya D 2020 Detection of alfvén eigenmodes on COMPASS with generative neural networks *Fusion Sci. Technol.* **76** 962–71
- [21] Staniek M and Lehnertz K 2007 Parameter selection for permutation entropy measurements *Int. J. Bifurc. Chaos* **17** 3729–33
- [22] Unakafova V A and Keller K 2013 Efficiently measuring complexity on the basis of real-world data *Entropy* **15** 4392–415
- [23] Wolf R C *et al* 2017 Major results from the first plasma campaign of the Wendelstein 7-X stellarator *Nucl. Fusion* **57** 102020
- [24] Zhang N, Sun Y, Zhang Y, Yang P, Lin A and Shang P 2019 Distinguishing stock indices and detecting economic crises based on weighted symbolic permutation entropy *Fluct. Noise Lett.* **18** 1950026
- [25] Zunino L, Fernández Bariviera A, Guercio M B, Martinez L B and Rosso O A 2012 On the efficiency of sovereign bond markets *Physica A* **391** 4342

A.3 Article III

Spontaneous transitions to high core-electron temperatures in W7-X low-iota plasmas close to electron-root condition

J. F. Guerrero Arnaiz, A. Dinklage, A. Könies, C. Nührenberg, A. Zocco, H. Bouvain, M. Borchardt, C. Brandt, N. Chaudhary, J. Geiger, M. Hirsch, R. Kleiber, K. Rahbarnia, A. Mishchenko, H. Thomsen, M. Zanini and the W7-X Team

Plasma Physics and Controlled Fusion, Submitted for publication July 2023

Spontaneous transitions to high core-electron temperatures in W7-X low-iota plasmas close to electron-root condition

J F Guerrero Arnaiz^{1,2}, A Dinklage^{1,2}, A Könies¹,
C Nührenberg¹, A Zocco¹, H Bouvain^{1,2}, M Borchardt¹,
C Brandt¹, N Chaudhary¹, J Geiger¹, M Hirsch¹, R Kleiber¹,
K Rahbarnia¹, A Mishchenko¹, H Thomsen¹, M Zanini¹ and
the W7-X Team

¹ Max-Planck-Institut für Plasmaphysik, Greifswald, Germany

² Universität Greifswald, Institut für Physik, Greifswald, Germany

E-mail: juan.fernando.guerrero.arnaiz@ipp.mpg.de

Abstract.

Transitions to core-electron-root-confinement (CERC) regime are examined in presence of low-order rational values of the rotational transform ι in Wendelstein 7-X. Experiments were conducted at densities and heating powers close to the bifurcation from pure ion-root to CERC conditions. The transitions were found in the low- ι configuration at stationary plasma conditions, but at evolving plasma currents. The transitions occurred in the plasma are linked with high ECRH power in the plasma start-up phase. Analysis of the effects due to the ramping plasma current indicate a change of the rotational transform (ι) profile temporarily crossing low-order rational values. The transition, in a narrow range of plasma currents and supported by simulations of the shielding current evolution, is consistent with the observed increase of the central electron temperature. Before these transitions, low frequency fluctuation activity was identified which ceased when higher electron temperatures were attained i.e. following the transition to positive central radial electric field (E_r) values. The preceding activity is characterized through experimental and numerical approaches. Ideal and non-ideal MHD analysis, including the effects of magnetic islands and radial electric fields, indicate that a plasma instability is unlikely, but side bands of zonal flow oscillations, Doppler-shifted due to the ambient electric field are most consistent with the experimental findings.

1. Introduction

Wendelstein 7-X (W7-X) is an optimized, superconducting stellarator [1, 2]. The main goal of W7-X is to demonstrate the feasibility of steady-state operation of stellarators and to explore the performance relevant to fusion conditions. To this end, it is crucial to understand how favorable plasma confinement regimes, i.e. the electron-root confinement (CERC) regime [3], depend on the different plasma parameters. More specifically, it is imperative to identify and characterize the physical mechanisms that trigger transitions to different confinement regimes if those occur. Since many of those transitions occur spontaneously, we conducted a data mining study [4] in discharges at conditions close to the transition from ion- (the other stable radial electric field E_r solution) to electron-root confinement regime [5]. We identified discharges undergoing a typical transition pattern accompanied with broad-band oscillations, and these discharges are analyzed in this paper.

The core-electron-root-confinement (CERC) is a stellarator specific neoclassical transport regime with spatial regions at positive radial electric fields and a localized high E_r -shear region giving rise to a transport barrier [3]. CERC is resulting from multiple roots of the ambipolarity condition, i.e. ion and electron fluxes may balance at different radial electric fields. This can happen in stellarators if particles reside at low collisionality where electron transport is much affected by E_r . Since plasmas at low collisionality are expected at fusion conditions, the understanding of CERC and its dependency on the magnetic configuration contributes to a broader understanding of reactor scale plasmas.

To identify CERC is an improved confinement regime related to the transition to the electron-root solution of the ambipolarity condition and is characterized by peaked electron temperatures and positive radial electric field E_r in the plasma center [3]. The electron-root E_r suppresses unfavorable $1/\nu$ transport, which is one of the major goals for stellarator optimization [6].

Transitions to high core-electron temperatures were observed in experiments with evolving rotational transform ι conducted in the fusion research device Heliotron-J (H-J) [7] and the heliac TJ-II [8, 9]. In H-J, spontaneous increases of the electron temperature T_e were detected going along the evolution of ι and its crossing through a specific rational value. Also, during ion- to core electron-root confinement transitions in the Compact Helical System (CHS), it was observed that magnetic perturbations such as Alfvén eigenmodes were capable of triggering these transitions [10]. The triggering of the transition through an Alfvén eigenmode is suspected to be due to a loss of fast ions that modified the potential profile. Nevertheless, the interplay between the aforementioned mechanisms and further candidates that may play a major role in the transitions has not yet been fully explored and are therefore systematically addressed in this paper.

Here, we report on apparently spontaneous transitions to CERC regime in specific magnetic configurations, observed in W7-X. A specific feature complementing these transitions was observed, namely preceding fluctuation activity at about $f \sim 1$ kHz

(different to the reported transitions in H-J and TJ-II). In this paper, we characterize this feature, explore the role of plasma parameters, ι and E_r on the activity, and examine potential instability mechanisms by conducting ideal and non-ideal MHD stability analysis. We will also provide evidence that low-order rational magnetic surfaces may trigger the transitions observed.

2. Multivariate measurements on Wendelstein 7-X for the characterization of plasma states

W7-X is equipped with different diagnostics to ensure optimal plasma monitoring and operation. In this paper, we will focus on the evolution of the electron density n_e , the electron temperature T_e , the soft-X ray emissions, the diamagnetic energy W_{dia} and the total plasma current I_p .

For local measurements of n_e and T_e , Thomson scattering diagnostic is employed. For this, periodically pulsed neodymium-doped yttrium aluminum garnet laser is used, along interference filter polychromators and silicon avalanche diodes as detectors [11]. This system provides n_e and T_e profiles of the plasma at a sampling frequency of 30 Hz, and up to 10 kHz in burst mode.

The T_e data presented and analyzed throughout this paper is also derived from measurements performed by the electron cyclotron emission (ECE) diagnostic [12–14]. ECE data allows us to examine fluctuations in the emissivity given its high sampling rate of up to 2 MHz. To this end, a heterodyne radiometer is employed to measure the second harmonic X-mode emission along a line of sight crossing the plasma center close to the bean-shaped cross section at largest toroidal curvature. To spatially resolve the emission along the line of sight, 32 signal channels measuring a frequency range of 126 – 162 GHz are operated. A detailed simulation of radiative transport provides also radial profiles of the electron temperature.

The soft X-ray multi-camera tomography system (XMCTS) measures emissions through pinhole cameras arranged in an up-down symmetry in the poloidal plane [15], where the flux surfaces have a triangular shape. This non-invasive diagnostic consists of 20 soft-X ray cameras that measure radiation in the energy range of 1 – 12 keV through 18 photodiodes each, also with a sampling frequency of up to 2 MHz. Through high sampling rate and adequate spatial resolution, accurate tomographic reconstructions are possible, thus being able to resolve MHD instabilities in a poloidal cross section of the plasma [16].

Finally, W_{dia} and I_p are derived from signals from diamagnetic loops measuring the diamagnetic flux, and Rogowski coils respectively. The former employs a set of three diamagnetic loops to measure changes of the toroidal magnetic flux originating from the diamagnetic current flowing perpendicular to the magnetic field [17], and the latter is inferred from a single Rogowski coil located in the inner surface of the plasma vessel [18].

2.1. Overview of low-iota configuration plasma with spontaneous transition

As an example of a typical plasma discharge examined in this study that displays a spontaneous transition to high core-electron temperatures, Fig. 1 shows an overview of the temporal evolution of some plasma quantities of the plasma discharge 20180829.24. More specifically, the electron cyclotron resonance heating power P_{ECRH} is illustrated in Fig. 1(a), the line integrated electron density n_e in Fig. 1(b), the ECE data T_e^{rad} from a channel (channel-#13) with predominant central emission calibrated to its radiative temperature in Fig. 1(c), soft-X ray emission $\varepsilon_{\text{soft-X}}$ with highest signal contribution from the high gradient region in Fig. 1(d), the diamagnetic energy W_{dia} in Fig. 1(e) and the plasma current I_p in Fig. 1(f).

From the waveforms presented, the salient feature is the step-wise increase of T_e at $t \approx 1.4$ s (red dashed line). This occurs at a time window in which P_{ECRH} , n_e , and W_{dia} remained roughly constant. It is this phenomenology that is meant to be the observed spontaneous transition. In the examined data-set, the transition identified in Fig. 1(c) and (d) takes place in plasma discharges with evolving I_p under different plasma conditions.

To provide experimental evidence for a quasi-coherent fluctuation, a spectral analysis of the ECE data presented in Fig. 1(c) is illustrated in Fig. 1(g). The spectrogram was computed through short-time Fourier transform with a Hamming window of 10 ms of duration and 10% overlap between windows. During the plasma start-up, the heating power was swiftly ramped up to roughly 2 MW. The heating power was maintained, while the electron density continued increasing and the electron temperature started relaxing. At $t = 0.2$ s (black dashed line) the heating power was again increased to approximately 4.5 MW. At this instance, we observe fluctuation activity appearing in the form of a down-chirp starting with a frequency $f = 15$ kHz and decreasing until reaching approximately 0.5 kHz at $t = 0.45$ s. After reaching the lowest frequency, the heating power is increased for a second time to 5 MW, and the frequency of the activity rises until saturating at roughly 2 kHz. The first harmonic at 4 kHz can also be seen, which starts to slightly increase before vanishing with the activity when the transition occurs, at $t \approx 1.4$ s (red dashed line). Also, it is noted that ECE channels outside the core do not show the fluctuation evolution.

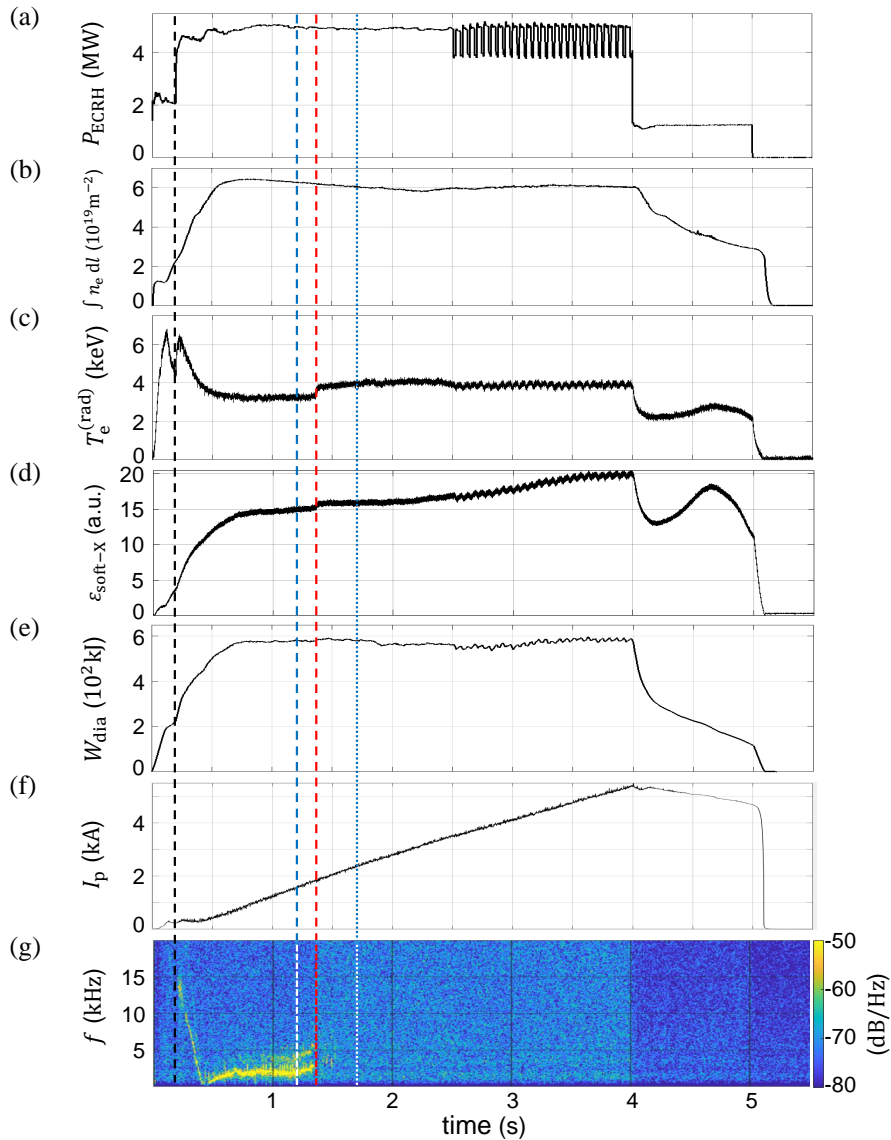


Figure 1. Waveform signals taken in low-iota configuration plasma discharge 20180829.24 in W7-X (configuration B: DBM, $\langle\beta\rangle = 1.02\%$). (a) shows the electron cyclotron heating power P_{ECRH} , (b) the line integrated electron density n_e , (c) the ECE signal measured through channel-#13 with predominant central emissions, (d) soft-X ray emission $\varepsilon_{\text{soft-X}}$ with highest signal contribution from the high gradient region, (e) the diamagnetic energy W_{dia} and (f) the total plasma current I_p . Spectrogram computed through the short-time Fourier transform of the ECE signal obtained through channel-#10, observing the plasma core (g). Red dashed line pinpoints the instant when a spontaneous T_e increase is observed. Blue dashed and dotted lines indicate instances before and after the T_e transition occurs, at $t = 1.2\text{s}$ and $t = 1.7\text{s}$ respectively. Black dashed line illustrates instance when P_{ECRH} was swiftly increased.

The change of the plasma state due to the transition is also evident when comparing radial profiles of main plasma parameters at time windows before and after the transition occurs, Fig. 2. The profiles in Fig. 2(a) – (d) were retrieved from a discharge time

$t = 1.2$ s before the T_e transition took place. Conversely, Fig. 2(e) – (h) present profiles for a time instance after the transition, $t = 1.7$ s. The profiles are presented in a radial coordinate r ($r = 0$ is the plasma center) and the ion and electron profiles are shown in blue and red respectively. To fit the data, a gaussian process was applied using a squared exponential covariance function [19], and its hyperparameters were optimized through maximum marginal likelihood. Also, as an added condition for the fit, the gradients at $r = 0$ are set to be equal to zero.

Comparing Fig. 2(a) with Fig. 2(e) shows a noticeable change in the T_e profile. We observe the higher attained temperatures in the plasma center expanding throughout the high gradient region. However, the total pressure is surprisingly unaffected within the error margins (c.f. Fig. 2(c) and Fig. 2(g)); In other words, the increase in T_e appears to happen in an adiabatic process for the plasma as a whole and the plasma densities in Fig. 2(b) and Fig. 2(f), rearrange such that the thermal energy is conserved. Further evidence is provided by the line integrated soft-X ray emissivities which show a spatio-temporal pattern indicating locally decreasing and increasing n_e [4]. After the transition, the densities of both, electrons and ions, decrease slightly near the core (c.f. Fig. 2(b) and Fig. 2(f)). Also, the E_r profiles calculated from the ambipolarity condition change significantly, namely from negative values across the radial coordinate as seen in Fig. 2(d), to positive values near the plasma core after the transition occurs, Fig. 2(h). It is this feature of $E_r > 0$ that provides along with the increase of T_e the evidence for a transition to an electron-root confinement to occur.

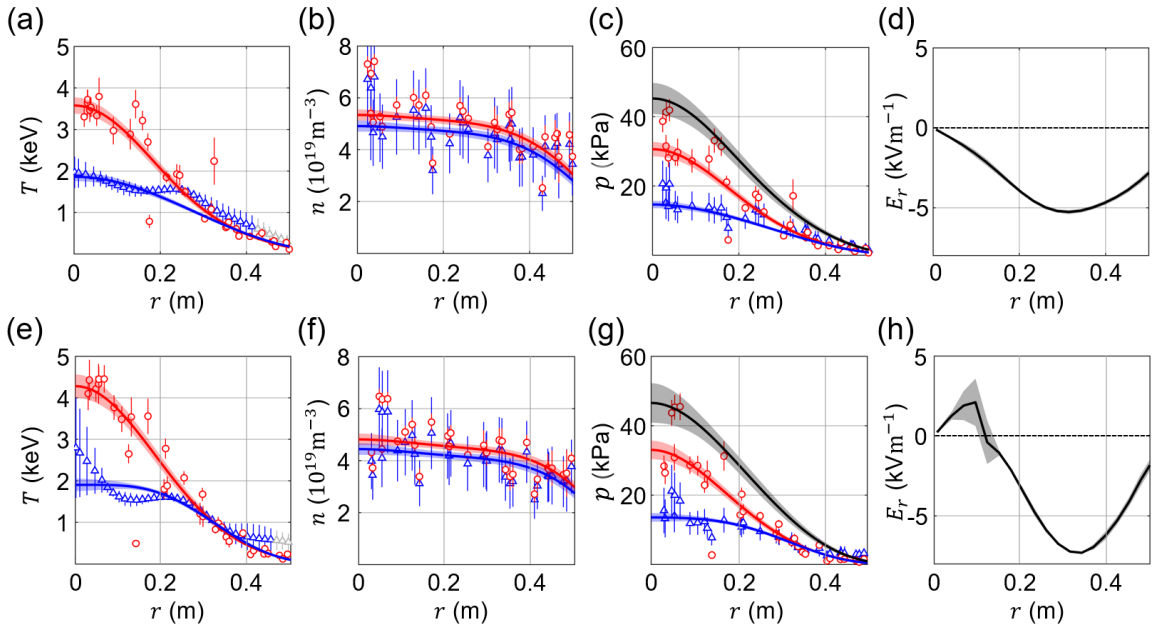


Figure 2. Plasma profiles of low-iota configuration plasma discharge 20180829.24 in W7-X at discharge times (a) – (d) $t = 1.2$ s and (e) – (h) $t = 1.7$ s. Electron (red) and ion (blue) temperature profiles (a),(e); density profiles (b),(f); plasma pressure profiles (c),(g) including total plasma pressure (black line); and radial electric field profiles (d),(h).

Given the profiles as shown in Fig. 2, we are in the position to provide estimates of the time-dependent evolution of the current density profiles. The evolution of the parallel current density $j_{\parallel}(r)$ is key to assess potential changes in the rotational transform $t(r)$ over time. To this end, we employ the neoclassical transport code NTSS [20]. The code delivers the shielding current profile evolution for a given set of temperature and density profiles. NTSS solves the time-dependent particle and energy flux equations in flux coordinates. The radial electric field is self-consistently determined from the non-ambipolar electron and ion fluxes with a field-diffusion model to cope with bifurcations of non-single valued solutions of the ambipolarity condition [21]. The latter may lead to the occurrence of electron-root and ion-root solutions as seen in Fig. 2(d) and (h), respectively. The evolution of the poloidal flux provides the parallel current density profile in response to the bootstrap current (and current drive, found to be negligible with the almost perfect streaming angle in the analyzed experiments).

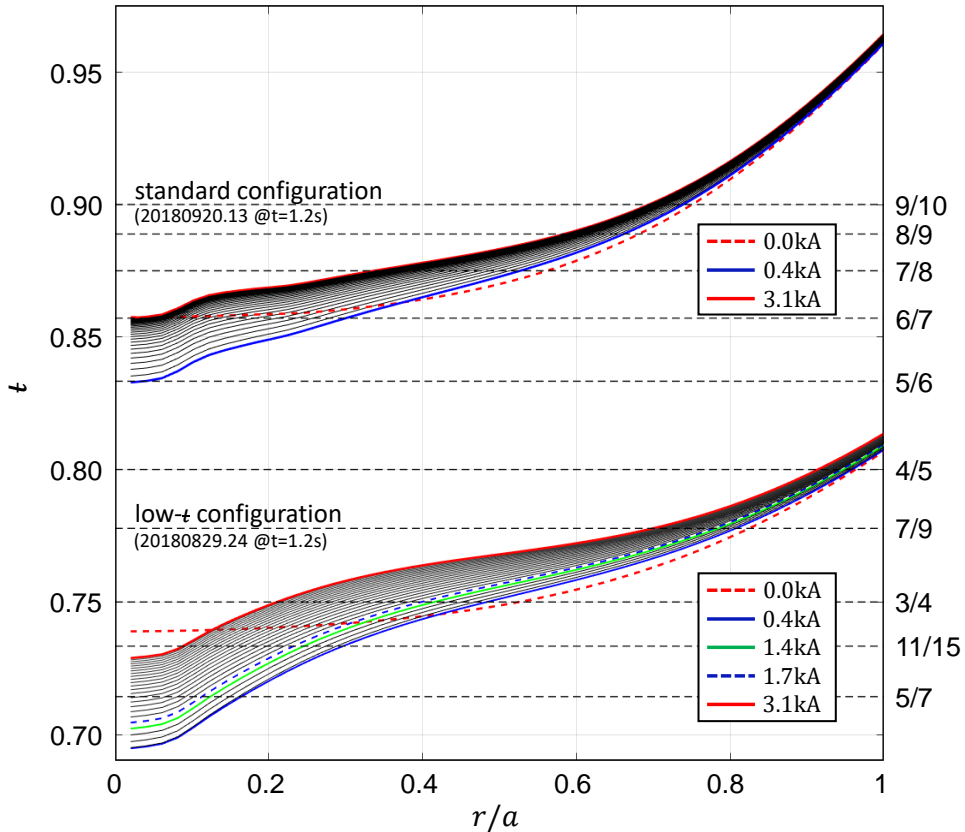


Figure 3. Evolution of rotational transform profiles for increasing (up to 3.1 kA) net toroidal current in plasma discharge 20180920.13 (standard configuration) and plasma discharge 20180829.24 (low- t configuration) in W7-X. Calculated employing the transport code NTSS [20]. Several low-order rationals are also indicated.

Since the experimental findings indicate that the fluctuation profile ceases after some seconds, we conclude that a detailed simulation on short time-scales (plasma start-up time, energy confinement time) is not required but imposes challenges for time-

dependent, self-consistent simulations. Instead, we use the profiles in Fig. 2(a)-(c) as given for some initial simulation time t_0 . We neglect profile changes and any difference needs to lie within the profiles Fig. 2(a)-(c) compared to Fig. 2(e)-(f) after the transition of T_e took place.

Fig. 3 shows the outcome of $j_{||}(t)$ simulations in effect on the Δt profiles changing from the poloidal flux of $j_{||}$ following the methodology described in [20]. For comparison purposes, the rotational transform profiles of two discharges with similar plasma profiles but in different magnetic configurations are shown. More specifically, plasma discharges 20180829.24 and 20180920.13 in the low- ι configuration and in the standard configuration respectively. For both cases, it is seen that the rotational transform without plasma (vacuum ι , red) is distorted by $j_{||}$. Since the initial conditions of the simulations impose an instantaneous response, ι is distorted strongly for the first time step but relaxes to a stationary ι -profile. Fig. 3 also reveals that the relaxation of the ι -profiles takes place on an evolution in the time-scale of the L/R time $\tau_{L/R}$ which is given by the inductivity of the plasma and the resistance. The NTSS code calculates this figure and for the profiles shown in Fig. 2, $\tau_{L/R} \approx 11.9 \pm 1.0$ s for Fig. 2(a)-(d) and $\tau_{L/R} \approx 14.5 \pm 1.1$ s for Fig. 2(e)-(h).

Since the evolution takes place on $\tau_{L/R}$, Fig. 3 indicates the ι -profiles to cross rational values at different r over time. In other words: rational values of ι are moving at different locations of T_e and $\partial T/\partial r$, both of which decisively affect the electron particle thermodiffusion which is the main reason for changes in the ambipolarity condition that sets E_r . The rational surfaces 5/6 and 5/7 are important because these are candidates in which magnetic island chains are produced owing to the $N = 5$ periodicity in W7-X [22]. We note that, with a plasma current of 0.4 kA (blue line), the rotational transform in the standard configuration barely crosses the 5/6 rational surface. However, with the same value of the plasma current, the rotational transform in the low- ι configuration crosses the 5/7 low-order rational surface at $\approx r/a = 0.17$ and this crossing moves inwards up to $\approx r/a = 0.1$ until the plasma current reaches 1.7 kA (blue dashed line) at which the T_e transition occurs. The experimental observations and the simulations allow us to conclude, that, as observed on H-J and TJ-II, it is the slowly changing ι profile that triggers the transition to an electron-root transport regime with a radial electric field bifurcating in the core region from negative to positive values as seen in Fig. 2(d) and Fig. 2(h).

3. Characterizing fluctuation activity preceding T_e transition

Now, we characterize the fluctuation activity before the transition to electron-root confinement to narrow down potential modes. This is done by different methods from both, experimental and numerical approaches. It is imperative to gain as much insight on the activity as possible from the experiment itself, before moving on to the numerical modeling. That is, to optimally utilize the available computing resources, analyzing only the most promising candidates suggested by the experimental results.

To this end, we first inspect the dependency between the mode frequency and the main plasma parameters, second we analyze spatio-temporal fluctuation measurements, third we examine soft-X ray tomography results, fourth we perform ideal MHD stability studies, fifth we analyze the impact of magnetic islands and E_r on the Alfvén and sound continuum, and finally we perform fluid and fully gyrokinetic simulations.

3.1. Potential modes and their distinctive characteristics

First, we provide an overview of potential modes known to occur in stellarator plasmas including their dispersion relation as well as the methods employed in Tab. 1. We begin with a recapitulation of known MHD activities and those dependencies that allow one an identification. A specific focus is put on spatial variations with respect to observations explained in the subsequent section.

Table 1. Overview of known MHD instabilities with their respective dispersion relations and methods employed to identify them. The reference points to the specific methodological approach applied in this paper

MHD instability	Dispersion relation	Methods for identification
Alfvén wave	$\omega_A^2 = k_{\parallel}^2 v_A^2 \rightarrow f = B(n - \iota m) 2\pi R (\mu_0 n_i m_i)^{\frac{1}{2}} \propto \frac{1}{\sqrt{n_i}}$	Parameter dependency: f v.s. T and f v.s. n
Ion acoustic wave	$\omega_s^2 = k_{\parallel}^2 v_s^2 \rightarrow f = \frac{(n - \iota m)}{2\pi R} \left(\frac{k_B (\gamma_e T_e + \gamma_i T_i)}{m_i} \right)^{\frac{1}{2}} \propto \sqrt{T}$	Alfvén/sound-continuum: global MHD with CAS3D and CONTI [23–25]
Geodesic acoustic mode (GAM)	$\omega_{\text{GAM}}^2 = \frac{2v_s^2}{R^2} \left(1 + \frac{\iota^2}{8\pi^2} \right) \rightarrow f \approx \frac{1}{2\pi R} \left(\frac{2k_B (\gamma_e T_e + \gamma_i T_i)}{m_i} \right)^{\frac{1}{2}} \left(1 + \frac{\iota^2}{8\pi^2} \right) \propto \sqrt{T}$	Fluid model: non-ideal including uniform resistivity, electron inertia and viscosity [26–28]
Low frequency oscillation	$\omega_{\text{LFO}} \sim \frac{v_{d,i} \cdot \nabla \Psi}{v_{d,i} \cdot \nabla \Phi} \frac{\sqrt{k_B T_i / m_i}}{R}$	Gyrokinetic model: Electromagnetic gyrokinetics for fast ions and bulk ions and electrons [29, 30]

An Alfvén wave is a traveling oscillation of ions in response to a restoring force provided by an effective tension on the magnetic field lines [31, 32]. It propagates in the direction of the magnetic field \mathbf{B} , while the ions motion and the perturbation of the magnetic field travel transversely. The dispersion relation as presented in Table.1 is derived from the resolution of the linearized ideal MHD equations [33]. If we assume the perturbed electrostatic potential to have the form $\Phi \sim \exp(-i\omega t + i(n\phi - m\theta))$, the parallel wave vector k_{\parallel} for a mode with fixed poloidal and toroidal mode numbers, m and n respectively, depends on the radially dependent ι profile. Also, the Alfvén velocity v_A is a function of n_i and \mathbf{B} , both of which with spatial variations, thus resulting in a space dependent dispersion relation. This means that for each m and n , a continuous spectrum of modes in radial direction exists with a mode frequency also dependent on

the spatial location [34]. Hence, for a set of modes with fixed m and n , the Alfvén continuum can be calculated to scrutinize if an Alfvén wave could exist at the observed frequency. Additionally, to determine if the fluctuation activity we detected is an Alfvén wave, the dependency $f_{\text{peak}} \propto 1/\sqrt{n_i}$ can be verified.

Ion acoustic waves are longitudinal oscillations of ions and electrons in a plasma that can occur through the interaction with an electric field. These constitute a fundamental mode of ion dynamics in which ions oscillate slowly against the background of rapidly oscillating electrons that provide the necessary restoring force [35, 36] and the dispersion relation can be derived from the ion fluid equation [33]. Similar to the Alfvén waves, the frequency of the ion acoustic waves does also vary spatially, thus forming a continuous spectrum of modes for fixed values of m and n . Thus, the indicatives to determine if the fluctuation activity is an ion acoustic wave are the parameter dependency $f_{\text{peak}} \propto \sqrt{T}$ and the possible waves appearing in the sound continuum.

Zonal flows are a particular case of sheared flows caused by an electrostatic potential perturbation that play an important role in the reduction of turbulent transport. These are characterized by zero wavenumber in the plasma potential while they have a finite radial wavelength [37, 38]. The collisionless evolution of initial zonal flow perturbations can be divided into two branches, the high-frequency branch constituted by geodesic acoustic modes (GAM) and the low-frequency branch comprised by low frequency oscillations. Ion orbits are polarizable, meaning that their guiding center can be displaced in the direction of an applied radial electric field E_r . This displacement leads to polarization and furthermore to the counteracting of E_r , thus giving rise to geodesic acoustic modes. These oscillations are electrostatic potential fluctuations with finite radial wavenumber that are induced by the geodesic curvature of the magnetic field line coupled to the poloidal density perturbation [39]. This electroacoustic mode leads to plasma motion in the magnetic surfaces perpendicular to the field, it is associated with the surface component of the magnetic field line curvature and it involves a $m = 1$ pressure disturbance.

In addition to geodesic acoustic modes as observed in tokamaks and stellarators [40], the presence of locally trapped particles in stellarators leads to an additional effect. If a radial electric field is applied, particles drift radially either gaining or losing energy from the field, affecting their respective drift velocity v_d . For a radial electric field pointing outwards, the outward drifting ions gain energy whereas the inward drifting ions lose energy (vice versa for the electrons). Thus, given that v_d is proportional to the particle velocity squared, the speed of the outward drifting ions increases over time while the inward drifting ions slow down. This results in a net toroidal current. The plasma acts as a dielectric becoming polarized, partly shielding out the applied radial electric field, which prompts an oscillatory response [41, 42]. The frequency of this oscillatory response, which is referred to as low-frequency oscillation in the literature [37, 40], can be written in terms of the ion magnetic drift $v_{d,i}$, the ion thermal velocity $v_{t,i}$, a radial coordinate Ψ and the major radius R [43].

Numerical modeling of this multifaceted MHD instabilities offers valuable insight

on the plausible scenarios that may develop from specific discharge conditions. For example, ideal MHD stability studies can determine if magnetic equilibria are stable against ideal MHD perturbations and thus determine if any perturbations of this kind is susceptible to grow unstable. To consider non-ideal perturbations, more intricate models that include e.g. resistivity, electron inertia and viscosity between others are required. More comprehensive models however, require thorough (yet more computationally demanding) models such as a gyrokinetics. Stepwise involvement of these aspects encompassing electromagnetic gyrokinetics for electrons and fast and bulk ions could offer more insight to prove whether an observed fluctuation corresponds to a zonal flow. Therefore, verifying the frequency and radial location of the observed activity to match with a plausible mode in the models is the followed approach in this study. The models employed in this paper are described in more detail in section 3.3.

3.2. Experimental approach

In this section, measurements from the different plasma parameters are analyzed to gain insight on the distinct characteristics of the fluctuation activity observed to be able to discern between the potential modes presented in the previous section. More specifically, the aim of the experimental approach is two-fold: in the one hand, to unravel any dependency between the frequency of the activity and the plasma parameters and, in the other hand, to characterize the activity as thoroughly as possible to discriminate between the plausible modes obtained through the numerical models in section 3.3.

3.2.1. Mode frequency and plasma parameter dependency The evolution of the frequency f_{peak} of the fluctuation activity w.r.t. central values of different plasma parameters is depicted in Fig. 4. Data from eight plasma discharges with the same magnetic configuration, in which the transition was observed, are displayed.

The variation of f_{peak} versus the central electron density n_e^0 is illustrated in Fig. 4(a). We can identify two clusters of discharges, namely four with $n_e^0 \approx 3 \times 10^{19} \text{ m}^{-3}$ and the remaining four with $n_e^0 \approx 4.7 \times 10^{19} \text{ m}^{-3}$. The frequencies found in both subgroups lie between 2 kHz and 6 kHz and fluctuate by $\approx 1 - 2$ kHz on average. This wide range of frequencies is observed even when the densities do not vary significantly, thus no clear overall parameter dependency is found.

The variation of f_{peak} w.r.t. the central electron temperature T_e^0 is depicted in Fig. 4(b). It can be seen that the subgroups lie closer to each other in terms of the electron temperature. We note a similar behavior of f_{peak} as recognized previously, that is, a fluctuating frequency for roughly constant values of the plasma parameter in question (T_e^0). However, plasma discharges 20180829.33/34 depicted in green and purple respectively, present a broader scattering of frequency values for varying T_e^0 ($\approx 0.2 \text{ keV}$). Moreover, a positive correlation between the temperature and the frequency might be recognized for some discharges. Nevertheless, this observation does not hold true in general for the rest of the discharges analyzed.

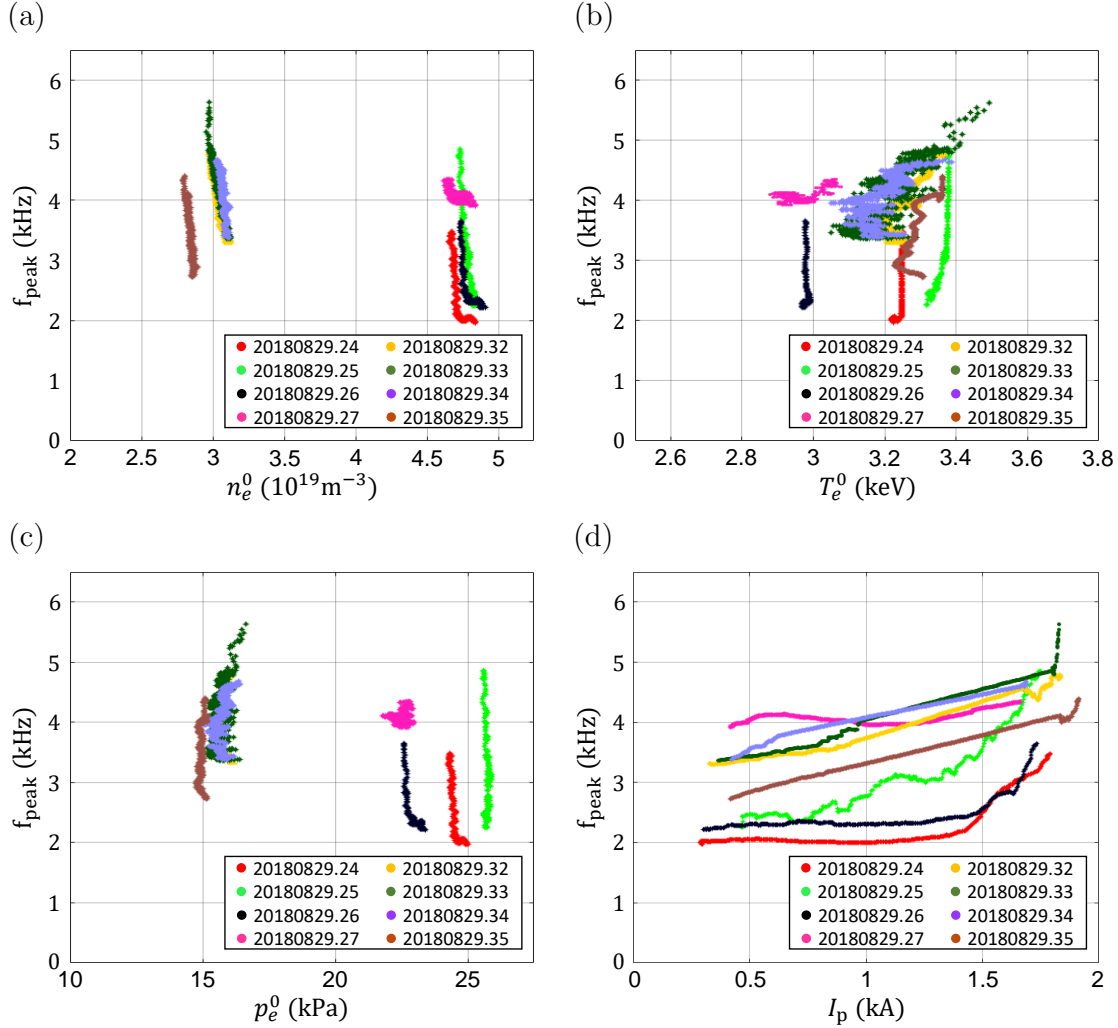


Figure 4. Evolution of the frequency f_{peak} of the fluctuation activity w.r.t. central values of different plasma parameters, in plasma discharges where the transition was observed. More specifically, variation of f_{peak} against (a) electron density n_e^0 , (b) electron temperature T_e^0 , (c) electron pressure p_e^0 and (d) plasma current I_p .

Now, the variation of f_{peak} w.r.t. the central electron pressure p_e^0 is shown in Fig. 4(c). These results are qualitatively comparable with the results presented in Fig. 4(a), where the two clusters can be distinguished and the frequency fluctuates despite, in this case, the electron pressure remains roughly constant. Thus, the electron pressure (electron gradient) is an evident driving force.

As a last parameter in this overview, the variation of f_{peak} versus the toroidal plasma current I_p is presented in Fig. 4(d). For almost all discharges analyzed, a positive correlation between f_{peak} and I_p is observed. This might not be the case for plasma discharge 20180829.27 as illustrated in pink, given the slight decrease of f_{peak} before reaching $I_p \approx 1$ kA. For the other discharges, the frequency rises roughly monotonically along I_p . However, the shape of the evolution of f_{peak} w.r.t. I_p varies from discharge to discharge. E.g., almost a linear correlation between f_{peak} and I_p can be observed for

discharges 20180829.32/33/35 (yellow, dark green and brown respectively), whereas for discharges 20180829.24/26 (red and black) f_{peak} remains constant until $I_p \approx 1.5$ kA at which the frequency increases rapidly by ≈ 2 kHz. It is noteworthy, that the preceding fluctuation activity vanishes in all discharges for similar values of the plasma current ($I_p \approx 1.7$ kA), independently of the values of the other plasma parameters investigated.

3.2.2. Spatio-temporal fluctuation analysis MHD instabilities are perturbations of the plasma that can be considered as electromagnetic waves interacting with plasma particles [44]. These are characterized by a plasma displacement ξ and by perturbed electric and magnetic fields associated with ξ . The displacement at a given radial location r and time t can be approximated by $\xi_{r,t} = \frac{T_e(r,t) - \langle T_e(r) \rangle}{\nabla \langle T_e(r) \rangle}$ [45], depending on T_e fluctuations $\tilde{T}_e = T_e - \langle T_e \rangle$ and gradients. In this sense, $\xi_{r,t}$ illustrates the direction and spatial extent to which T_e is squeezed and, since T_e is assumed to be constant on flux surfaces, magnetic flux compression is characterized, which is expected in the presence of a magnetic island. For a straightforward interpretation, we will consider the absolute value of $\nabla \langle T_e(r) \rangle$, such that independently of the magnetic field side, positive $\xi_{r,t}$ denotes a fluctuation attaining higher T_e values, whereas negative $\xi_{r,t}$ correspond to lower T_e . This analysis can give insight on the radial location of the instability, as well as deliver information regarding the evenness of the poloidal mode number m and hint the presence of a magnetic island.

The $T_e - \langle T_e \rangle$ and ∇T_e required for the displacement analysis employing data retrieved through the ECE diagnostic in plasma discharge 20180829.24 is presented in Fig. 5. In Fig. 5(a), the fluctuation activity preceding the T_e transition can be seen from measurements obtained through two ECE signal channels that collected incoming radiation originating from the low-field side (positive r/a) of the plasma. Although the oscillations detected in channel-#10 are stronger in amplitude, we observe these oscillations to have similar frequencies ($f \approx 2$ kHz) and to be phase shifted by π . From ECE measurements, we calculated the T_e profile (blue) as illustrated in Fig. 5(b). This profile was derived from averaging spatio-temporal ECE measurements over a time window of 40 ms. The sudden drop in the profile near the core is an artifact due to an ECE channel measuring emission at a frequency near the ECRH frequency. We note this profile to roughly match the predicted T_e profile (black) calculated through the 3-D ray tracing code TRAVIS [46]. This code solves the radiative transfer equations, allowing one to derive local electron temperatures from microwave emissivity taking radiation transport and relativistic effects into account. From this predicted profile, a T_e gradient profile can be derived, Fig. 5(c). From this analysis, all required quantities for the determination of the displacement $\xi_{r,t}$ are acquired.

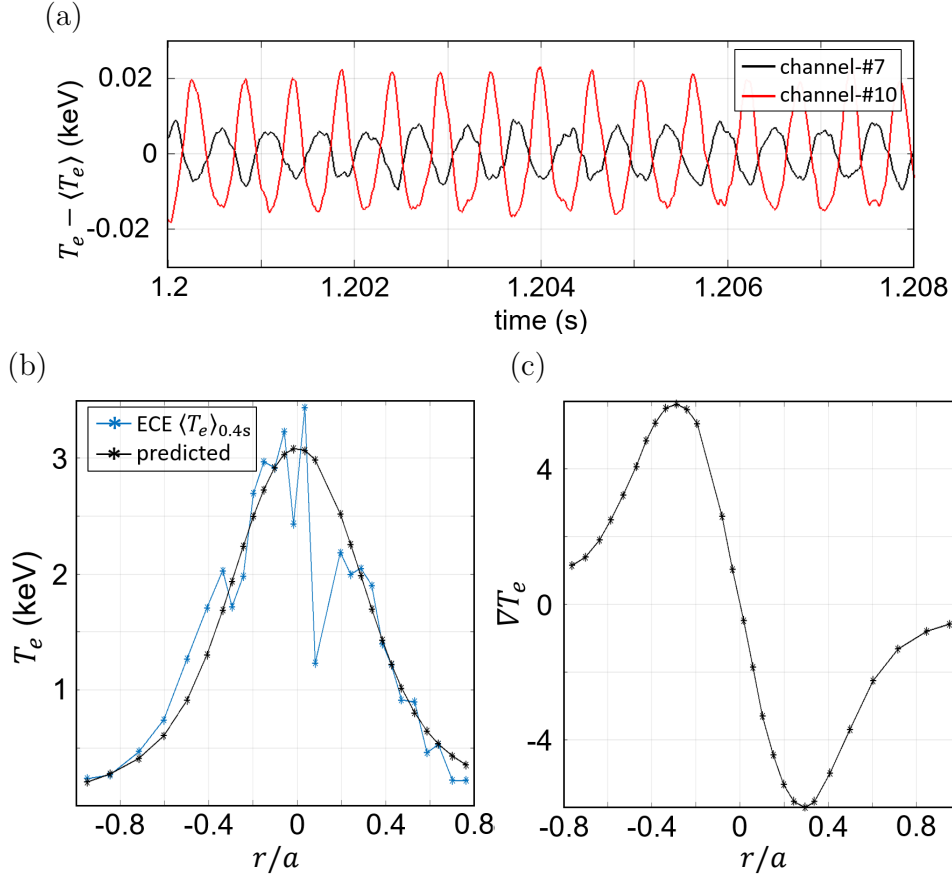


Figure 5. Analysis of ECE measurements for the determination of magnetic surface perturbations in plasma discharge 20180829.24 in W7-X. (a) fluctuation activity preceding T_e transition measured through ECE signal channels #7 and #10, measuring radiation originating from the low-field side at $r/a = 0.34$ and $r/a = 0.20$. (b) T_e profiles obtained from spatio-temporal averaged ECE measurements (blue) and as predicted through the ray-tracing code TRAVIS (black). (c) Temperature gradient profile derived from the profile calculated with TRAVIS.

The approximation of $\xi_{r,t}$ at different radial positions r/a at $t = 1.2$ s is shown in Fig. 6(a). The blue markers represent the value of $\xi_{r,t}$ corresponding to each available ECE signal channel and the gray shaded regions depict error bands obtained by averaging the value of $\xi_{r,t}$ at 100 different time windows, between $t = 1.200$ s and $t = 1.201$ s. From the error bands, we note that this method does not deliver conclusive information in the outer regions of the plasma and in the very core. However, significant structures appear between roughly $r/a = 0.2$ and $r/a = 0.5$ in both field sides of the plasma.

The conducted displacement analysis clearly localizes T_e oscillations in the high-gradient region in the plasma core at $r/a = 0.25$. Moreover, these $\xi_{r,t}$ structures appear to be mirrored seen from the comparison of the structures in the high-field side (negative r/a , black line) and in the low-field side (positive r/a , black dashed line). This occurs at around a normalized effective minor radius $r/a = |0.25|$. The

displacement oscillates once in each field side, which is a $\xi_{r,t}$ structure that a magnetic island could cause [44]. Magnetic islands squeeze their surrounding magnetic surfaces in both radial directions, towards and away from the plasma center, leading respectively to some decrease and increase of T_e in the corresponding directions. Therefore, the oscillation of the displacement obtained from the analysis hints on the presence of a magnetic island centered at $r/a = 0.25$ with a width of ≈ 6 cm.

Now, a phase analysis between all ECE signal channels w.r.t. ECE channel-#10 is shown in Fig. 6(b). Focusing on the phase analysis results for the ECE signal channels that presented significant $\xi_{r,t}$ results ($|r/a| \in [0.2, 0.5]$), we observe that the mirrored structures are in phase with each other. This is an indication of an even poloidal mode number m .

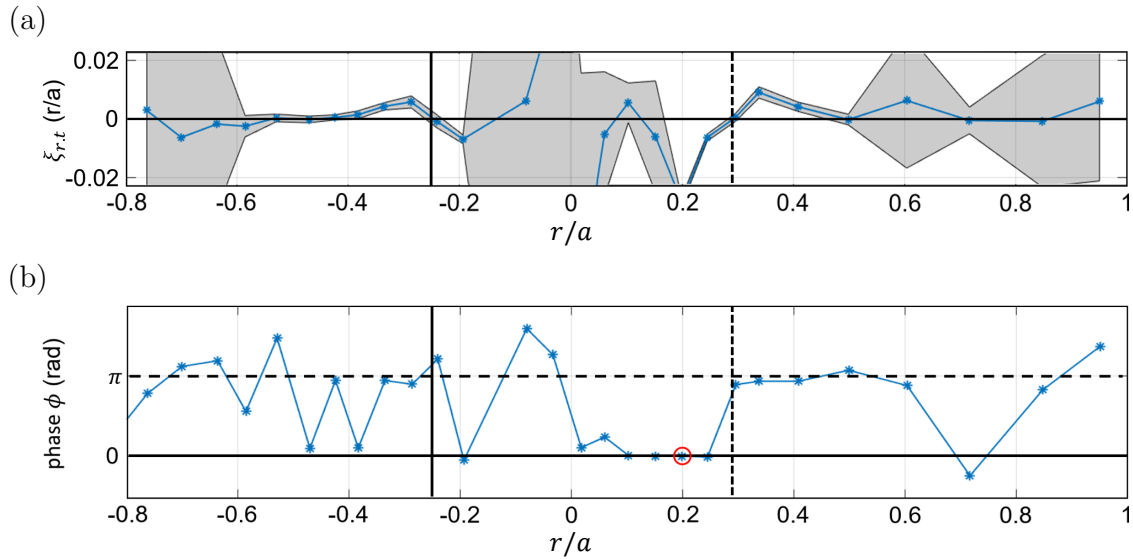


Figure 6. Analysis of magnetic surface perturbation due to fluctuation activity in plasma discharge 20180829.24 in W7-X. Black vertical dashed and solid lines indicate radial location of $\xi_{r,t} = 0$ in the low- and high-field side respectively. (a) Displacement $\xi_{r,t} = \frac{T_e(r;t) - \langle T_e(r) \rangle}{|\nabla \langle T_e(r) \rangle|}$ calculated from ECE measurements and derived T_e profiles. (b) Phase analysis of spatio-temporal ECE data w.r.t. ECE signal channel-#10 (red circle).

3.2.3. Soft-X ray tomography To complement the ECE displacement analysis, soft X-ray multi-camera tomography system was used to perform 2-D poloidal tomographic reconstructions. The reconstruction may offer additional insight on the fluctuation activity preceding the transition regarding the poloidal mode number m .

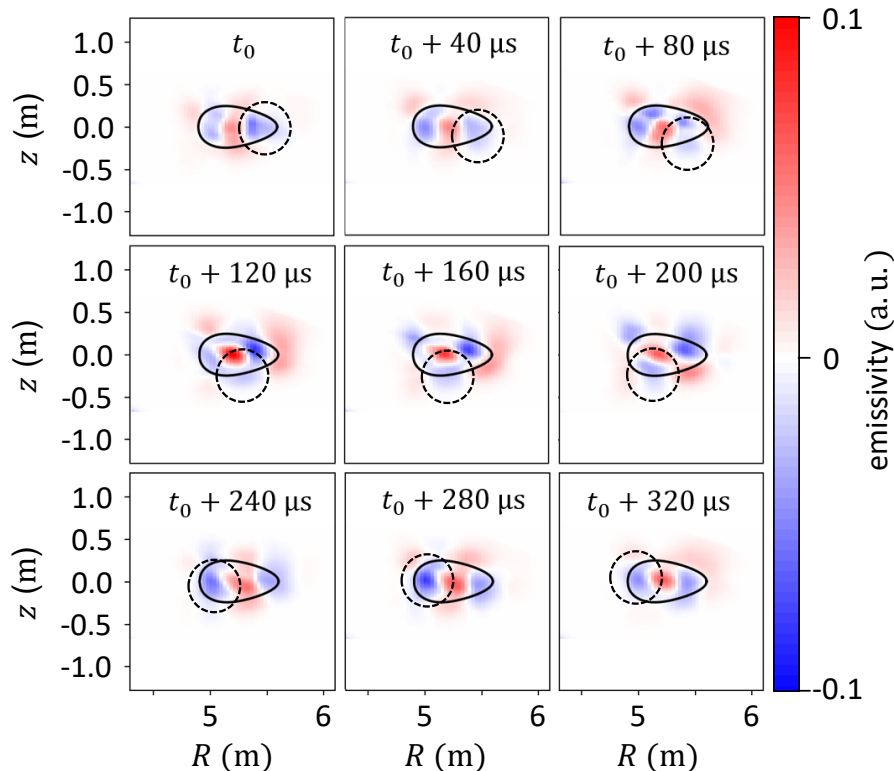


Figure 7. SVD-filtered soft-X ray tomographic reconstruction of plasma discharge 20180829.24 starting at $t_0 = 1.17$ s displaying rotating MHD structures in a poloidal cross-section in W7-X. The relative change of the emissivity w.r.t. an averaged emissivity reference is depicted from blue to red. A flux surface in the gradient region is illustrated in black.

The tomographic reconstructions of soft-X ray emissivity data at $t = 1.17$ s are shown in Fig. 7. A singular value decomposition (SVD) is employed to subtract a reference distribution representing the time averaged emissivity in a stationary phase from the emissivity at each region in the poloidal plane. In the reconstructions, regions of stronger and weaker emissions are depicted, therefore Fig. 7 shows the fluctuating signal. As seen from the sequence in Fig. 7, the evolution of the tomographic reconstructions with a time step of $40 \mu\text{s}$ shows a clock-wise rotating structure (encircled by a dashed line) with an approximate frequency of 2 kHz and dominating 2 and $m = 3$ structures. Higher mode numbers cannot be excluded from this analysis but we take this finding to focus on low- m modes.

3.3. Numerical approach

Finally, with all the information gathered for the characterization of the preceding fluctuation activity from the experimental approach, the numerical approach can be explored. Summarizing the experimental findings in the previous section we confront the models in Tab.1 with the experimental results. That is an oscillation at approximately 2 – 3 kHz not showing a clear parameter dependence with relatively low poloidal mode

number ($0 \leq m \leq 4$ from XMCTS) and probably even (from the plasma displacement analysis), as well as unknown toroidal mode number n . Their radial location was found to reside in a region of roughly 6 cm around a normalized effective minor radius $r/a \sim 0.25$. We will perform a differential diagnosis invoking different theoretical models using magnetic equilibria reconstructed to meet the experimental conditions as good as possible.

For the modeling, we will consider two cases for plasma discharge 20180829.24, namely: Case A, using the profile values calculated with the transport code NTSS at $t = 1.2$ s and the rotational transform profile at $t = 0$ s (vacuum t shown in red in Fig. 3); and Case B, using the same profiles for density and temperature and a profile of the rotational transform which corresponds to a total current of 1.4 kA (depicted in green in Fig. 3). The total current at which the transitions occurred ranged between 1.6 – 1.8 kA. The comparison between the two cases will allow us to draw conclusions about the role of the rotational transform on the fluctuation activity. Also, the effect of the radial electric field and hypothetical magnetic islands located at rational surfaces near the observed oscillations will be explored. In this section, the methods employed to analyze both cases are presented and followed by the respective results.

3.3.1. Tools employed for modeling Ideal MHD stability studies are a first step modeling analysis since these can offer insight on the stability of plasma equilibria, particularly against ideal MHD perturbations. The equilibrium calculations are performed implementing the 3-D MHD code VMEC [47] which employs a variational method to determine the equilibrium state. In the present study, its free-boundary version was used in which the plasma equilibrium is sustained by an external vacuum field and the plasma boundary is simultaneously adjusted for continuous total pressure across it. Then, the finite-element Fourier code CAS3D [23–25] (Code for the Analysis of the MHD Stability of 3-D equilibria) is employed, which is based on a formulation of the ideal MHD energy principle in magnetic coordinates [48]. These calculations also include the t -evolution. A detailed description of the procedure can be found in [49]. It is important to mention that ideal MHD stabilities do not include E_r contributions.

We will explore the stable MHD spectrum for both Alfvén and sound waves, which could be excited or destabilized by an external as well as an internal source such as e.g. turbulence. Calculating the respective continua, that is, the local Alfvén and sound frequencies for each combination of fixed m and n is not trivial for realistic plasma scenarios. This is achieved by first implementing CAS3D for the global MHD calculations and then employing the continuum code CONTI [50] to solve the equations of the ideal MHD continuum on flux surfaces using a Fourier transform in the poloidal and toroidal directions. The effect of magnetic islands on the continuum is currently being investigated [51, 52] and the modification of the spectra due to assumed static islands at resonant values of the rotational transform is also discussed.

For non-ideal MHD modeling including resistivities, electron inertia and viscosity, the particle-in-cell simulation code EUTERPE can be implemented [26, 27]. Here, a

reduced fluid model coupled by field equations is employed. To resolve these equations for electrostatic and magnetic potentials for each mode, ideal Ohm's law and momentum equation are used. This results in Fourier components from the fields as a function of time, radius and toroidal and poloidal angles. Hence, the growth rates of modes with fixed m and n can be computed such that unstable modes can be identified [28]. DMUSIC, a modern signal processing technique allows a radially resolved frequency analysis of the simulated potential for single poloidal Fourier indices [53]. This way we can get more insight into the mode dynamics and damping mechanisms.

Lastly, the code EUTERPE is implemented to solve non-linear gyrokinetic equations for finite β considering an external electric field and we will discuss electrostatic gyro-kinetic simulations of zonal flow oscillations as described in [29, 30], which are a common phenomenon in stellarators and especially in W7-X.

3.3.2. Ideal MHD stability analysis The study is based on the plasma discharge 20180829.24, in which a low- t W7-X variant was used with winding currents of 11.862 kA in the modular coils and 8.9 kA in the planar coils. An overview of the magnetic geometry is given in Fig. 8. In the vacuum field, the volume filled by field lines not being scraped off by the divertor is roughly 30 m^3 , the corresponding enclosed toroidal flux is 2 V s . The effective major and minor radii amount to 5.5 m and 0.525 m, so that the aspect ratio is $R/a = 10.5$.

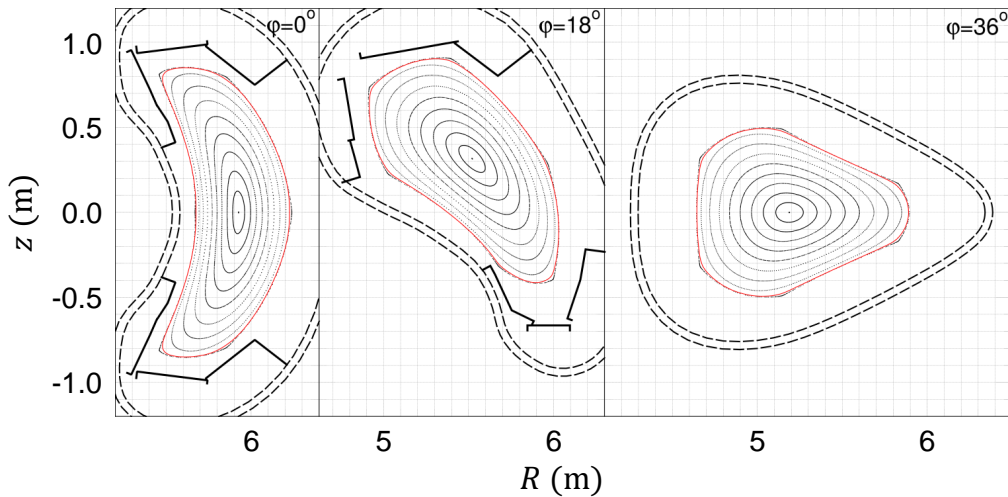


Figure 8. Three characteristic cross-sections showing the magnetic surfaces in the vacuum field (thin dotted lines), the outermost one just not being scraped off by the divertor. The initial boundary for the equilibrium calculation (red), the divertor structures (thick solid black lines), and the first wall (dashed) are also shown. The toroidal angle φ is set to zero for the plane of largest toroidal curvature and $\varphi = \frac{360}{5}/2 = 36^\circ$ in a second symmetry plane within one of the $N = 5$ field periods.

The influence of a small net toroidal current is studied according to the t -profile (green line) in Fig. 3. From the experimental data, the quantities needed for equilibrium

reconstruction were extracted from the profiles presented in Fig. 2. The corresponding current density is concentrated near the magnetic axis, approximating an on-axis ECRH, and lowers the rotational transform to below $\iota = \iota/2\pi = 5/7$ near the magnetic axis. We note that the ι -evolution leads to a shift of the resonance positions, e.g. $\iota = 3/4$ moving from $r/a \approx 0.4$ to $r/a \approx 0.5$. This even leads to a crossing with a new resonate position $\iota = 5/7$ closer to the plasma center. In the outer plasma domain, $r/a \gtrsim 5/6$, the rotational transform is approximately identical to the one resulting for the vacuum case (blue dashed line), with the $5/6$ island used for divertor operation outside the last closed flux surface ($r/a > 1$).

Implementing the energy principle of ideal MHD stability [48], the spectral code delivers results about the temporal and spatial properties of linear MHD modes of general-geometry plasma equilibria. The discrete symmetry of stellarators, i.e. the finite number of identical *field periods*, $N_p = 5$ for W7-X, gives rise to decoupled *mode families* [23] which are the stellarator analogon to the complete decoupling of toroidal mode numbers in axisymmetric systems. In other words, modes with different toroidal mode numbers do not interact or influence each other significantly and thus each mode can be studied independently.

For the present study, all mode families were examined. The Fourier harmonics of the three scalar components of the ideal MHD displacement vector, here 166 for each of them, were chosen to represent large- to medium-scale modes. For the radial dependence, 500 flux intervals between magnetic axis and plasma boundary were used. The boundary condition chosen is that of a plasma surrounded by an infinite vacuum region, so that the perturbation normal displacement, ξ^s , may be finite at the plasma boundary. The energy of the perturbed magnetic field is used for normalization in the stability calculation, facilitating the distinction between stable and unstable plasma equilibria [54]. At present, the influence of a radial electric field, corresponding to a poloidal plasma rotation, is neglected, but can, in principle, be studied with the CAS3D code [55].

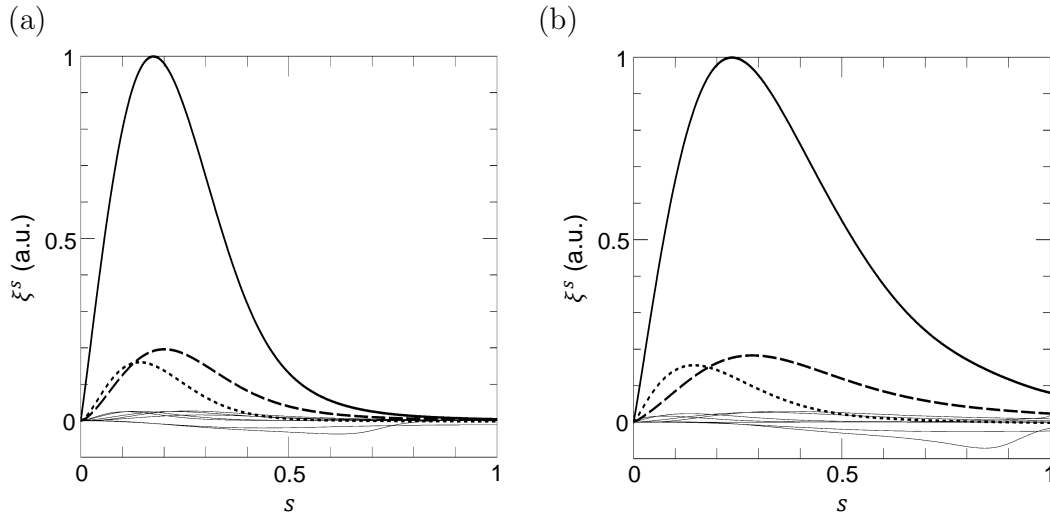


Figure 9. Normal displacement harmonics ξ_{mn}^s of stable ideal MHD modes versus the normalized toroidal flux $s = (r/a)^2$. Only the ten strongest of a total of 166 ξ^s harmonics are shown. (a) Case A, strongest harmonic (thick solid line) has $(m, n) = (8, -6)$. (b) Case B, strongest harmonic (thick solid line) has $(m, n) = (4, -3)$. The strongest sidebands are indicated by thick dashed lines. These are $(m, n) = (9, -6)$ and $(m, n) = (7, -6)$ in (a), and $(m, n) = (5, -3)$ and $(m, n) = (3, -3)$ in (b).

Regarding linearized ideal MHD stability, the properties of the two plasma equilibria (Case A and Case B) are very similar as seen in Fig. 9. For the calculation parameters described above, the configurations are found to be stable (no instabilities). The stable modes found are resonant at $t = 3/4$; that is, at $s \approx 0.25$ for Case A and at $s \approx 0.16$ for Case B, as shown in Fig. 9(a) and Fig. 9(b) respectively. With poloidal mode numbers $m = 8$ in Case A and $m = 4$ in Case B, the dominant Fourier harmonics have a broad radial extent. The small amplitudes at the normalized toroidal flux $s = (r/a)^2 = 1$ indicate a weak disturbance of the plasma boundary.

3.3.3. Alfvén and sound waves Ideal MHD stability analysis (see Sec.3.3.2) did not indicate unstable modes. Therefore, we look for suitable frequencies from the stable part of the MHD spectrum. Such oscillations could be driven by an external excitation of the plasma, plasma turbulence or by resonant interaction with particles in the plasma. Especially the latter effect would be better covered by a kinetic theory which we will employ in a later section. However, looking at the MHD spectrum, i.e. the spectra of Alfvén and sound waves allow one to get a quick overview at low computational cost. Here, we focus on the pure Alfvénic and the coupled Alfvén- sound continuum shown in Fig. 10. Although the global modes which are actually interesting were omitted here, there are hints to their appearance from the structure of the continuum. Usually, global modes reside in continuum gaps (minimizing their so-called continuum damping) or above or below shallow maxima or minima of the spectral branches (Global Alfvén eigenmodes or Global sound modes, resp.).

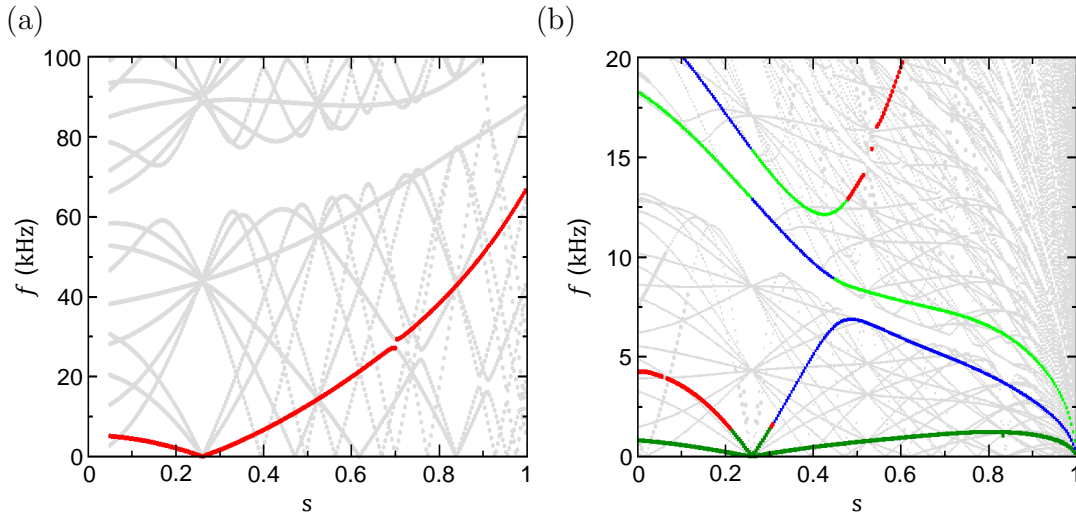


Figure 10. (a) Alfvén continuum for the $N = 2$ mode family. The branch with the mode numbers $(m, n) = (4, -3)$ is highlighted in red. As expected, there are neither open gaps nor shallow extrema allowing for modes in the low frequency region. (b) Lower part of the coupled Alfvén and sound continuum, Relevant continuum branches are highlighted, namely: in red, $(m, n) = (4, -3)$ (Alfvén); in dark green, $(m, n) = (4, -3)$ (sound); in blue, $(m, n) = (3, -3)$ (sound); in green, $(m, n) = (5, -3)$ (sound).

The Alfvén continuum for the $N = 2$ mode family is shown in Fig. 10(a). We observe a gap in the continuum between ~ 60 kHz and ~ 80 kHz where modes might exist. However, there are neither open gaps nor shallow extrema allowing the existence of a weakly damped mode in the low frequency range (~ 2 kHz). The same is the case for the coupled sound and Alfvén spectrum depicted in Fig. 10(b): the open gap is far to high (~ 15 kHz). A global low-frequency sound mode might exist, but due to the Alfvénic $(m, n) = (4, -3)$ branch (dark green), an interaction with the continuum leading to strong damping is highly probable.

If there is no conclusive information on mode numbers, the MHD spectra for all mode families, need to be studied including possibly existing global modes, as it has been done earlier in TJ-II [56]. For the following reasons, this was not done in the present work. First, the modes in question seem neither correspond to a $n_e^{-\frac{1}{2}}$ dependency of Alfvén waves nor the T dependence of sound waves. Second, there are no fast particles that could excite or destabilize Alfvén modes through resonant interactions as in the case of TJ-II. Third, we will perform a gyro-kinetic calculation which will cover kinetic effect more completely, albeit, for a limited selection of mode numbers.

3.3.4. Modification of the Alfvén continuum due to islands The existence of a magnetic island at a resonant position would cause an upshift of the Alfvén continuum [57, 58], which has to be interpreted as the central part of a new gap due to the helicity of the island [52]. In this gap, global modes can be more easily excited as they would undergo less interaction with the continuum and, therefore, experience less damping.

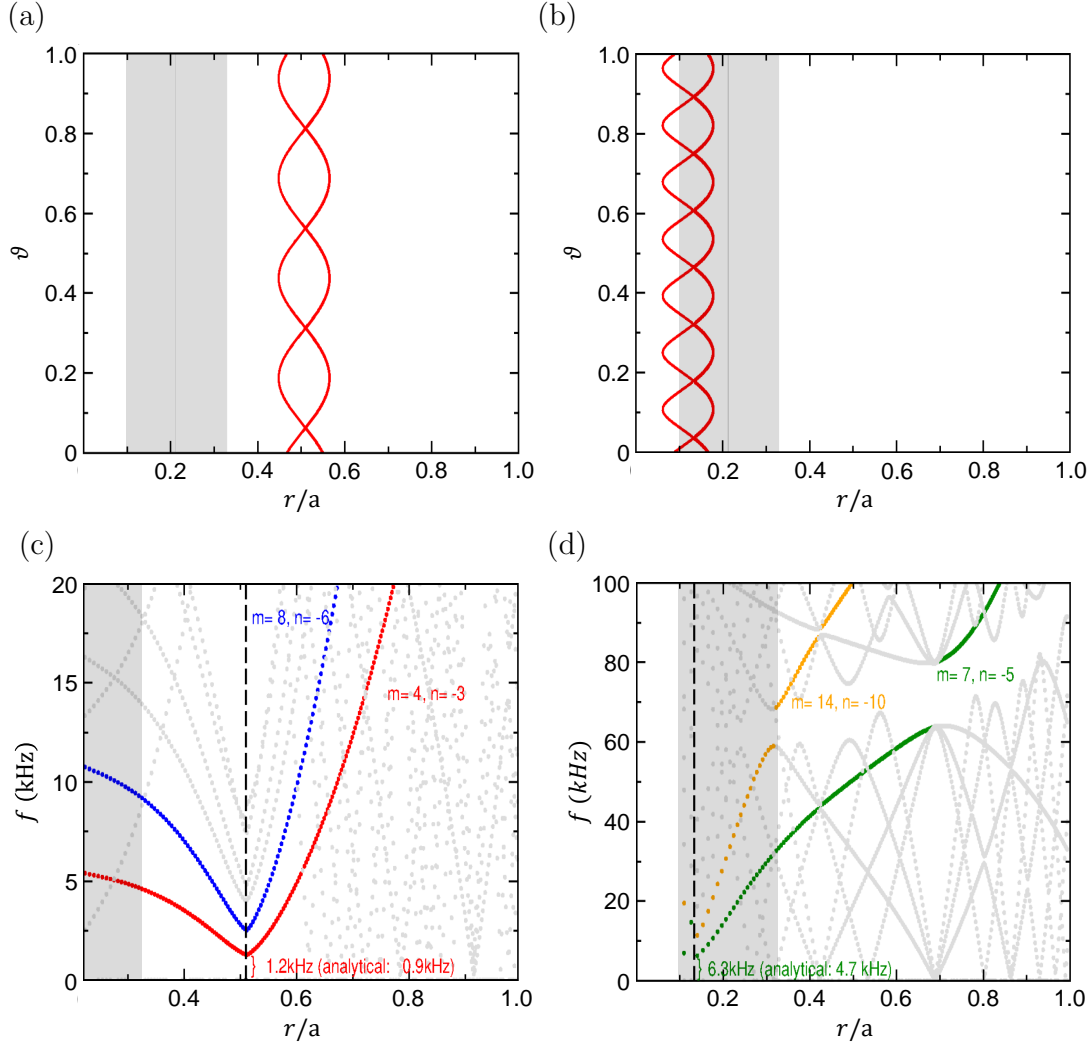


Figure 11. Magnetic island at the resonance position of (a) $t = 3/4$ (Case A) and (b) $t = 5/7$ (Case B). The presumed island width was adapted to the observed ECE signal to match 6 cm and the location of the experimentally observed mode is marked in gray. Alfvén continua (c) and (d) modified due to the presence of the islands shown in (a) and (b) respectively. The continuum frequencies which belong to a certain flux surface s^* (including islands) are assigned to the maximum/minimum position (r/a) of $r_{\max}(s^* = \text{const}, \vartheta, \varphi)$ (see [52]). In (c), the upshift of the $(m, n) = (4, -3)$ branch was measured to be approximately 1.2 kHz, while the analytical formula from Ref, [57] yields 0.9 kHz. In (d), the upshift of the $(m, n) = (7, -5)$ branch was measured to be approximately 6.3 kHz, while the analytical formula yields 4.7 kHz. Gray shaded region indicates location where the fluctuation activity was experimentally observed.

The CONTI code has been used to calculate the modification of the Alfvén continuum of the $N = 2$ mode family due to the presence of a magnetic island. Results are shown in Fig. 11. Judging from the radial extent of the measurement, a presumed island should have the size of approximately 6 cm. Calculations have been done for two possible island locations: one at $t = 3/4$ and the other at $t = 5/7$ as depicted in Fig. 11(a) and (b) respectively. While the first position corresponds to the position

of a lower order rational rotational transform somewhat away from the region of the measurement, the second one is located more towards the center and corresponds to a "natural", i.e. non-symmetry breaking perturbation.

As illustrated on the "outer" part of the the continuum around the island, Fig. 11(a), the frequency for an island excitation at $t = 3/4$ (~ 1.2 kHz) is below the experimentally observed frequency (2 – 3 kHz). Furthermore, such an island would require a symmetry breaking external perturbation.

The other possible island belonging to a symmetry preserving perturbation has been looked at, Fig. 11(b). The resonant iota of $5/7$ is located very close to the plasma center and the frequency of the $(m, n) = (-5, 7)$ branch increases by 6.3 kHz due to the magnetic island. This opens up a frequency window where modes might exist, which would match the observations from the frequency and the radial position of the mode (gray shaded region). Magnetic island induced Alfvén eigenmodes have been calculated only once for a relatively special setting [59]. Their calculation in general is still subject of research. Nevertheless, its mode numbers would be very certainly tied to the island helicity $(m, n) = (7, -5)$. Although the poloidal mode number seems to be a bit to high judging from the XMCTS observations, in principle, it could offer an explanation for the observed frequency.

Further investigations need to reveal if such an island would be possible by engaging e.g. the HINT code [60]. The outcome would depend on subtleties of the equilibrium and its reconstruction and is beyond the scope of this paper.

3.3.5. Mode stability analysis through a gyro-kinetic model As the investigation with ideal MHD did not yield conclusively an instability that could account for the observation, additionally, a fully gyro-kinetic computation has been performed using the EUTERPE code.

We performed two calculations to cover a wide range of mode families as depicted in Fig. 12 and Fig. 13. More specifically, Fig. 12(a) shows the mode stability analysis of the modes related to $(m, n) = (4, -3)$ as depicted in Fig. 12(b), whereas Fig. 13(a) shows the analysis of the modes associated to $(m, n) = (7, -5)$ as illustrated in Fig. 13(b). For each case, the waveforms represent the mode amplitudes for each poloidal mode number m , integrated over all toroidal mode numbers n depicted in their respective mode tableau.

Both calculations were using the electric field from the ambipolarity condition as calculated by NTSS at $t = 1.2$ s (see Fig. 2(d)). The resolution used in radial, poloidal and toroidal directions was 150, 128 and 128 B-splines respectively, and 16×10^6 ions and 64×10^6 electrons markers were employed. In Fig. 12(a) we observe a slight overall steady growth of the modes, which can be attributed to numerical effects. Nevertheless, all cases studied seem to be stable and do not present significant structures. The calculations could be performed for longer times, however it would be computationally expensive and instabilities due to numerics could rise.

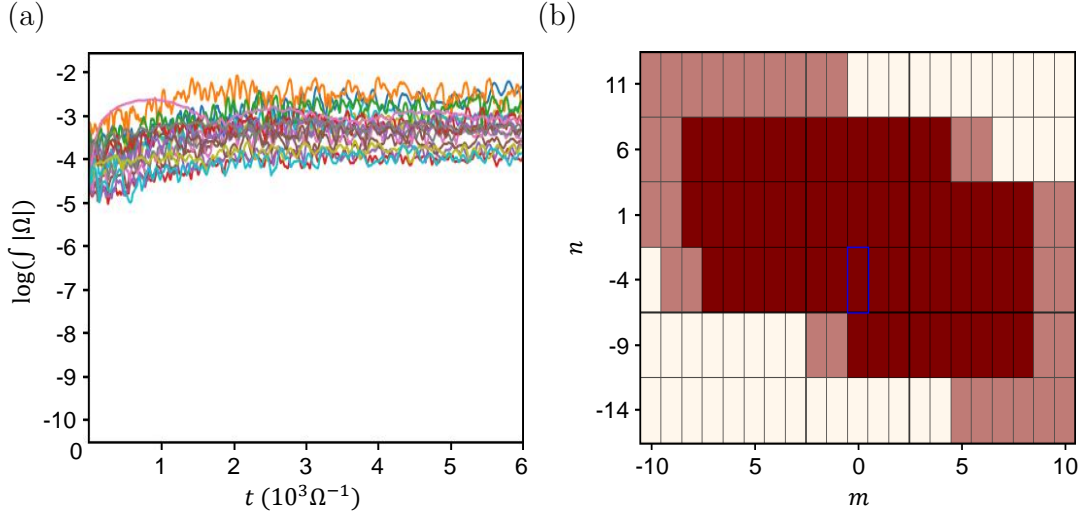


Figure 12. a) Mode amplitudes from a fully gyro-kinetic, electromagnetic calculation integrated over radius and toroidal mode numbers showing no sign of an instability. The calculation was performed for Case A. (b) The mode tableau showing all mode numbers considered for the calculations (dark). A larger tableau (light colors) is needed within the code to account for the broader side bands of A_{\parallel} in Fourier space [61, 62].

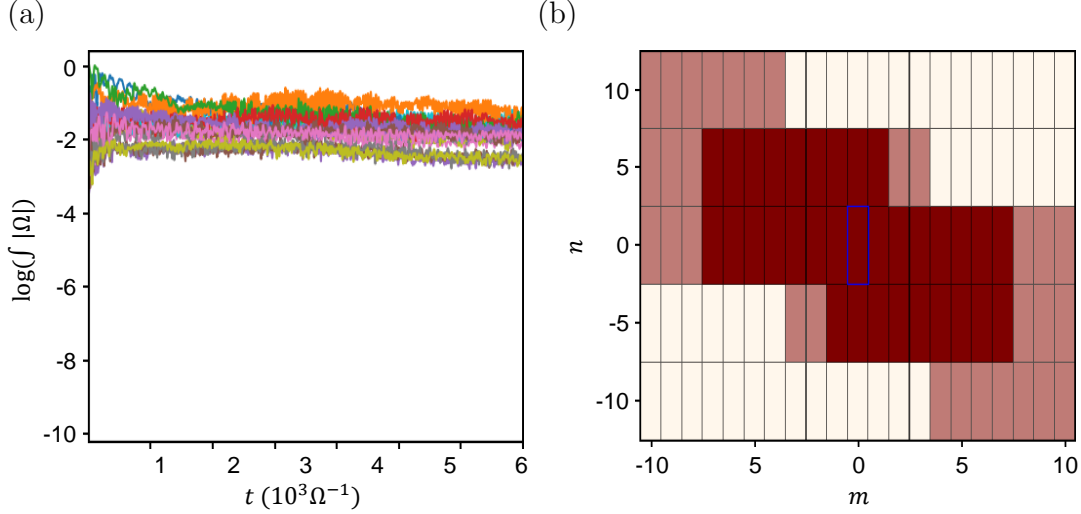


Figure 13. (a) Mode amplitudes from a fully gyro-kinetic, electromagnetic calculation integrated over radius and toroidal mode numbers showing no sign of an instability. The calculation was performed for Case A. (b) The mode tableau showing all mode numbers considered for the calculations (dark). A larger tableau (light colors) is needed within code to account for the broader side bands of A_{\parallel} in Fourier space (see [61, 62]).

3.3.6. Zonal Flow Oscillations In a tokamak equilibrium, a perturbation to the zonal component $\phi_{m=0,n=0}(r)$ of the electrostatic potential ϕ can be shown to relax to a constant level [63]. However, there is a difference in stellarators. Here, the particles can drift away from the flux surfaces leading to a slow oscillation of this component.

Its frequency is far below that of the geodesic acoustic modes which are supposed to be not prominent in W7-X as they either strongly couple to the sound waves [64] or are heavily damped.

The MHD continuum calculated employing the code CONTI is shown in Fig. 14(a). More specifically, the branches for $0 \leq m \leq 4$ and $n = 0$ for Case A and Case B are shown in brown and in gray/colored respectively. From this calculation, we observe all branches to appear as sound modes (c.f. Fig. 10(b)). Focusing on the branches at lowest frequencies, modes with poloidal mode numbers $m = 0, \pm 1$ and ± 2 may appear. Starting with the 18 kHz branch at the plasma center, we observe the branch with $m = -1$. At higher central frequencies of around 22 kHz and 35 kHz, we find the branches with $m = 0, 1$ and $m = \pm 2$ respectively. If compared w.r.t. each other, we observe the branches from Case A to not strongly deviate from their corresponding branch in Case B. This indicates that the rotational transform does not play a major role in the results of this analysis. However, the frequencies are far beyond the mode frequency we detected.

Fig. 14(b) shows the frequency spectrum from an electrostatic gyro-kinetic calculation for the $m = 1$ component of Case B employing the DMUSIC algorithm [53]. The branches observed here only coincide relatively well with the sound wave continuum as seen in Fig. 14(a). Unlike in tokamaks, these are not clear geodesic acoustic mode (i.e. $(m, n) = (0, 0)$) oscillations but rather $m = \pm 1$ side bands. Aspects of this phenomenon have been discussed earlier for W7-X [64, 65]. On the other hand, the GAM-like higher frequency oscillations have always been found in earlier simulations, [29, 66]. The difference to that earlier work is that the damping of the GAM, albeit still considerable, appears to have decreased for the present parameters as shown in Fig. 16. In particular, it might be caused by the lower ϵ value. By Fourier filtering the input to the DMUSIC algorithm, these modes can be attributed to be primarily features of the $m = 1$ and $m = 2$ side bands. These results agree with the GAM branches illustrated in Fig. 14(a) and, additionally, a low-frequency oscillation can be seen at approximately 0.9 kHz.

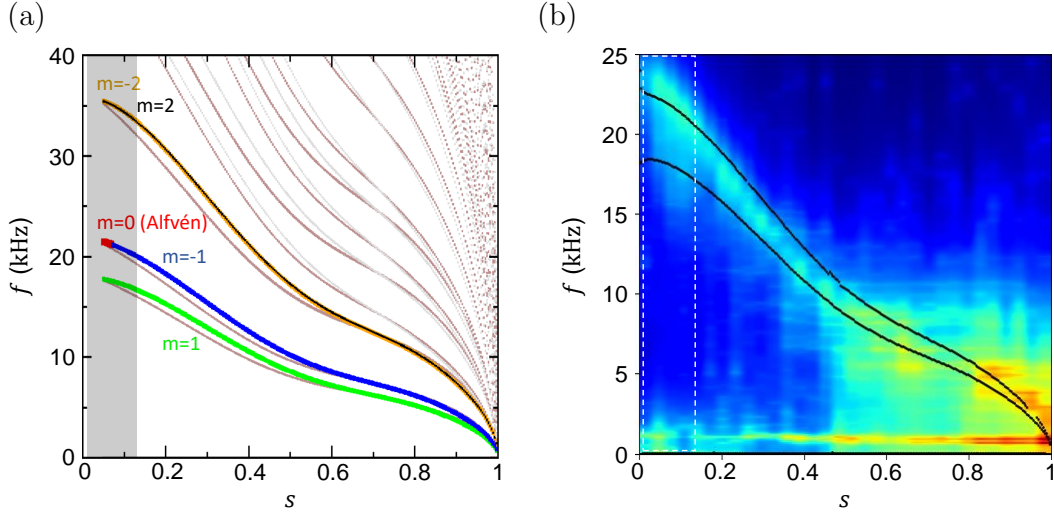


Figure 14. (a) Part ($m = -4 \dots 4, n = 0$) of the continuous spectrum of geodesic acoustic modes (GAM) for the $n = 0$ mode family, plotted over the normalized toroidal flux $s = (r/a)^2$, in W7-X for Case A (vacuum ϵ) and Case B (ϵ corresponding $I_p = 1.4$ kA). In the calculation with CONTI, all branches appear as sound modes, i.e. the dominating component was found to be a $m \neq 0$ pressure perturbation. The branches for Case A and Case B are shown in brown and in gray/colored respectively. There is no radial electric field present in this calculation. (b) DMUSIC Frequency spectrum over s from an electrostatic gyro-kinetic calculation with EUTERPE for Case B with no radial electric field present. The $m = 1$ component is singled out. The black lines represent the (green and blue) GAM like branches ($m = 1$ and $m = -1$) shown in (a). The excitation visible at 0.9 kHz is the zonal flow oscillation. Region delimited by the dashed white line indicates location where the fluctuation activity was experimentally observed.

Focusing on the low-frequency oscillation obtained in Fig. 14(b), Fig. 15 shows the results of the $(m, n) = (0, 0)$ zonal component for Case B without a radial electric field. A marginally stable zonal flow oscillation of approximately 1 kHz can be observed in both investigated cases. The frequency of the zonal component $\phi_{m=0, n=0}$ does not show much variation over the radius. This finding suggests a global mode to be excited. Weak side bands at higher frequencies (≈ 12 kHz) are observed as shown for the normalized toroidal flux at $s = (r/a)^2 = 0.2$ depicted in Fig. 15(b).

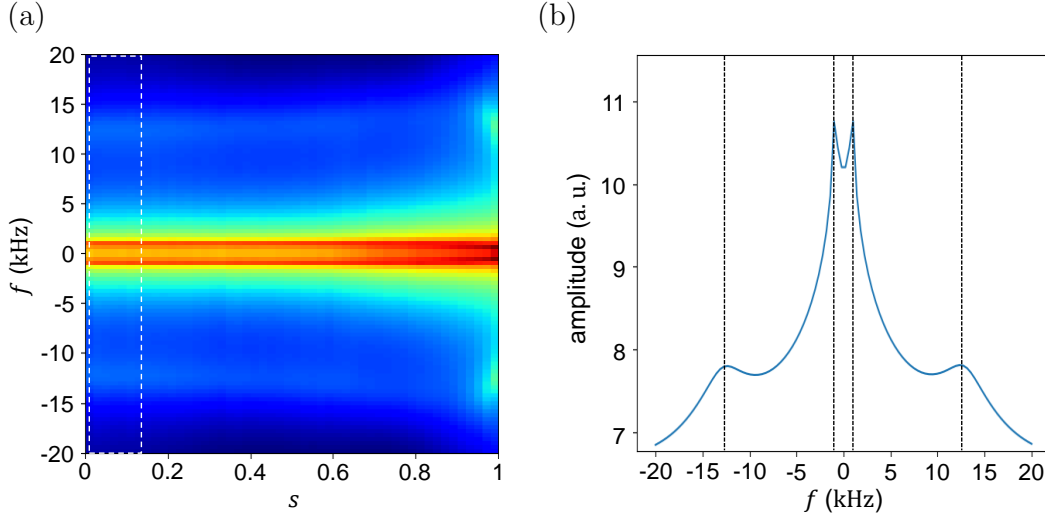


Figure 15. (a) Oscillation of $\phi_{m=0,n=0}$ over the normalized toroidal flux s obtained with DMUSIC from EUTERPE data for Case B. The frequency found is 0.9 kHz and the region delimited by the dashed white line indicates location where the fluctuation activity was experimentally observed. (b) Local frequencies obtained with DMUSIC at $s = 0.2$.

The time evolution of the perturbed potential ϕ of the zonal component $(m, n) = (0, 0)$ due to various E_r profiles is displayed in Fig. 16. This analysis is performed to gain insight on the decay of the low-frequency oscillations. More specifically, to assess the stability of the zonal component for negative and positive flat E_r profiles, as well as the profile calculated through NTSS at an instance after the T_e transition occurred ($t = 1.7$ s, cf. Fig. 2(h)) are shown in Fig. 16(a), (b) and (c) respectively. These fields have been varied between -6 kV/m and 6 kV/m. From Fig. 16(a)-(c) we note that the frequency of the oscillation rises with field as does the damping and the finally achieved residual level of the zonal flow. That is, the damping is lowest for $|E_r| \sim 0$ and increases with $|E_r|$, independent of the sign of the radial electric field. Also, the strongly damped GAM oscillations with much higher frequency are clearly visible at $t \cdot \Omega_* < 1000$. Comparing the results obtained for positive and negative E_r profiles, as seen in Fig. 16(a) and (b) respectively, we observe that the damping of ϕ seems to be slightly stronger for the former than for the latter. Lastly, as illustrated in Fig. 16(c), we note that the perturbed potential for an instance after the T_e transition (red) resembles the calculations obtained for ϕ with a flat $E_r = -6$ kV/m profile (blue); That is, indicating a heavily damped oscillation of the perturbed potential.

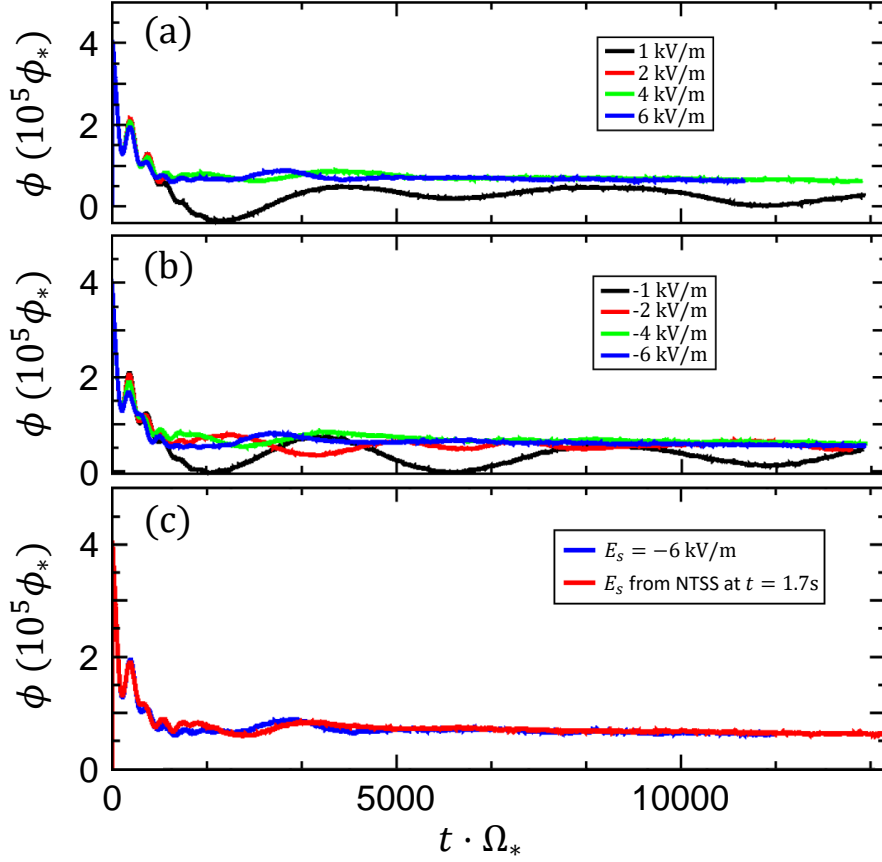


Figure 16. Time traces of the zonal component $(m, n) = (0, 0)$ of the perturbed potential ϕ from electrostatic simulations with EUTERPE. Results employing positive (a) and negative (b) flat radial electric field profiles and (c) the E_r profile calculated with NTSS for an instance after the T_e transition occurred ($t = 1.7$ s, cf. Fig. 2(h)). Time is represented in terms of the ion cyclotron frequency $\Omega = 2.298 \times 10^8 \text{ s}^{-1}$.

Fig. 17 shows the frequency of the low-frequency oscillation and its side bands for a range of experimentally plausible negative and positive flat E_r profiles. More specifically, the frequencies of the $m = 0, 1, 2, 3$ components are depicted with their respective $\vec{E} \times \vec{B}$ drift frequencies. This is, since the appearance of a radial electric field, which arises as a consequence of the non-ambipolarity of the neoclassical transport, will alter the frequency and damping of the zonal flow oscillations as expected from earlier work [66]. We observe from Fig. 17, that the frequency of the different side bands agree to a good extent with the $\vec{E} \times \vec{B}$ frequencies. Also, it is important to note that the frequencies found for these side bands lie in the ballpark of the frequencies observed in the experiments. Particularly, the side bands with $m = 1$ and $m = 2$, given that the local value of the electric field as calculated by NTSS is approximately -4 kV/m at the location with oscillations. For this values of E_r , the $m = 1$ and $m = 2$ side bands reached frequencies of roughly 2.5 kHz and 5 kHz respectively. The findings presented sufficiently demonstrate that an applied electric field damps the zonal flow oscillations by the excitation of Doppler-shifted side bands. It should be noted here, that the effect

looks similar for positive fields and constant profiles.

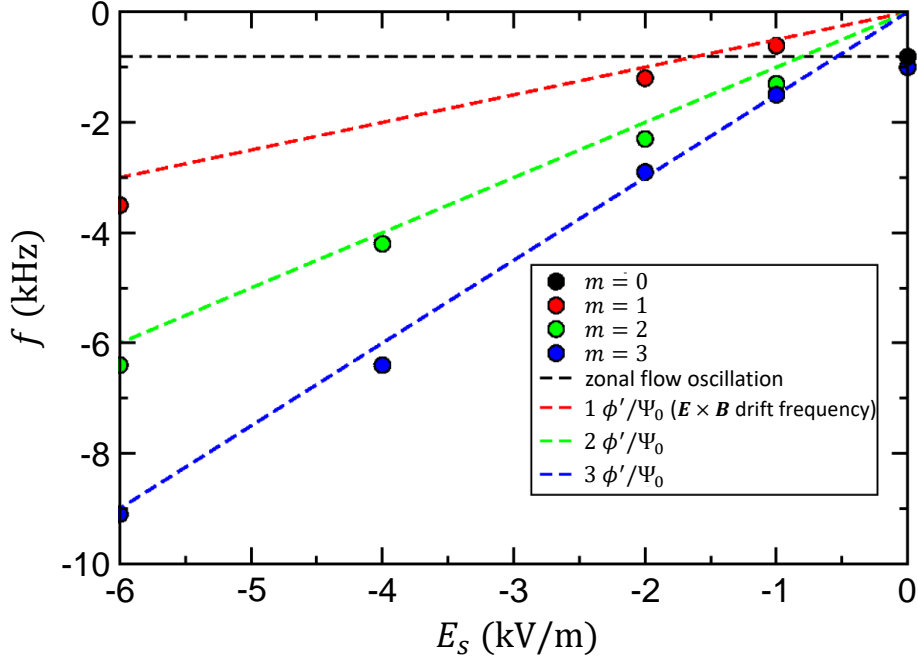


Figure 17. Oscillation frequencies related to a zonal flow excitation for Case B with different radial electric values $E_r = E_s(r/a)$. The excitation decays through different poloidal mode numbers which are Doppler shifted due to $\vec{E} \times \vec{B}$ rotation. Gray shaded region indicates location where the fluctuation activity was experimentally observed.

The effect of taking into account a flat $E_r = 4$ kA profile in the analysis of the low-frequency oscillation using DMUSIC is presented in Fig. 18. To get an impression of the effect of a radial electric field, we applied first radial fields which are proportional to the normalized effective minor radius r/a such that they would lead to a rigid $\vec{E} \times \vec{B}$ rotation such that $E_s = \text{constant}$. The calculation illustrated in Fig. 18(a) shows the effect of a flat E_s profile of constant value 4 kV/m. We note that, by construction, the frequency signal for the $m = 0$ component is strictly symmetric w.r.t. the sign of the frequency and, due to the applied radial electric field, the frequency is upshifted and splitted to approximately 5 kHz and 8 kHz. Fig. 18(b) reveals that the splitting is due to a geometric coupling to an $m = 2$ component of the perturbed potential. Due to its poloidal dependence, the $m = 2$ component is Doppler-shifted by the $\vec{E}_r \times \vec{B}$ rotation to positive frequencies. If the field is negative, then the shift is in the other direction. The up-shifted GAM-like branch of the continuum (≈ -10 kHz at $s \approx 0.5$) and the coupling to the $m = 1$ component at positive frequencies (≈ 5 kHz at $s \approx 0$) is also visible. Remarkably, for the zonal component, the signal appears symmetric and features $m = 2$ and $m = 3$ more prominently than an $m = 1$. When repeating the analysis for other fields, the picture is similar: the $m \neq 0$ components get excited and Doppler-shifted proportional to m (cf. Fig. 17(b)) and so the initial perturbation gets damped.

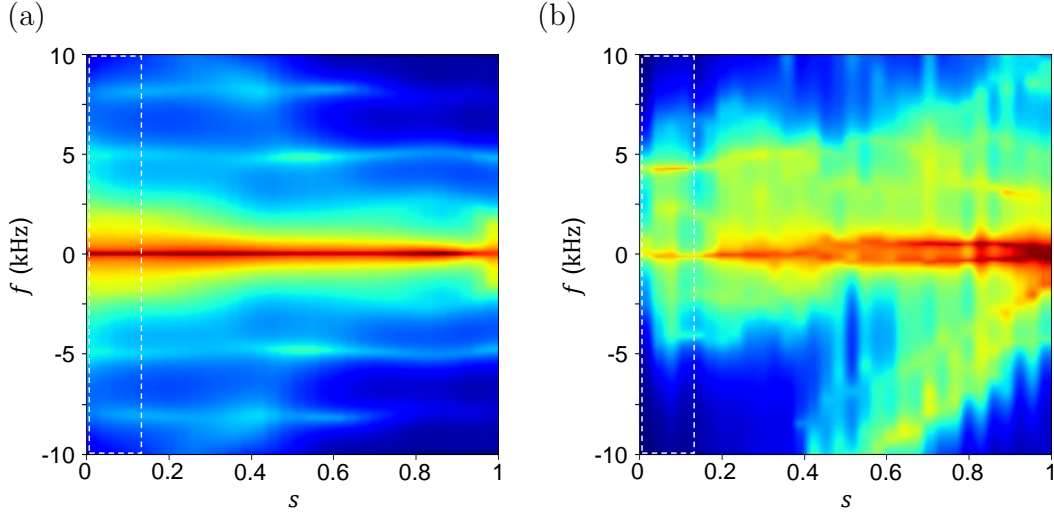


Figure 18. Frequency over the normalized toroidal flux $s = (r/a)^2$ obtained with DMUSIC from EUTERPE data for the (a) $m = 0$ and (b) $m = 2$ components of the zonal flow oscillation with a radial electric field $E_s = 4\text{kV/m}$. Region delimited by the dashed white line indicates location where the fluctuation activity was experimentally observed.

Finally, Fig. 19 shows the analysis of the zonal flow components with the inclusion of the radial electric field calculated by NTSS at a time $t = 1.7\text{s}$ (after T_e transition, cf. Fig. 2(h)). More specifically, the simulations for the zonal components $m = 0$ and $m = 2$ are depicted in Fig. 19(a) and Fig. 19(b) respectively. For both cases, we observe a distortion of the spectra, which corresponds to the Doppler shift caused by the electric field (black lines). In Fig. Fig. 19(a) the distortion is symmetric w.r.t. the sign of the frequency given the strict symmetry of the $m = 0$ component, whereas in Fig. Fig. 19(b) the frequency of the $m = 2$ follows the sign of the E_r profile. In Fig. 19(a) straight lines appear at various frequencies. It would be tempting to attribute them to emerging global zonal flow oscillations, in analogy to the global geodesic acoustic modes [67, 68]. However, in Fig. 19(b) higher and lower in frequency GAM-like branches of the continuum can be observed at $s > 0.5$ and, most interesting, the Doppler shifted zonal flow at the location where the mode activity was observed (region delimited by the white dashed line) can be seen as predicted in the simulation showed in Fig. 17.

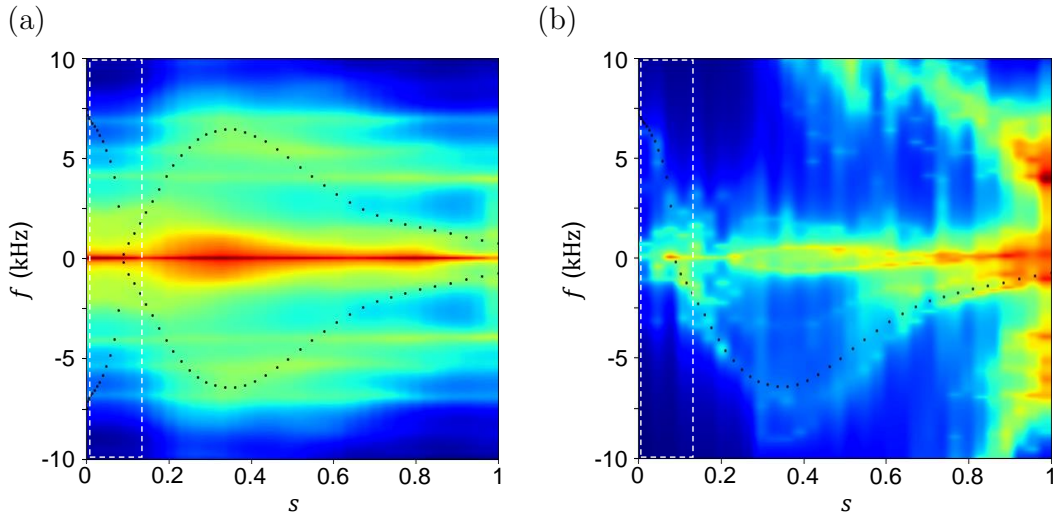


Figure 19. Frequency over the normalized toroidal flux $s = (r/a)^2$ obtained with DMUSIC from EUTERPE data for the (a) $m = 0$ and (b) $m = 2$ components of the zonal flow oscillation with a radial electric field calculated by NTSS at $t = 1.7$ second (after T_e transition). Doppler shift caused by the radial electric field ($m \frac{\phi'(s)}{\psi_0}$) is shown in black dotted lines. Region delimited by the dashed white line indicates location where the fluctuation activity was experimentally observed.

It needs to be noted at this point that the zonal flow oscillations are observable in calculations for many configurations of W7-X. For the usual plasma parameters the frequency is around 1 kHz. Indeed we found a strong dependence on the ambient radial electric field as it was expected from earlier work [66]. We conclude that a radial electric field at typical values of ion-root conditions affects zonal flow oscillations, shifting the frequency to values observed in experiments.

4. Conclusions

Spontaneous transitions to high core-electron temperatures were observed in W7-X low- ι plasmas close to electron-root condition. In the low- ι magnetic configuration, the rotational transform crossed the low-order rational magnetic surface 5/7 at different locations of T_e and $\partial T/\partial r$; whereas in the standard configuration, ι does not cross neither 5/6 nor 5/7, both candidates in which a magnetic island chain is produced given the $N = 5$ toroidal periodicity in W7-X. This finding sheds light on the role of the ι -profile evolution on the transitions and may explain why these transitions were exclusively observed in low- ι plasma discharges. Thus, the experimental observations and the simulations of ι provide evidence that these surfaces may trigger the transition to an electron-root transport regime as seen on H-J and TJ-II.

The calculations in the last sections illustrate that neither an instability of magneto-hydrodynamic nor gyro-kinetic nature is a likely cause for the observed oscillations. We have tried to match the experimental observations to our best and could not find an instability with ideal MHD and gyro-kinetic codes.

Stable Alfvén and sound waves do not match the right frequency range; except those which are associated with a presumed magnetic island at the radial position where $\iota(r) = 5/7$. However, the position of the presumed islands judged from the iota profile does not entirely match the experimental observations and it is beyond the scope of this paper to decide if the existence of such an island is feasible. It may also be the case that the presumed islands play a major role in the transition to the electron-root confinement as it was reported from different fusion experiments in the literature [7, 10]. However, negative findings do not entirely rule out an explanation in that direction as not every detail of the experiment is known accurately enough. Also, there might be other modes or other mode numbers involved that looked at in the calculations. Nevertheless, these calculations make a plasma instability unlikely, except for the 5/7 island which would depend on the subtleties of the profile of the rotational transform. Furthermore, it cannot yet be shown that there is in fact a mode in the island induced gap in the Alfvén spectrum as this is still topic of research [69]. However, the direct comparison of results obtained for Case A (vacuum ι) and Case B (ι corresponding to 1.4 kA) indicates that, the rotational transform has only a small effect on the oscillation observed.

Instead, we offer an alternative interpretation which sort of matches the experimental low frequency observations and perhaps even others [70, 71]: stable zonal flow oscillations that have been found for both configurations studied, Case A and Case B, at around 0.9 kHz. In case of an ambient background field, the zonal flow oscillation appears to decay rapidly through the side bands which are marginal. In comparison, GAM like oscillations are strongly damped ($\gamma \sim \omega$), not matching with the observations of the mode activity before the mode termination. A model calculation using $E_r = E_s(r/a)$ (rigid rotation of the plasma column) illustrates that the side bands undergo Doppler shifts due to the ambient radial electric field which can easily reach several kHz as observed experimentally.

Our calculations do not provide an explanation of why these actually stable oscillations should be excited. However, in the experiments analyzed, the oscillations appear close to the plasma core always after switching on additional on-axis ECRH power, i.e. an external perturbation. This setting corresponds to our calculation which also start with an initially imposed perturbation of the electric potential, which induces the zonal flow excitation. The setting corresponds also to the observation of the zonal flow oscillations in TJ-II [72] which were excited by pellet injection.

The relatively long lasting experimental signal would suggest an additional underlying driving mechanism. It could be relaxing profiles, turbulence or the build-up of a radial electric field ensuring ambipolarity that are driving the zonal flow oscillations. Its subsequent decay into side bands, depending on the electric field and the plasma profiles, could thus offer an explanation for the observed low frequency oscillations in W7-X. The disappearance of the fluctuation activity goes along with the transition to the core electron-root confinement regime, hinting that the new transport conditions attained may be linked with the vanishing of the oscillations. If the fluctuation activity is driven by turbulence, the formation of the internal transport barrier in the transition

to the electron-root confinement regime would lead to the suppression of turbulence and thus lead to the vanishing of the activity.

Acknowledgments

This work has been carried out within the framework of the EUROfusion Consortium, funded by the European Union via the Euratom Research and Training Programme (Grant Agreement No 101052200 — EUROfusion). Views and opinions expressed are however those of the author(s) only and do not necessarily reflect those of the European Union or the European Commission. Neither the European Union nor the European Commission can be held responsible for them.

References

- [1] R C Wolf et al. Major results from the first plasma campaign of the Wendelstein 7-X stellarator. *Nucl. Fusion*, 57:102020, 2017.
- [2] T. Klinger et al. Overview of first Wendelstein 7-X high-performance operation. *Nucl. Fusion*, 59:112004, 2019.
- [3] M. Yokoyama et al. Core electron-root confinement (CERC) in helical plasmas. *Nucl. Fusion*, 47:1213, 2007.
- [4] J F Guerrero Arnaiz, A. Dinklage, J. Geiger, et al. Fast characterization of plasma states in W7-x with permutation entropy. *Plasma Phys. Control. Fusion*, 64:084005, 2022.
- [5] A. Dinklage, G. Fuchert, R.C. Wolf, et al. Validation of theory-based models for the control of plasma currents in W7-X divertor plasmas. *Nucl. Fusion*, 61(12):126022, 2021.
- [6] G. Grieger, W. Lotz, P. Merkel, et al. Physics optimization of stellarators. *Phys. Fluids B*, 4:2081, 1992.
- [7] T. Mizuuchi N. Kenmochi, T. Minami et al. Reformation of the electron internal transport barrier with the appearance of a magnetic island. *Sci. Rep.*, 10, 2020.
- [8] T. Estrada, D. López-Bruna, A. Alonso, et al. Electron Internal Transport Barriers and Magnetic Topology in the Stellarator TJ-II. *Fusion Sci. Technol.*, 50(2):127–135, 2006.
- [9] T. Estrada, F. Medina, D. López-Bruna, et al. Transitions to improved core electron heat confinement triggered by low order rational magnetic surfaces in the stellarator TJ-II. *Nucl. Fusion*, 47(4):305, 2007.
- [10] S. Ohshima. Personal communication, 2022-08.
- [11] E. Pasch, M. N. A. Beurskens, S. A. Bozhnikov, et al. The thomson scattering system at Wendelstein 7-X. *Phys. Scr.*, 92:055601, 2017.
- [12] H J Hartfuss, T Geist, and M Hirsch. Heterodyne methods in millimetre wave plasma diagnostics with applications to ECE, interferometry and reflectometry. *Plasma Phys. Control. Fusion*, 39:1693, 1997.
- [13] S Schmuck, H J Hartfuss, M Hirsch, et al. Design of the ECE diagnostic at Wendelstein 7-X. *Fusion Eng. Des.*, 84:1739, 2009.
- [14] U. Höfel, M. Hirsch, S. Kwak, et al. Bayesian modeling of microwave radiometer calibration on the example of the Wendelstein 7-X electron cyclotron emission diagnostic. *Rev. Sci. Instrum.*, 90:043502, 2019.
- [15] C. Brandt, T. Broszat, H. Thomsen, et al. Installation of the soft x-ray multi-camera tomography system (XMCTS) in the Wendelstein 7-X stellarator. *Fusion Eng. Des.*, 123:887, 2017.
- [16] C. Brandt, J. Schilling, H. Thomsen, et al. Soft x-ray tomography measurements in the Wendelstein 7-X stellarator. *Plasma Phys. Control. Fusion*, 62(3):035010, 2020.

- [17] K. Rahbarnia, H. Thomsen, U. Neuner, et al. Diamagnetic energy measurement during the first operational phase at the Wendelstein 7-X stellarator. *Nucl. Fusion*, 58:096010, 2018.
- [18] U. Neuner, K. Rahbarnia, C.D. Beidler, et al. Measurements of the parameter dependencies of the bootstrap current in the W7-x stellarator. *Nucl. Fusion*, 61:036024, 2021.
- [19] M.A. Chilenski, M. Greenwald, Y. Marzouk, et al. Improved profile fitting and quantification of uncertainty in experimental measurements of impurity transport coefficients using gaussian process regression. *Nucl. Fusion*, 55(2):023012, 2015.
- [20] Yu. Turkin, H. Maassberg, C. D. Beidler, et al. Current control by ECCD for W7-x. *Fusion Sci. Technol.*, 2006.
- [21] K.C. Shaing. *Phys. Fluids*, 27(7):1567, 1984.
- [22] T. Sunn Pedersen, M. Otte, S. Lazerson, et al. Confirmation of the topology of the Wendelstein 7-X magnetic field to better than 1:100,000. *Nat. Commun.*, 2016.
- [23] C. Nührenberg. Global ideal magnetohydrodynamic stability analysis for the configurational space of Wendelstein 7-X. *Plasma Phys. Control. Fusion.*, 1996.
- [24] C. Nührenberg. Compressional ideal magnetohydrodynamics: Unstable global modes, stable spectra, and alfvén eigenmodes in Wendelstein 7-X-type equilibria. *Plasma Phys. Control. Fusion.*, 1999.
- [25] C. Nührenberg. Free-boundary ideal MHD stability of W7-X divertor equilibria. *Nucl. Fusion*, 2016.
- [26] A. Mishchenko, M. Borchardt, M. Cole, et al. Global linear gyrokinetic particle-in-cell simulations including electromagnetic effects in shaped plasmas. *Nucl. Fusion*, 55:053006, 2015.
- [27] R. Kleiber, R. Hatzky, and A. Könies. An explicit large time step particle-in-cell scheme for nonlinear gyrokinetic simulations in the electromagnetic regime. *Phys. Plasmas*, 23:032501, 2016.
- [28] A. Zocco, A. Mishchenko, C. Nührenberg, et al. W7-x and the sawtooth instability: towards realistic simulations of current-driven magnetic reconnection. *Nucl. Fusion*, 61:086001, 2021.
- [29] A. Mishchenko, P. Helander, and A. Könies. Collisionless dynamics of zonal flows in stellarator geometry. *Plasma Phys. Control. Fusion.*, 2008.
- [30] A. Mishchenko and A. J. Brizard. Higher-order energy-conserving gyrokinetic theory. *Plasma Phys. Control. Fusion.*, 2011.
- [31] H. Alfvén. Existence of electromagnetic-hydrodynamic waves. *Nature*, 150:405, 1942.
- [32] K. Iwai, K. Shinya, K. Takashi, et al. Pressure change accompanying Alfvén waves in a liquid metal. *Magnetohydrodynamics*, 39:245, 2003.
- [33] F. F. Chen. *Waves in plasmas*, chapter 4, pages 95–138. Plenum Press, New York, 1974.
- [34] T. B. Fehér. *Simulation of the interaction between Alfvén waves and fast particles*. PhD Thesis, Greifswald, Greifswald, 2013.
- [35] L. Tonks and I. Langmuir. Oscillations in ionized gases. *Phys. Rev.*, 33:195, 1929.
- [36] F. F. Lu and S. Q. Liu. Dispersion and damping of ion acoustic wave in deuterium–tritium fusion plasmas with slowing-down distributed α particles. *AIP Adv.*, 11:055112, 2021.
- [37] E. Sánchez, I. Calvo, and J. L. Velasco. Oscillatory relaxation of zonal flows in a multi-species stellarator plasma. *Plasma Phys. Control. Fusion*, 60:094003, 2018.
- [38] P. H. Diamond, S-I Itoh, K. Itoh, et al. Zonal flows in plasma — a review. *Plasma Phys. Control. Fusion*, 47:R35, 2005.
- [39] N. Winsor, J. L. Johnson, and J. M. Dawson. Geodesic acoustic waves in hydromagnetic systems. *Phys. Fluids*, 11:2448, 1968.
- [40] G.D. Conway, A.I. Smolyakov, and T. Ido. Geodesic acoustic modes in magnetic confinement devices. *Nucl. Fusion*, 62:013001, 2022.
- [41] A. Mishchenko, P. Helander, and A. Könies. Collisionless dynamics of zonal flows in stellarator geometry. *Phys. Plasmas*, 15:072309, 2008.
- [42] R. Kleiber, R. Hatzky, A. Könies, et al. An improved control-variate scheme for particle-in-cell simulations with collisions. *Comput. Phys. Commun.*, 2011.

- [43] P. Monreal, E. Sánchez, I. Calvo, et al. Semianalytical calculation of the zonal-flow oscillation frequency in stellarators. *Plasma Phys. Control. Fusion*, 59:065005, 2017.
- [44] V. Igochine. Magneto-hydrodynamics and operational limit. In V. Igochine, editor, *Active control of magneto-hydrodynamic instabilities in hot plasmas*, pages 53 – 104. Springer, Berlin Heidelberg, 2015.
- [45] R. Fitzpatrick. Helical temperature perturbations associated with tearing modes in tokamak plasmas. *Phys. Plasmas*, 2:825, 1995.
- [46] N. B. Marushchenko, Y. Turkin, and H. Maassberg. Ray-tracing code TRAVIS for ECR heating, EC current drive and ECE diagnostic. *Comput. Phys. Commun.*, 185:165, 2014.
- [47] S. P. Hirshman, W. I. van RIJ, and P. Merkel. Three-dimensional free boundary calculations using a spectral green’s function method. *Comput. Phys. Commun.*, 43:143, 1986.
- [48] I. B. Bernstein, E. A. Frieman, M. D. Kruskal, et al. An energy principle for hydromagnetic stability problems. *Proc. R. Soc. A: Math. Phys. Eng. Sci.*, 244:17, 1958.
- [49] A. Zocco, G. G. Plunk, P. Xanthopoulos, et al. Geometric stabilization of the electrostatic ion-temperature-gradient driven instability. I. Nearly axisymmetric systems. *Phys. Plasmas*, 23:082516, 2016.
- [50] A. Könies and D. Eremin. Coupling of Alfvén and sound waves in stellarator plasmas. *Phys. Plasmas*, 17:012107, 2010.
- [51] A. Könies, C. Slaby, R. Kleiber, et al. The MHD continuum with a radial electric field. *Phys. Plasmas*, 27:122511, 2020.
- [52] A. Könies, J. Cao, R. Kleiber, et al. A numerical approach to the calculation of the Alfvén continuum in the presence of magnetic islands. *Phys. Plasmas*, 29(9):092102, 2022.
- [53] R. Kleiber, M. Borchardt, A. Könies, et al. Global gyrokinetic pic simulations for stellarators and heliotrons with emphasis on experimentally relevant scenarios. In *18th European Fusion Theory Conference (EFTC), Ghent, Belgium*, 2019.
- [54] C. Nührenberg and A. H. Boozer. Magnetic islands and perturbed plasma equilibria. *Plasma Phys. Control. Fusion.*, 2003.
- [55] 2021.
- [56] R. Jiménez-Gómez, A. Könies, E. Ascasíbar, et al. Alfvén eigenmodes measured in the TJ-II stellarator. *Nucl. Fusion*, 2011.
- [57] A. Biancalani, L. Chen, F. Pegoraro, et al. Continuous Spectrum of Shear Alfvén Waves within Magnetic Islands. *Phys. Rev. Lett.*, 2010.
- [58] C. R. Cook and C. C. Hegna. Analytical theory of the shear Alfvén continuum in the presence of a magnetic island. *Phys. Plasmas*, 2015.
- [59] C. R. Cook, C. C. Hegna, J. K. Anderson, et al. Identification of island-induced Alfvén eigenmodes in a reversed field pinch. *Plasma Phys. Control. Fusion*, 2016.
- [60] T. Hayashi, A. Takei, and T. Sato. Magnetic surface breaking in three-dimensional $l=2$ heliotron/torsatron equilibria. *Phys. Fluids B*, (4):1539, 1992.
- [61] R. Hatzky, R. Kleiber, A. Könies, et al. Reduction of the statistical error in electromagnetic gyrokinetic particle-in-cell simulations. *J. Plasma Phys.*, 2019.
- [62] R. Kleiber. *in preparation*, 2020.
- [63] M. N. Rosenbluth and F. L. Hinton. Poloidal flow driven by ion-temperature-gradient turbulence in tokamaks. *Phys. Rev. Lett.*, 80:724–727, 1998.
- [64] Ya. I. Kolesnichenko, V. V. Lutsenko, A. Weller, et al. Conventional and nonconventional global alfvén eigenmodes in stellarators. *Phys. Plasmas*, 2007.
- [65] C. Nührenberg and K. Hallatschek. 3-d linear mhd for acoustic modes and zonal flows. In *33rd EPS Conference on Contr. Fusion and Plasma Physics, ECA*, volume 30 I, page P2.116, 2006.
- [66] A. Mishchenko and R. Kleiber. Zonal flows in stellarators in an ambient radial electric field. *Plasma Phys. Control. Fusion.*, 2012.
- [67] V.P. Lakhin and E.A. Sorokina. Geodesic acoustic eigenmode for tokamak equilibrium with maximum of local GAM frequency. *Physics Letters A*, 2014.

- [68] G.D. Conway, A.I. Smolyakov, and T. Ido. Geodesic acoustic modes in magnetic confinement devices. *Nucl. Fusion*, 2021.
- [69] A. Könies, J. Cao, R. Kleiber, et al. A numerical approach to the calculation of the alfvén continuum in the presence of magnetic islands. *Plasma Phys. Control. Fusion.*, 2022.
- [70] J.-P. Böhner, J. A. Alcusón, S. K. Hansen, et al. Phase contrast imaging measurements and numerical simulations of turbulent density fluctuations in gas-fuelled ECRH discharges in Wendelstein 7-X. *J. Plasma Phys.*, 2021.
- [71] S. B. Ballinger, J. L. Terry, S. G. Baek, et al. Dynamics and dependencies of the configuration-dependent 1–2 kHz fluctuation in W7-x. *Nuclear Materials and Energy*, 2021.
- [72] J. A. Alonso, E. Sánchez, I. Calvo, et al. Observation of oscillatory radial electric field relaxation in a helical plasma. *Phys. Rev. Lett.*, 118:185002, 2017.

B. Statutory Declaration

Eigenständigkeitserklärung

Hiermit erkläre ich, dass diese Arbeit bisher von mir weder an der Mathematisch-Naturwissenschaftlichen Fakultät der Universität Greifswald noch einer anderen wissenschaftlichen Einrichtung zum Zwecke der Promotion eingereicht wurde. Ferner erkläre ich, dass ich diese Arbeit selbstständig verfasst und keine anderen als die darin angegebenen Hilfsmittel und Hilfen benutzt und keine Textabschnitte eines Dritten ohne Kennzeichnung übernommen habe.

Greifswald, 31st July 2023

Juan Fernando Guerrero Arnaiz

C. Acknowledgments

First and foremost, I would like to express my deepest gratitude and appreciation to my supervisor Dr. Andreas Dinklage for his guidance, invaluable insights, and continuous encouragement throughout this research endeavor. His expertise, patience, and commitment to excellence played a pivotal role in guaranteeing the quality of this work. I would like to extend my gratitude to Dr. Bernd Pompe for the insightful and stimulating discussions, and to Dr. Michael Endler for his valuable feedback that majorly shaped the direction of this research.

I am deeply thankful to Dr. Mathias Hirsch and Dr. Henning Thomsen for their helpful advice, remarks and extensive knowledge on the W7-X diagnostics, and to Dr. Axel Könies, Dr. Alessandro Zocco, Dr. Carolin Nührenberg for guiding me through the various numerical methods employed throughout this thesis and their theoretical background. Their collective support and belief in the importance of this scientific inquiry have made this accomplishment possible.

I would also like to thank my friends and colleagues for the moral support and unnecessary, but rather amusing discussions. Thank you Marco for eating lunch at 11:30am almost everyday with me. Thank you Neha for constantly reminding me that there is more than just working. And thank you Hjördis for standing up every 30 minutes and "lüften". Jokes aside, thank you all for the moral support and for trying your best to answer any question I came up with regarding this work.

Finally, I am grateful for the love and encouragement from my family. I tried my best and I did it both, for myself, and to make you all proud. I hope this journey was worth your support and sacrifices. You have been a constant source of inspiration and motivation, enabling me to pursue my educational goals with determination and perseverance. Last but not least, I want to thank my significant other for believing in me, even during those times when I doubted myself.